Magnetic Field Amplification in Laser-Produced Plasmas

Jena Meinecke

Merton College

Atomic and Laser Physics Department

University of Oxford

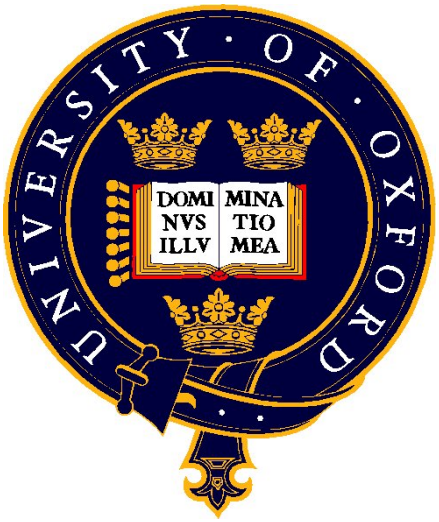

A thesis submitted in fulfilment of the requirements for the degree of

Doctor of Philosophy at the University of Oxford

Michaelmas term, 2015

Abstract

The universe abounds with shock waves, from those arising during structure formation, to those driving supernova explosions that create the elements of which life is made and can even trigger star formation. In the early universe, matter was nearly homogeneously distributed; today, as a result of gravitational instabilities, it forms a web-like structure of clusters, filaments, and voids [1]. Radio-Synchrotron emission and Faraday Rotation measurements have revealed that clusters, filaments, and voids are all magnetised from a few nG to tens of μG [2][3]. When integrated over the whole universe, this magnetic energy represents a sizeable component of the cosmic energy budget, making magnetic fields essential players in the dynamics of luminous matter in the universe.

At present, the origin and distribution of magnetic fields are far from understood. The standard model for the origin of galactic and intergalactic magnetic fields is through the generation of small seed fields by some mechanism (e.g. Biermann Battery) and the amplification of these seed fields via dynamo or turbulent processes to the level consistent with current observations [4][5][6][7]. Due to the advent of high-powered lasers, scaled astrophysical phenomena can be created in the laboratory [8][9] – a supernova several parsecs in diameter can be scaled down to the size of a baseball. These laboratory plasmas are similar to plasmas in the universe in terms of localisation, heat conduction, viscosity, and radiation.

Here we report on experimental measurements of magnetic field amplification by turbulent motions in both laser-produced shock waves scaled to supernova remnants [7] and laser-produced jets analogous to cluster merger events [10]. These measurements of turbulent magnetic field amplification in a laser-produced plasma are a precursor to turbulent dynamo [11] in which amplification is no longer limited by diffusion, and a necessary component in explaining the magnetisation of luminous matter in the universe [6].

To my family

Acknowledgements

From the bottom of my heart and with the utmost sincerity, I am incredibly grateful for my graduate advisor, Professor Gianluca Gregori. He has been the best mentor a student could ever ask for. Gianluca has promoted me, given me confidence and reassurance, and shown me how to look at problems like a scientist. I've watched my friends struggle with their advisors, loosing passion for science– some even leaving research all-together. Gianluca has not only changed my life, but arguably those of his other students who still have a fierce passion and curiosity for science after facing the challenges of a graduate programme. Most importantly, Gianluca serves as a role model. He has an amazing intuition for the future of science, analyses problems quickly, generates creative solutions, and yet manages to stay calm and humble throughout the entire process. Thank you, Gianluca for setting high standards in yourself– I am eternally grateful.

I never wanted to be a scientist. I always intended to be an artist like my grandmother. Art, in it's many forms, is the one thing, with confidence, that I can say I'm 'good' at. However, in 2007, after accidentally taking a physics course in college (and enjoying it!), Dustin Froula heard about my interest in physics and took me on as a summer intern at the Lawrence Livermore National Laboratory (LLNL). He reminds me (far too often) that in my first year doing 'real' experiments, I estimated a 1 kA output from the wall sockets. I had a lot to learn and great mentors including Steven Ross and Brad Pollock. I didn't have a clue about career options in research, let alone the amount of fun involved with a physics experiment. After Dustin moved to Rochester, Siegfried Glenzer took me on as his student– that's when things really began to pick up. Each summer, Siegfried would literally give me a target area (either TA 2 or Janus) in the Jupiter Laser Facility, and say 'go make this experiment work.' I grew a lot during the four years at LLNL– the opportunities afforded to me at LLNL made me the experimentalist I am today. I owe all of my successes to both Dustin and Siegfried for believing in me.

At the University of Oxford, I had the opportunity to work with many wonderful scientists who challenged me everyday. Without listing them all, I would prefer to draw attention to one person in particular– Hugo Doyle. Hugo was our postdoc for a few years and helped me on all the experiments in this thesis. He had an incredible ability to make people smile, even when things were rough. I can be stubborn and difficult to work with sometimes (...many times). Unbeknown to Hugo, he served as a role model for how I should conduct myself in a team. He helped me grow as a person– not just as a scientist. Furthermore, he was a great teacher and better friend. I'm grateful to have known Hugo and wish he was still working with us.

Thank you everyone!

Warmest regards,

Jena Meinecke x

P.S. Thank you Joseph Cross for submitting my thesis to Examination Schools while I've been overseeing NIF preparations in California! You're a dear!! Also, thank you (a million times!) to Charlie Jarrott for helping me get LaTeX to work– you're a Computer Whisperer.

Contents

Abstract **i**

Acknowledgements **iii**

1 Introduction **1**

1.1 Historical Context 1

1.2 Motivation: Why study laboratory astrophysics? 4

1.3 Overview: The origins of magnetic fields 6

1.3.1 Astrophysical methods of measuring magnetic fields 9

1.4 Plasma Dynamics 14

1.4.1 Definition of a plasma 14

1.4.2 Single-particle motions 16

1.4.3 Plasmas as fluids 20

1.5 Organisation of this thesis 20

1.6 Contributors 22

1.6.1 Publications and Honours 25

2 Theoretical Background **29**

2.1 Description of Shock waves 29

2.1.1 Jump Conditions and Shock Relations 30

2.1.2 Blastwaves: Energy Conservation and Sedov-Taylor Regime 32

2.2 Formation of Astrophysical and Laser-produced Jets 34

2.3 Magnetohydrodynamics 36

2.4 Generation of Seed Magnetic Fields 39

2.4.1 Weibel Instability 40

2.4.2 Return Currents . . . 42
2.4.3 Biermann Battery Mechanism . . . 42
2.5 Development of Turbulence . . . 47
2.5.1 Magnetic Field Amplification by the Turbulent Dynamo Mechanism 51
2.5.2 Turbulent Induction of Magnetic Fields for low Pm . . . 52
2.6 Scaling of Laboratory Plasmas to Astrophysical Phenomena . . . 56
2.6.1 Hydrodynamic Similarity Conditions . . . 56
2.6.2 Scaling Assumptions . . . 57
2.7 Laser-Matter Interactions . . . 60
2.7.1 Nonlinear Wave Effects . . . 61
2.7.2 Electron Motion in a Laser Field . . . 62
2.7.3 Ionisation Mechanisms . . . 63
2.7.4 Absorption of Electromagnetic Waves . . . 64
2.7.5 Landau Damping . . . 66
2.7.6 Parametric Instabilities . . . 67

3 Instrumentation and Experimental Methods 69
3.1 High-Energy Lasers . . . 69
3.1.1 Quantum mechanical description of lasers . . . 69
3.1.2 Solid-state laser construction . . . 73
3.1.3 Nd: glass lasers . . . 77
3.1.4 RAL Vulcan Target Area West laser . . . 79
3.1.5 Titan laser . . . 81
3.1.6 NIF laser . . . 81
3.2 Optical Diagnostics . . . 83
3.2.1 Schlieren Imaging . . . 84
3.2.2 Mach-Zehnder Interferometer . . . 89
3.2.3 Spectroscopy . . . 91

3.3 Magnetic Field 'Bdot' Probes 94
3.3.1 Design and Construction 95
3.3.2 Calibration Technique 98
3.3.3 Interpretation of Data 102

4 Magnetic Field Amplification of Laser-produced Shock Waves 107

4.1 Astrophysical Motivation– Supernova Remnant Cassiopeia A 108
4.2 Background and Previous Work 109
4.3 Experimental Arrangements 111
4.4 Plasma Characterisation of Laser-produced Shock Waves 114
4.4.1 Description of Helios and FLASH Simulations 116
4.5 Magnetic Field Characterisation of Shock-induced Turbulence 117
4.5.1 Development of Kolmogorov Turbulence 120
4.5.2 Cross Correlation and Growth Rate 122
4.6 Scaling of Laser-Produced Shock Waves to Cassiopeia A 124
4.7 Reproducibility on Other Laser Facilities 127

5 Nonlinear Amplification of Magnetic Fields in Laser-Produced Jets 130

5.1 Astrophysical Motivation– Turbulence in Cluster Merger Events 130
5.2 Experimental Arrangements 132
5.3 Plasma Characterisation of Laser-Produced Jets 134
5.3.1 Description and Implications of FLASH Simulations 134
5.3.2 The MHD Approximation 138
5.4 Magnetic Field Characterisation of Jets 140
5.4.1 Effect of an Applied-Static Magnetic Field 141
5.4.2 Magnetic Field Amplification in Colliding Jets 143

5.5 Development of Kolmogorov-like Turbulence 144
5.5.1 Thermal Broadening due to Turbulent Motions 147
5.5.2 Balancing Turbulent Heating with Radiative Cooling 148
5.6 Astrophysical Relevance to the Coma Cluster 152
5.7 Comparison with Laser-Produced Jets from Aluminium Foil Targets 155
5.7.1 Magnetic Field Characterisation and Development of Turbulence . . 156

6 Future Work: Measurements of Turbulent Dynamo using the NIF 159
6.1 Experimental Arrangements 159
6.2 Predicted Results and Simulations 164

Conclusions 166

Chapter 1

Introduction

The generation and amplification of magnetic fields in laser-produced plasmas presented in this thesis, fall within the field of 'laboratory astrophysics.' Driven by recent developments of high-energy lasers [12], the study of laboratory astrophysics sheds light on the dynamics of large-scale objects in the universe ranging from supernovas to galaxy clusters. By recreating scaled, laboratory events, we can study how astrophysical objects behave in order to understand the story of the universe. Even though the majority of the work presented in this thesis will represent laboratory observations of tabletop plasmas, we will use this chapter to discuss methods and measurements of astrophysical plasmas.

1.1 Historical Context

The field of laboratory astrophysics is relatively new and only gained momentum about 20 years ago, a few decades after the invention of the laser. Today, as a result of advancements in laser technology, laboratory astrophysics is becoming quite popular, encompassing several hundreds of plasma physicists from around the world to investigate topics ranging from plasma instabilities to the dynamics of planetary cores. The research conducted in this field is literally out of this world and provides a unique opportunity to bridge the gap between experimental physicists and astronomers. Together we can search for answers to questions humanity has been asking for ages: How did the universe evolve? What is the nature of the large-scale, astrophysical objects and events? If we can better understand astrophysical phenomena, how can this influence the future of humanity?

Laboratory astrophysics is typically classified under an umbrella of science called 'high-energy-density physics' defined by pressures above one million atmospheres [13]. Since 1 Mbar is 100 Jmm^{-3}, the laser systems used for our experiments, which deposit $\sim$300 J over $\sim$300 $\mu\mathrm{m}^3$, are well within this regime. Several events led to the creation of laboratory astrophysics. In the 1930s, particle accelerators were developed to compress large numbers of particles within a small space. In the 1940s, nuclear weapons produced high-energy-density conditions which were (fortunately) not ideal for systematic studies. The Z-pinch was developed in the 1950s with hopes of creating controlled thermonuclear fusion. However, it was not until the late 1950s and 1960s, with the invention of the laser, that the field began to take substantial steps forward.

High energy lasers, the ideal tool for creating tabletop, astrophysical objects, owe their existence to inertial confinement fusion. Efforts to create fusion environments began in the United States, Soviet Union, Europe, and Japan. At the forefront of this research was the Lawrence Livermore National Laboratory (LLNL) in California. Scientists at LLNL had been interested in glass lasers and began development in 1975 on the Cyclops laser which was used to tackle the issue of beam self-focusing. The Argus laser in 1976 introduced the concept of using more than one beam to ablate a target. The Shiva laser in 1977 was a high power system with 20 separate amplifiers and notably served as the precursor to the infamous Nova laser– the most powerful laser of its time. John Emmett and the LLNL Laser Science team developed this impressive machine in 1984 which delivered >1 kJ of light in 1 ns using 10 laser beams.

The development of Nova at LLNL marks an important period of history– this is when some of the first laboratory astrophysics experiments were conducted. Serendipitously, on February 23, 1987 at 0735 UT, the blue supergiant Sanduleak located in the Large Magellanic Cloud, a dwarf galaxy located 50 kpc from Earth, exploded as a core-collapse type II supernova. Scientists clamoured at the opportunity to study the early moments of such a powerful event and quickly noticed that previously accepted simulations were orders

of magnitude off from the observable data. This motivated scientists to better understand the dynamics of large scale phenomena in the universe through laboratory analogies.

Many contributed to the early development of laboratory astrophysics, but a few in particular are worth noting: B. A. Remington, R. P. Drake, J. Kane, and D. Ryutov. Remington led an experimental team in 1996 using the Nova laser to study both hydrodynamic instabilities relevant to core-collapse supernovae and plasma flow dynamics relevant to supernovae ejecta. Ultimately he wanted to understand the dynamics of ambient plasma interactions during the early stages of remnant formation. The team measured a strong shock that was maximally compressed in both the experimental and astrophysical plasmas. Furthermore Remington was able to make a comparison between the laboratory plasmas and astrophysical objects necessary to drive the field of laboratory astrophysics forward. Shortly after, Kane used the experimental data from Nova to benchmark aspects of the nonlinear hydrodynamics of the supernova code PROMETHEUS.

The momentum continued with Drake in 1998 when he began experiments to test Rayleigh-Taylor (RT) instabilities by characterising the forward and reverse shocks launched into a foam. The transformation from his experiment to the supernova remnant case was 1 ns to 1 yr, 100 km/s to 10^4 km/s, and 100 μm to 0.03 lt-yr. Drake was able to make this analogy due to theoretical work done by Ryutov in which he showed that the Euler equations (describing the evolution of density, momentum, and entropy) are invariant under transformations that keep ut/l constant, where u, t, and l are velocity, time, and spatial dimension, respectively. Thus the field of laboratory astrophysics was born. In 2011, Gregori proposed studying magnetic field generation in astrophysically-relevant shock waves by filling a chamber with an ambient gas. As a result, this thesis will demonstrate the author's contribution to the field of laboratory astrophysics through experimental studies into the origins of magnetic fields in the universe.

Now we look to the future of laboratory astrophysics and what possibilities lie ahead.

The National Ignition Facility (NIF) has recently begun allowing universities to use their laser for 'discovery science' which goes beyond the initiatives of the inertial confinement fusion project. The NIF laser is hands-down the most energetic laser the world has ever seen, delivering MJs of energy and opening up a new window of opportunities for scientists interested in high-energy-density regimes. Furthermore, the Laser Megajoule (LMJ) facility in France is starting to accept proposals for their new laser which should be ready in the coming years. In short, the field of laboratory astrophysics is growing rapidly and will continue to do so as long as advancements in laser facilities continue to progress.

1.2 Motivation: Why study laboratory astrophysics?

The field of astronomy according to Plato, "compels the soul to look upwards and leads us from this world to another." However, astronomy is fundamentally an observational science with its fair share of limitations. Fifty years ago, if scientists wanted to understand the dynamics of phenomena in the universe (e.g. supernova explosions), they would have to point their telescopes in the right direction and wait around for something to happen. Events in the universe occur over large timescales. For instance, the most recent supernova event that occurred in the Milky Way galaxy was discovered by Johannes Kepler in 1604– an explosion so luminous that it lit up the night sky and was even visible during the day. The next supernova event predicted in our galaxy is Eta Carinae, a blue supergiant roughly 120 times the mass of the Sun, which is predicted to explode in a few hundred thousand years– imagine waiting around for that event.

Fortunately, the field of laboratory astrophysics provides a solution to this problem. Events that occur over hundreds of years can be recreated within a few nanoseconds. Objects which extend over hundreds of trillions of miles in space, can be scaled down to a

few centimetres in the laboratory. High-energy lasers are capable of creating plasmas which are similar to those observed in space. Specifically, when laser-produced plasmas fulfil the following criteria, they are considered hydrodynamically similar [9][14]: (1) the system needs to be 'collisional'; (2) energy flow by particle heat conduction needs to be negligible; (3) energy flow by radiation flux needs to be negligible; and (4) viscous dissipation needs to be insignificant. A full description of these scaling requirements can be found in Section 2.6. In practice, experimentalists crudely focus their attention on two parameters: a large Reynolds number (Re) and a large magnetic Reynolds number (Rm). For $\mathrm{Re} \gg 1$ inertial forces dominate the flow which means viscous forces are negligible. For $\mathrm{Rm} > 1$, magnetic fields are capable of being advected with the flow instead of quickly dissipating out [11]. To attain such values, the plasmas need to have a high velocities and temperatures that can be attained from high-energy deposition onto a target.

However, astrophysical plasmas boast $\mathrm{Re} \sim 10^{13}$ and $\mathrm{Rm} \sim 10^{27}$– parameters which are orders-of-magnitude larger than laser-produced plasmas. So how can one say that laboratory plasmas are similar to astrophysical objects? As long as $\mathrm{Re} > 10^3$ (in these reported experiments $\mathrm{Re} \sim 10^4$), then the Reynolds number is above the critical level to develop vortices, further implying that viscous forces are no longer dominant. Furthermore, for $\mathrm{Rm} \sim 1$, magnetic fields can be advected with the flow but will dissipate over time. However, for $\mathrm{Rm} > 200$, which is attainable on the NIF laser, a new phenomenon called dynamo sets in [11]– the same mechanism that operates at $\mathrm{Rm} \sim 10^{27}$ as observed in supernovas. Further justification and support for this argument can be found in Section 2.5.

More broadly, it's worth asking why we should even care about understanding astrophysical events. The NIF laser was built for the purpose of attaining fusion energy as an alternate source of clean energy. It may then seem a bit silly to take time away from this important project to use the NIF laser to study the dynamics of supernovas. However, even events common in our daily lives (e.g. Kelvin-Helmholtz instabilities in clouds), can

be observed in cosmic events. For instance, RT instabilities, which are prevalent in cosmic events, are also common in inertial confinement fusion reactions. By better understanding how instabilities behave in scaled-astrophysical plasmas, we can better understand how they behave in other environments of interest. Furthermore, laboratory astrophysics provides scientists with a means of answering fundamental questions about our existence and place in the larger universe. For instance, supernova explosions are the violent death of a star; powerful shock waves generated from an explosion, sweep across galaxies, dispersing vital elements of which life is made of– the iron in our blood, calcium in our bones, and oxygen we breathe. *Our* physical bodies are composed of star dust, and it is likely that my left hand came from a different dying star than my right hand. At the end of the day, we are made from the stardust that permeated the universe through a supernova explosion. Studying this type of phenomena can help us better understand how we came into existence. As Michio Kaku states, "Physicists are made of atoms. A physicist is an attempt by an atom to understand itself."

1.3 Overview: The origins of magnetic fields

Magnetic fields are ubiquitous to luminous matter in the universe and accompany the formation and destruction of large-scale objects. It has been suggested that magnetic fields could have affected galaxy formation and the early evolution of the universe [4]. Magnetic forces could be responsible for causing density fluctuations to form in primordial gas that triggered the collapse of matter to form bound objects. In terms of star formation, magnetic fields influence the distribution of stellar masses. For instance, in the absence of a magnetic field, stars would shift towards larger masses as observed in the early galactic evolution.

However, the origins of magnetic fields remain a mystery. To our knowledge, magnetic fields did not exist at the on-set of the Big Bang but instead were created years later during

the formation of large-scale structures such as clusters, filaments, and voids. This leads to one of the most perplexing questions facing contemporary astronomers: How did magnetic fields come into existence?

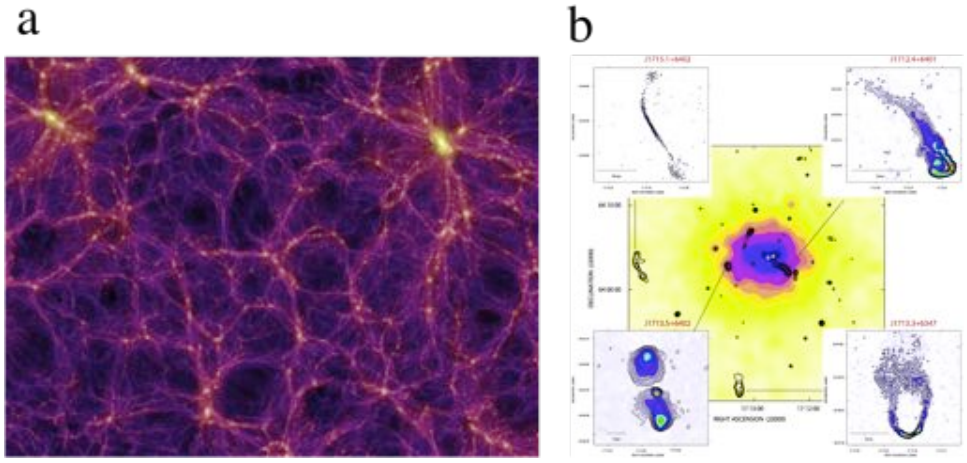

Figure 1: **Large scale structures in the universe are magnetised. a,** At the largest scale, the universe abounds with three types of luminous structures: clusters, filaments, and voids. Clusters (yellow) are groups of galaxies which are bound by gravitational attraction. Filaments (purple) connect clusters across voids (black). This image represents recent data collected by Tully, *et al.* of the Virgo cluster where the Milky Way is located. **b.** Astrophysical data indicates that clusters are magnetised. Shown above is synchrotron radio emission contours that were overlaid on the ROSAT x-ray image of the A255 galaxy cluster. Correlating radiation with Faraday rotation measurements, indicates that galactic clusters have magnetic fields $\sim \mu$G.

Let us begin with a picture of the early universe: Thermal radiation left over from the Big Bang, referred to as the cosmic microwave background (CMB), indicates that matter in the early universe was almost homogeneously distributed – 'almost' being the key word. Gravitational instabilities arising from small perturbations in the mass distribution drove the collapse of matter. As a result, a very ordered universe transformed into a web-like structure of clusters, filaments, and voids as shown in Figure 1(a). As matter began to collapse supersonically, gas accretion onto clusters generated strong shock waves which

began to extend across the universe, bringing with them the elements of which life is made. These shock waves are arguably the birth place of magnetic fields in our universe.

Astrophysical observations confirm that large-scale objects in the universe are magnetised, from clusters $\sim \mu$G to filaments $\sim$ nG to voids $\sim$ 0.1 fG [1]. Clusters are groups of hundreds to thousands of galaxies that are gravitationally attracted to each other and span distances of Mpc; where a parsec is approximately 3 light years or a few trillion miles in length. Wide-diffuse synchrotron emission measurements made by Gionvannini and Feretti in 2002 indicate magnetic fields of 0.1-1 μG in clusters [15]. Faraday rotation measurements of nearby galaxies A2255 were also conducted by Govoni, *et al.* using polarised radio halos at the cluster centre, relic sources at the cluster periphery, and several embedded radio galaxies [2]. They observed average magnetic fields of 2.5 μG across the cluster which compliments synchrotron radiation measurements well. Filaments are some of the largest structures known to humanity– they span distances of 50-80 Mpc and form long, threadlike boundaries between voids in the universe. Filaments are made up of galaxies which form long bands instead of clusters and are observed to be magnetised at about $\sim$ nG.

At the largest scale, voids have a diameter of 11-150 Mpc and contain few, if any, galaxies. Neronov and Vovk measured $\sim$ 0.1 fG fields in 2010 by observing GeV gamma-ray emission from the electromagnetic cascade initiated by tera-electron volt gamma-rays in the intergalactic medium [16]. This is incredibly important because it proves that primordial magnetic fields were created in the very early universe during structure formation. If instead magnetic fields were created long after the formation of clusters, voids would not necessarily support ubiquitous magnetic fields.

The creation of magnetic fields is thought to be a three phase process [6]. In the first phase, primordial 'seed' magnetic fields are created by the Biermann battery mechanism in asymmetrical shock waves due to misaligned density and temperature gradients. These magnetic fields are $\sim 10^{-21}$ G, which is significantly less than current observations. So how

can small seed fields be amplified by several orders of magnitude to the level seen today? The answer is turbulence [5].

In the second phase, Kolmogorov turbulent motions amplify seed magnetic fields 'frozen' into the plasma flow. Since astrophysical environments boast Rm $\sim 10^{27}$, magnetic advection dominates magnetic diffusion. Field lines can begin to stretch, twist, and fold in the presence of turbulence. For a system of fixed volume and minimal magnetic diffusion, an increase in magnetic field strength must be accompanied by a proportional increase in field-line length, indicating the necessity for fields to tangle stochastically. Magnetic fields begin to amplify in this manner until the magnetic energy reaches equipartition with the available kinetic energy of the system. This is the onset of phase three: dynamo, where magnetic field amplification is no longer limited by diffusion. Further discussion of these phenomena can be found in Section 2.5.

It is important to note that an observation of moderate magnetic field amplification (phase two) and the dynamo regime (phase three) have never been observed in a laboratory plasma relevant to astrophysics until now. This thesis will present the first measurements of moderate magnetic field amplification and discuss current experimental efforts led by the author to observe the dynamo effect using the NIF laser.

1.3.1 Astrophysical methods of measuring magnetic fields

As previously stated, astrophysical measurements indicate that the large-scale universe is magnetised. Let us discuss how those magnetic field measurements are made in the universe before proceeding to laboratory experiments. There are two popular methods of measuring magnetic fields in astrophysics: luminosity from synchrotron radiation [17] and polarisation measurements using Faraday rotation [18][19]. Both methods are capable of measuring magnetic fields across large scale (Mpc) objects by cleverly making use of pre-existing sources of radiation.

What are the known sources of radiation in the universe? One source emanates from powerful jets ejected from supermassive black holes which bring with them charged particles. Supermassive black holes arise after the death of a large star (many times larger than our sun) and are typically millions or billions of times more massive than the Sun. Our own Milky Way hosts a supermassive black hole at its centre. As material spiralling along the accretion disk of a black hole approaches the event horizon, it can often be ejected along open field lines to form a supersonic, collimated jet orthogonal to the disk plane. These objects then become known as 'quasars'; or for the more compact (travel-size) case, 'blazars.' However, quasars are not the only source of radiation available in the universe; high energy particles ejected from supernova remnants can also be used for magnetic field measurements across large-scale objects. Observatories such as the Very Large Array (VLA) in New Mexico can collect radio emission originating from synchrotron radiation to determine the magnetic field strength of a particular object. Additionally, radiation can be collected on instruments such as the x-ray telescope at the Chandra observatory, the infrared Spitzer Space Telescope, and the Hubble Space Telescope.

Luminosity from synchrotron radiation can be used to infer the average magnetic field strength across a large object, such as a cluster, in the universe. Synchrotron radiation occurs when high energy particles are accelerated radially in the presence of an imposed magnetic field, releasing photons of corresponding energy. This phenomena was first detected by Geoffrey R. Burbidge in 1956 when the energetic jet Messier 87 was observed to emit strong radiation, shown in Figure 2(a), as predicted by Hannes Alfvén in 1950. The relationship between the luminosity (L_{pop}), otherwise known as the amount of energy emitted per unit time, and the imposed magnetic field (B) of interest, can be described by

$$L_{pop}(\nu) \propto B^{(p+1)/2}\nu^{-(p-1)/2} \tag{1}$$

for a particular frequency, ν, and pitch angle, p. For typical astrophysical measurements

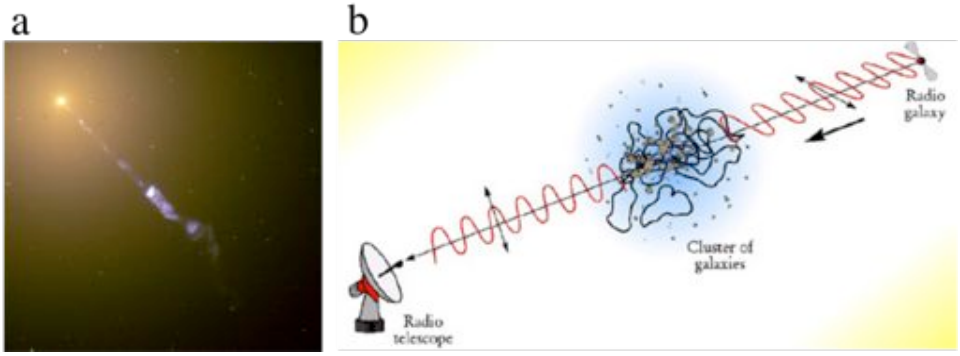

Figure 2: **Known sources of radiation in the universe can be used to measure the magnetic field of large-scale objects. a,** Messier 87 is a radio galaxy located in the northern Virgo Cluster, ∼16 Mpc from Earth. It was discovered in 1781 by Charles Messier and features a supermassive black hole at its core which emits strong radiation. The protruding jet features blue light which is the result of synchrotron radiation. (Image: NASA 2000) **b,** Polarised synchrotron radiation from radio galaxies can be used to diagnose the magnetic field strength of objects in the universe such as clusters. As polarised light enters a region with a magnetic field, the angle of polarisation changes; this is known as Faraday rotation. (Image: P.P. Kronberg 2002)

where B $< 10^{-8}$ T, this expression can be simplified to $L_p \propto B^3$. However, these calculations usually assume: magnetic fields fill the entire radio source; relativistic protons and electrons have equal energy; and a range of frequencies in which the synchrotron luminosity is calculated from 10 MHz to 10 GHz. As a result, it is important to correlate magnetic field measurements with other diagnostics.

Faraday rotation can be used to determine the magnetic field of a large-scale object by observing the rotation of polarised radiation through a volume. The difference in phase velocity between the left and right circularly polarised waves can be measured as an overall rotation of the plane of polarisation. For astrophysical observations, the rotation measurement, RM, can be related to the magnetic field along the line-of-sight, $B_{||}$, by the following equation

$$RM_{[rad/m^2]} = 812 \int_0^{L_{[kpc]}} n_{e[cm^{-3}]} B_{||[\mu G]} dl \tag{2}$$

where n_e is the electron density across the path length, L. This leads to a number of questions.

First, how can we determine the variables n_e and L? The path length is easier to determine. The universe abounds with objects of known luminosity referred to as 'standard candles.' By comparing the object's observed brightness to its known brightness, the path length can be determined. Such standard candles include Type Ia supernovas which always collapse at the same critical mass (1.39 times the solar mass) and therefore shine with the same luminosity every time, approximately 5 billion times brighter than the Sun. Type Ia supernovas are amongst the brightest objects in the known universe and can outshine entire galaxies. Another type of standard candle includes Cepheid variables, a special type of star, which Edwin Hubble used to determine distances of nebulae. The electron density, n_e, distribution in a cluster is typically assumed to take the profile of

$$n_e(r) = n_0(1 + r^2/r_e^2)^{-3\beta/2} \tag{3}$$

where r, n_0, and r_e are the distance from the centroid, the central electron density, and the cluster core radius, respectively. The plasma beta, β, refers to the ratio of the plasma pressure to magnetic pressure. These values can be found through observations. For instance, Govoni, *et al.* derived these values from ROSAT X-ray observations.

Next, one might wonder how the spatial profile of the magnetic field along the line-of-sight can be determined. Astrophysical observations have shown that there is a strong correlation between the gas energy-density profiles and the magnetic energy density profile – in both cases, the energy density decreases from the cluster centre at the same rate. Therefore, the magnetic field can take a similar form to Equation 3 by replacing the electron density with the magnetic field. Now we are armed with the necessary information to determine the magnetic field strength of a large-scale object.

Faraday rotation measurements are typically conducted using microwave radiation in

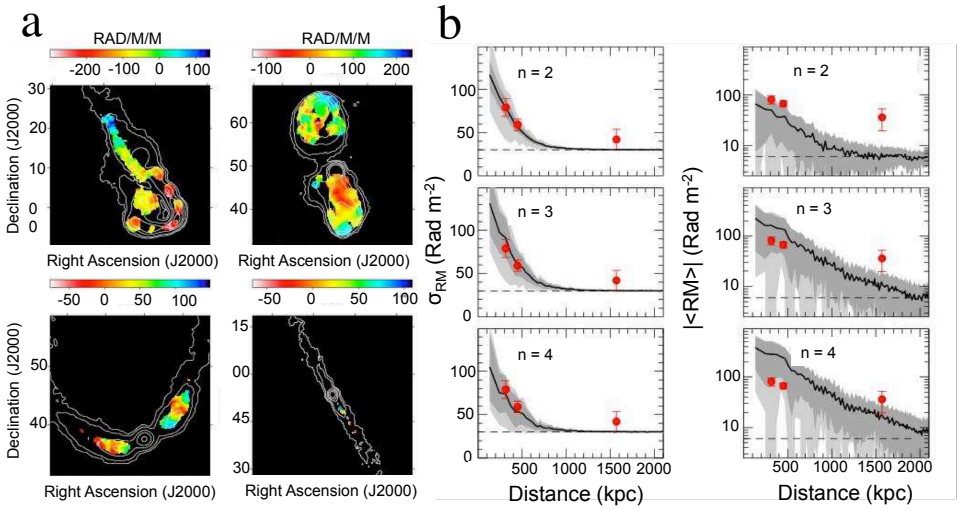

Figure 3: **Faraday rotation measurements indicate the magnetic field strength of astrophysical objects.** **a,** Images of the rotation measurements at four different frequencies 4535, 4885, 8085, and 8465 MHz for the Abell 2255 cluster. These plots indicate that the average magnetic field in clusters $\sim \mu$G. **b,** The magnetic field spectrum can be used to determine the average magnetic field across the cluster. Three radio galaxy measurements were taken to provide three different lines-of-sight for the cluster (red). The magnetic field spectrum was fit to the data using different values of n. (Image: F. Govoni, *et al.* 2008)

order to detect small magnetic fields where B $<$ 1 G. For high frequency radiation moving through a magnetic field, the change in polarisation would be far too small to detect. In practice, astrophysicists do not directly determine the value of B, but instead first measure the magnetic field power spectrum based on the model $|B_k|^2 \propto k^{-n}$ where values of n are used to fit the raw data as shown in Figure 3(b). Furthermore, several Faraday rotation measurements are taken across various different lines-of-sight in order to better understand the 3-dimensional object. All of these measurements are averaged together to determine the average magnetic field strength across a cluster.

1.4 Plasma Dynamics

The surface of our planet is rich in matter of the solid, liquid, and gaseous states. However, most of the visible matter in the known universe falls within a fourth state of matter – plasma. The only naturally occurring sources of plasma near the surface of our planet are found in lightning and the aurora. In a plasma, particles have enough energy to overcome the binding energy which keeps an electron bound to an atom (for instance, 13.6 eV in the case of the ground state of hydrogen). Even though gases are an assembly of particles without a definite shape or volume, plasmas are unique in that they are electrically conductive and can respond strongly to electromagnetic forces. In fact, plasmas exhibit many similar characteristics to fluids in terms of their bulk motions. This section will discuss the fundamental nature of plasmas and then focus on the influence of an applied magnetic field on a plasma.

1.4.1 Definition of a plasma

Around 99% of the readily observed universe is comprised of plasma, from interstellar medium to supernovae and beyond. This fourth state of matter is a quasineutral gas of charged and neutral particles which exhibits collective behaviour [20]. Plasmas are quasineutral in the sense that they are able to shield out, for example, external potentials by rearranging the interior charged particles accordingly. This concept is known as Debye shielding and leaves the majority of the plasma free of large electric fields or potentials while still maintaining small scale electromagnetic forces. The sheath thickness, or Debye length, is given by

$$\lambda_D \equiv \left(\frac{\epsilon_0 k_B T_e}{n e^2} \right)^{1/2} \tag{4}$$

where $n \simeq n_e \simeq n_i$ is the plasma density and T_e is the temperature of the electrons. A convenient form of these equation is $\lambda_D = 743(k_B T_e/n)^{1/2}$ [cm] where $k_B T_e$ is in eV and n

is in cm^3.

In most cases, the electron temperature contributes to the plasma sheath thickness because the electrons are much lighter than the heavy ions. Electrons can therefore move quickly to create a surplus or deficit necessary to shield out electric potentials. In the absence of thermal agitations, $T_e \to 0$, the plasma sheath becomes an infinitely fine layer. The first necessary condition for a plasma is that the plasma sheath must be significantly smaller than the size of the system, $\lambda_D \ll L$. When this condition is met, the interactions in the bulk of the plasma are more important than those at its edges, rendering the plasma quasineutral.

Plasmas demonstrate 'collective behaviour' which means that its motions depend on both the local collisions and the state of the plasma in remote regions. This leads to the second requirement for an ideal plasma, that there are enough particles to create a plasma sheath ($N_D \gg 1$). In fact the number of particles in a Debye sphere is $N_D = (4/3)n\pi\lambda_D^3$ and the plasma is said to be 'ideal' if the number of particles inside the Debye sphere can be taken to approach infinity. Charged particles must be close enough together to influence many nearby particles, not just the closest one. An interesting phenomena occurs in some high-energy-density plasmas called 'collisionless plasmas' where the long-range electromagnetic forces dominate local collisions to point where these collisions can be neglected.

Even though plasmas exhibit collective behaviour, there are small scale electromagnetic forces to consider. For instance, when electrons are displaced from a uniform background of ions, electric fields are set up to restore the charge balance. Electrons quickly move to restore that balance but overshoot due to their inertia. As a result, the electrons oscillate about their equilibrium position at the 'plasma frequency', ω_p, while the massive ions, unable to respond quickly enough, remain relatively stationary. The electron plasma

oscillation is thus described by

$$\omega_p = \left(\frac{n_e e^2}{\epsilon_0 m_e}\right)^{1/2}. \tag{5}$$

It is worth noting here that ω_p does not depend on k, so the group velocity $d\omega/dk$ is zero. This means that the plasma oscillations do not propagate unless the contribution from thermal motions are considered. In this case, we can properly describe electron plasma waves by the following equation

$$\omega^2 = \omega_p^2 + \frac{3}{2}k^2 v_{th}^2 \tag{6}$$

where $v_{th}^2 = 2k_B T_e/m$. Now the electron plasma waves depend on k, so the group velocity can be reduced to $v_g = \frac{3}{2}\frac{v_{th}^2}{v_\phi}$, where $v_\phi = \omega/k$ is the phase velocity.

Using this result, we can discuss the third and final requirement to define a plasma. For an ionised gas to behave as a plasma rather than a neutral gas, we require $\omega\tau > 1$ where τ is the mean time between collisions and ω is the frequency of typical plasma oscillations. For example, a weakly ionised gas in a jet exhaust does not qualify as a plasma because the charged particles collide so frequently with neutral atoms that their motion is controlled by ordinary hydrodynamic forces rather than by electromagnetic forces. In summary, there are three parameters which must be fulfilled: (1) $\lambda_D \ll L$, (2) $N_D \gg 1$, and (3) $\omega\tau > 1$.

1.4.2 Single-particle motions

Plasmas sometimes behave like a fluid, where collisions dominate and simple equations of ordinary fluid dynamics are sufficient, and other times behave like a collection of individual particles, where the motion of a single particle becomes important [21]. In any case, plasmas tend to disperse, allowing individual particles to travel at high velocities away from their source, rendering the plasma obsolete. However, plasmas can be sustained by providing a restraining force by means of an external magnetic field.

In the presence of a uniform external magnetic field, $\mathbf{B}$, a particle undergoes cyclotron gyration to generate its own opposing magnetic field. In the absence of an electric field, the Lorentz force for a charged particle, q, moving at a velocity $\mathbf{v}$, can be described by $m\frac{d\mathbf{v}}{dt} = q\mathbf{v} \times \mathbf{B}$. It then follows that the cyclotron frequency describing the orbit of a charged particle in a uniform magnetic field is

$$\omega_c \equiv \frac{|q|B}{m}. \tag{7}$$

The physical description here is that the external magnetic field provides a centripetal force which holds an otherwise free electron in a circular perpendicular motion. In fact, if the centripetal force is set equal to the Lorentz force,

$$\frac{mv_\perp^2}{r_L} = |q|v_\perp B \tag{8}$$

$$r_L \equiv \frac{v_\perp}{\omega_c} = \frac{mv_\perp}{|q|B} \tag{9}$$

the equilibrium distance of a charged particle can be calculated. This radius of curvature, r_L, is called the Larmor radius. In a weak magnetic field, a particle only slightly deviates from its path, resulting in a large Larmor radius. Similarly, a highly energetic particle is not easily deflected by an external magnetic force, resulting in a large Larmor radius.

A charged particle in a uniform magnetic field moves in a helical path about a point, or 'guiding centre', that moves with constant velocity parallel to the magnetic field. If an observer were to look down on this circularly rotating particle, the particle would appear to pass a given point every $2\pi r_L/v_\perp$ seconds, generating a current of $I = |q|v_\perp/2\pi r_L$. The associated magnetic moment that acts to oppose the applied field B, is

$$\mu = \pi r_L^2 I = \frac{mv_\perp^2}{2B}. \tag{10}$$

If additionally, there is a non-magnetic force acting on the particle, the guiding centre begins to drift. One of the most common cases is an applied electric field **E**. From Lorentz's law, $m\frac{d\mathbf{v}}{dt} = q\mathbf{E} + q\mathbf{v} \times \mathbf{B}$, the velocity of the guiding centre drift can be described by

$$\mathbf{v_d} = \frac{\mathbf{E} \times \mathbf{B}}{B^2}. \tag{11}$$

Equation 11 implies that the drift of a particle in an applied electric field is independent of the charge, mass, and velocity. To understand this concept, let's look at the physical picture depicted in Figure 4(b). In the first half-cycle of an electron, the particle gains energy from the electric field, increasing the velocity, resulting in a large Larmor radius, r_L. During the second half of the cycle, the particle loses energy, resulting in a much smaller r_L and an overall drift of the guiding centre. Heavy ions have a larger Larmor radius which means they can drift more in each cycle. However, the ions will have a smaller gyration frequency than the lighter electrons, resulting in fewer cycles. As a result, the drift velocity is equivalent for both ions and elections.

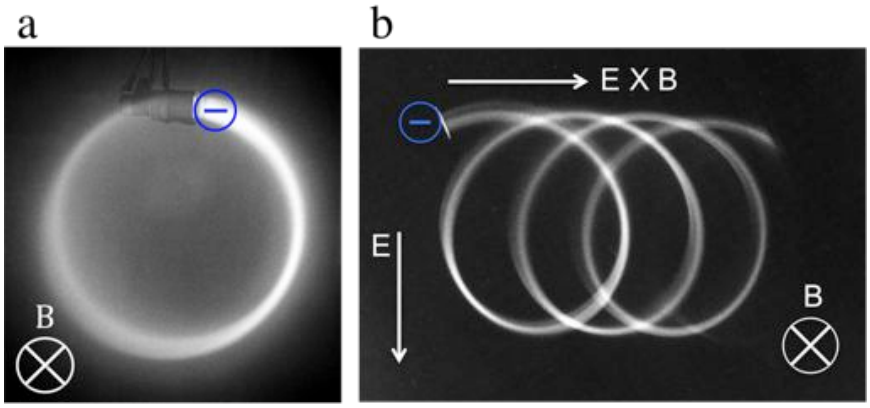

Figure 4: **Single-particle motion in a magnetic field. a,** A particle undergoes cyclotron gyration when moving through a uniform magnetic field. The radius of curvature is known as the Larmor radius. **b,** When a particle is exposed to both a uniform magnetic and electric field, the particle's guiding centre drifts. (Image: R. L. Stenzel 2004)

In laboratory systems, plasmas are frequently subjected to non-uniform magnetic fields which can quickly lead to mathematically convoluted problems. In the simplest case, if a particle is moving in a uniform magnetic field, $\mathbf{B}$, and then exposed to a non-uniform magnetic field ∇B perpendicular to $\mathbf{B}$, the particle will begin to drift according to the following equation

$$\mathbf{v}_{\nabla \mathbf{B}} = \pm \frac{1}{2} v_{\perp} r_L \frac{\mathbf{B} \times \nabla B}{B^2}. \tag{12}$$

The direction of the drift velocity now depends on the particle's charge which accounts for the $\pm$ sign. As a particle moves in a nonuniform magnetic field, the cyclotron frequency adjusts accordingly, resulting in fluctuations of the Larmor radius.

Another simple case to consider is $\nabla B || \mathbf{B}$, a particle moving in a non-uniform magnetic field which is parallel to $\mathbf{B}$. In the field of plasma confinement, this leads to a phenomena known as a 'magnetic mirror.' If a particle is moving in the same direction as the varying magnetic field, it will feel a force,

$$\overline{F}_z = -\frac{1}{2} \frac{m v_{\mp}^2}{\mathbf{B}} \frac{\partial \mathbf{B_z}}{\partial z}. \tag{13}$$

The interesting thing about this variation of the applied magnetic field, is that the magnetic moment takes the same form as Equation 10. This implies a number of important conclusions. As a particle moves into a region of stronger or weaker magnetic field, $\mathbf{B}$, its Larmor radius necessarily changes. However, the magnetic moment, μ, remains invariant – this preserves energy conservation. If a particle were to move from a weak magnetic field region to a strong magnetic field region, it would see an increase in $\mathbf{B}$ which means $v_{\perp}$ would need to equally increase resulting in a larger Larmor radius. Physically, this means that if a large enough magnetic field were applied, the particle would reach $v_{||} = 0$ and reflect back to a weaker field region. This is the basic concept of plasma confinement.

There is an exhaustive list of applied field variations that could be discussed, but

hopefully this will give a flavour of the effects fields can have on a plasma. The main goal was to establish that magnetic fields have a profound effect on plasmas, and the motions of individual particles can be used to understand the dynamics of a plasma.

1.4.3 Plasmas as fluids

Now we will transition from looking at individual particles to looking at the behaviour of the plasma as a whole. Since typical plasma densities in our experiments are $\sim 10^{17}$ cm^{-3}, it is particularly fortunate that we can crudely understand the behaviour of a plasma without having to look at each and every particle individually. Here we adopt the fluid equations of motion. If we refer back to Lorentz's law which describes the motion of particles in the frame of reference of the particle, we now want an equation which will represent the dynamics of an element fixed in space. Therefore, the convective derivative is an appropriate substitution, and Lorentz's law takes the following form

$$mn\left[\frac{\partial \mathbf{v}}{\partial t} + (\mathbf{v}\cdot\nabla)\mathbf{v}\right] = qn(\mathbf{E} + \mathbf{v}\times\mathbf{B}) \tag{14}$$

where $\mathbf{v}$ is the plasma fluid velocity. In Equation 14 the first term is the change in fluid velocity from a *fixed frame* of reference while the second term is in the *moving frame* of reference of the particle. Now we can apply this result to the fluid equations in Chapter 2.

1.5 Organisation of this thesis

This thesis is divided into six sections and focuses on the two most prominent discoveries made by the author and team. The introduction, **Chapter 1**, is intended to provide motivation and background information for the experiments presented in this thesis. **Chapter 2** will cover hydrodynamics and magnetohydrodynamics relevant to laser-produced plasmas. The physics of shock waves will be introduced, and a link will be made between

astrophysical plasmas and laboratory plasmas. This is when scaling laws become important. Furthermore, the topic of laser-matter interactions will be discussed before proceeding onto the next chapter where diagnostic tools will be applied to laser-plasma experiments. Amongst the most important topics in Chapter 2 include the mechanisms for magnetic field generation and amplification by turbulent motions.

Once the theoretical background has been established, we will move onto the instrumentation and experimental methods of studying laser-produced plasmas in **Chapter 3**. A discussion about high-power lasers will set the stage for experiments. There will be a discussion about the diagnostic tools used to understand plasma conditions and transient magnetic fields. It is worth noting that for most of the author's experiments, she used optical diagnostics and has a strong understanding of how to setup and implement these tools.

Chapters 4 and 5 will discuss the two major experimental results. **Chapter 4** will focus on the first observations of magnetic field amplification in laser-produced shock waves relevant to supernova remnants. **Chapter 5** will take this result a step further by introducing measurements of non-linear amplification of magnetic fields, a precursor to turbulent dynamo, in laser-produced jets relevant to cluster-merger events. In both cases, a detailed description of the experimental setup and diagnostic tools will be presented. Both experiments were conducted during the same 5-week Vulcan experiment, so the setups and plasma environments are similar. The major results from both experiments will be presented along with the astrophysical relevance and impact on the astrophysical community.

This thesis will conclude in **Chapter 6** with a discussion of the next steps forward. The author is currently on experiment with a team of international scientists looking to create turbulent dynamo for the first time in laser-produced plasma at the National Ignition Facility. A brief discussion of the experimental setup and goals will be presented. The team hopes to make the first observations of turbulent dynamo, the 'holy grail' of laboratory

astrophysics, to make a more complete story of evolution of magnetic fields in the universe.

1.6 Contributors

Induction coils, or 'Bdot' probes, were one of the primary diagnostics for the laboratory study of magnetogenesis. The concept and design was derived from Everson, *et al.* but modified for these experiments by the author, A. Baird, and G. Gregori. Each probe was handmade by the author under the guidance and support of A. Baird. Newer models feature a 0.5 mm diameter core which was engineered by C. Spindloe of Target Fabrication at the Rutherford Appleton Laboratory (RAL). Each probe was calibrated by the author using the laboratory space and equipment at the University of Oxford. The method of calibration was devised by both the author and C. D. Murphy. For most experiments, data collected by the Bdot probes was analysed by the author, and investigation into the proper method of analysing Bdot data was lead by the author and G. Gregori. Additional input and useful conversations came from H. Doyle and L. Z. Liu.

The experiments presented in this thesis were carried out at large laser facilities which required substantial help from collaborators. It is common with these types of collaborations to have a team of 20-30 people: about a dozen scientists present for the experiment, several involved with the conceptual support, and a simulations team. These experiments are ultimately a team effort and all collaborators should be deeply acknowledged for their efforts, regardless of the size. To that effect, it is important to highlight the author's contributions to justify sufficient work, worthy of a Doctor of Philosophy degree– these contributions are detailed in the following papers.

Investigation into laser-produced shock waves:

"Turbulent amplification of magnetic fields in laboratory laser-produced shock waves"

Meinecke, *et al.* **Nature Physics** 2014.

The project was conceived by G. Gregori, D. Q. Lamb, B. Reville, and F. Miniati. The design was lead by the author, G. Gregori, B. Reville, C. D. Murphy, R. Bingham, A. A. Schekochihin, N. C. Woolsey, and R. P. Drake. The experiment and data analysis was lead by the author and H. W. Doyle using the Vulcan Target Area West laser. The facility provided considerable technical help, especially from R. J. Clarke, M. Notley, and R. Heathcote. The experiment was carried out by the author, H. W. Doyle, M. J. MacDonald, R. Crowston, C. C. Kuranz, A. Pelka, and W. C. Wan. The subsequent paper was written by the author, G. Gregori, H. W. Doyle, A. A. Schekochihin, A. R. Bell, D. Q. Lamb, P. Tzeferacos, and B. Reville. The data was analysed by the author and H. W. Doyle. Numerical simulations were performed by P. Tzeferacos. Further experimental and theoretical support was provided by R. Bingham, R. P. Drake, M. Fatenejad, M. Fatenejad, M. Koenig, Y. Kuramitsu, D. Lee, H.-S. Park, A. Ravasio, Y. Sakawa, A. Scopatz, P. Tzeferacos, N. C. Woolsey, and R. Yurchak.

Investigation into laser-produced jets:

"Developed turbulence and non-linear amplification of magnetic fields in laboratory and astrophysical plasmas" Meinecke, *et al.* **PNAS** 2015.

The project was conceived by G. Gregori, D. Q. Lamb, A. A. Schekochihin, B. Reville, and F. Miniati. The design was lead by the author, G. Gregori, B. Reville, C. D. Murphy, R. Bingham, A. A. Schekochihin, N. C. Woolsey, and R. P. Drake. The experiment and data analysis was lead by the author and H. W. Doyle using the Vulcan Target Area West laser. The facility provided considerable technical help, especially from R. J. Clarke, M. M. Notley, and R. Heathcote. The experiment was carried out by the author, H. W. Doyle, M. J. MacDonald, R. Crowston, C. C. Kuranz, A. Pelka, W. C. Wan, R. J. Clarke, R. Heathcote, and M. M. Notley. The subsequent paper was written by the author, G. Gregori,

H. W. Doyle, A. A. Schekochihin, A. R. Bell, D. Q. Lamb, P. Tzeferacos, and B. Reville. The data was analysed by the author, H. W. Doyle, and E. M. Churazov. Numerical simulations were performed by P. Tzeferacos. Further experimental and theoretical support was provided by R. Bingham, R. P. Drake, M. Fatenejad, M. Koenig, Y. Kuramitsu, D. Lee, H.-S. Park, A. Ravasio, Y. Sakawa, A. Scopatz, P. Tzeferacos, N. C. Woolsey, and R. Yurchak.

Other investigations into laboratory astrophysics:

The author participated in a number of experiments during her postgraduate years which are not the main focus of this thesis but played an important role in preparations for her experiments at RAL. Some of the data and analysis from these experiments have been incorporated into this thesis.

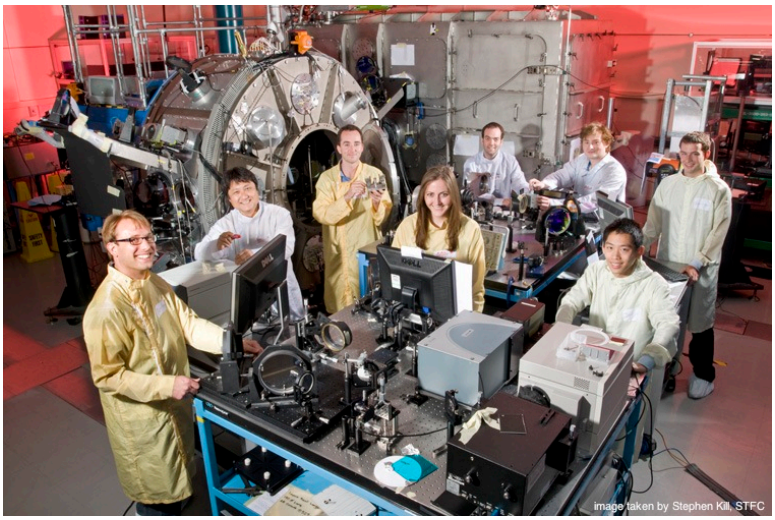

Figure 5: **The experimental team inside the Vulcan laser target area at RAL.** The two main experiments presented in this thesis, on laser-produced shock waves and jets, were conducted by this group of individuals in May 2012. The cylindrical target chamber is pictured in the back and the optical diagnostics are shown setup on the two adjacent tables.

1.6.1 Publications and Honours

The experimental result presented in Chapter 4 was named one of the Top Ten Breakthroughs of 2014 by *Physics World* and featured in several television programmes including The Science Channel's *How the Universe Works* and BBC Four's *Sky at Night* programme. The research discoveries in Chapter 4 made the front cover of BBC's *Sky at Night* magazine ("How to Make a Supernova") and the discoveries in Chapter 5 were featured in *Physics Today* magazine. For her efforts during postgraduate studies, the author was named the Institute of Physics (IOP) Very Early Career Female Physicist of the Year (2015), the American Physical Society (APS) Woman Physicist of the Month (October 2014), and finalist for the Women of the Future: Science Award (2014). The publications listed in this section represent research efforts made by the author during her postgraduate time at the University of Oxford. She presented this work at 15 conferences, of which 6 were oral presentations (3 invited talks).

1. **J. Meinecke**, P. Tzeferacos, A. R. Bell, R. Bingham, E. M. Churazov, R. Crowston, H. Doyle, R. P. Drake, M. Koenig, Y. Kuramitsu, C. C. Kuranz, D. Lee, M. J. MacDonald, C. D. Murphy, H.-S. Park, A. Pelka, A. Ravasio, B. Reville, Y. Sakawa, W. C. Wan, N. C. Woolsey, R. Yurchak, F. Miniati, A. A. Schekochihin, D. Q. Lamb, and G. Gregori, *Developed turbulence and non-linear amplification of magnetic fields in laboratory and astrophysical plasmas,* PNAS, **112**, 8211-8215 (2015).

2. **J. Meinecke**, H. W. Doyle, F. Miniati, A. R. Bell, R. Bingham, R. Crowston, R. P. Drake, M. Fatenejad, M. Koenig, Y. Kuramitsu, C. C. Kuranz, D. Q.Lamb, D. Lee, M. J. MacDonald, C. D. Murphy, H-S. Park, A. Pelka, A. Ravasio, Y. Sakawa, A. A. Schekochihin, A. Scopatz, P. Tzeferacos, W. C. Wan, N. C. Woolsey, R. Yurchak, B. Reville, and G. Gregori, *Turbulent amplification of magnetic fields in laboratory laser-produced shock waves,* Nature Physics, **10**, 520-524 (2014).

3. H-S. Park, C. M. Huntington, F. Fiuza, R. P. Drake, D. H. Froula, G. Gregori, M. Koenig, N. L. Kugland, C. C. Kuranz, D. Q. Lamb, M. C. Levy, C. K. Li, **J. Meinecke**, T. Morita, R. D. Petrasso, B. B. Pollock, J. S. Ross, D. D. Ryutov, Y. Sakawa, A. Spitkovsky, B. A. Remington, H. G. Rinderknecht, M. Rosenberg, H. Takabe, D. P. Turnbull, P. Tzeferacos, S. V. Weber, and A. B. Zylstra, *Collisionless shock experiments with lasers and observation of Weibel instabilities,* Phys. Plasmas, **22**, 056311 (2015).

4. C. Huntington, F. Fiuza, J. S. Ross, A. Zylstra, R. P. Drake, D. H. Froula, G. Gregori, N. L. Kugland, C. C. Kuranz, M. Levy, C. Li, **J. Meinecke**, T. Morita, R. Petrasso, C. Plechaty, B. A. Remington, D. Ryutov, Y. Sakawa, A. Spitkovsky, H. Takabe, and H-S. Park, *Observation of magnetic field generation via the Weibel instability in interpenetrating plasma flows,* Nature Physics, **11**, 173-176 (2015).

5. E. R. Tubman, R. Crowston, R. Alraddadi, H. W. Doyle, **J. Meinecke**, J. E. Cross, R. Bolis, D. Q. Lamb, P. Tzeferacos, D. Doria, B. Reville, H. Ahmed, M. Borghesi, G. Gregori, N. C. Woolsey, *Nanosecond Imaging of Shock- and Jet-Like Features,* IEEE, **42**, 2496-2497 (2014).

6. N. L. Kugland, J. S. Ross, P.-Y. Chang, R. P. Drake, G. Fiksel, D. H. Froula, S. H. Glenzer, G. Gregori, M. Grosskopf, C. Huntington, M. Koenig, Y. Kuramitsu, C. C. Kuranz, M. C. Levy, E. Liang, D. Martinez, **J. Meinecke**, F. Miniati, T. Morita, A. Pelka, C. Plechaty, R. Presura, A. Ravasio, B. A. Remington, B. Reville, D. D. Ryutov, Y. Sakawa, A. Spitkovsky, H. Takabe, H.-S. Park, *Visualizing electromagnetic fields in laser-produced counter-streaming plasma experiments for collisionless shock laboratory astrophysics,* Phys. Plasmas, **20**, 056313 (2013).

7. M. J. Grosskopf, R. P. Drake, C. C. Kuranz, E. M. Rutter, J. S. Ross, N. L. Kugland, C. Plechaty, B. A. Remington, A. Spitkovsky, L. Gargate, G. Gregori, A. Bell, C.D. Murphy, **J. Meinecke**, B. Reville, Y. Sakawa, Y. Kuramitsu, H. Takabe, D.H. Froula,

G. Fiksel, F. Miniati, M. Koenig, A. Ravasio, E. Liang, W. Fu, N. Woolsey, and H.-S. Park, *Simulation of laser-driven, ablated plasma flows in collisionless shock experiments on OMEGA and the NIF,* High Energy Density Physics, **9** (1), 192-197 (2013).

8. A. Scopatz, M. Fatenejad, N. Flocke, G. Gregori, M. Koenig, D. Q. Lamb, D. Lee, **J. Meinecke**, A. Ravasio, P. Tzeferacos, K. Weide, and R. Yurchak, *FLASH hydrodynamic simulations of experiments to explore the generation of cosmological magnetic fields,* High Energy Density Physics, **9** (1), 75-81 (2013).

9. M. Fatenejad, A. R. Bell, A. Benuzzi-Mounaix, R. Crowston, R. P. Drake, N. Flocke, G. Gregori, M. Koenig, C. Krauland, D. Lamb, D. Lee, J. R. Marques, **J. Meinecke**, F. Miniati, C.D. Murphy, H.-S. Park, A. Pelka, A. Ravasio, B. Remington, B. Reville, A. Scopatz, P. Tzeferacos, K. Weide, N. Woolsey, R. Young, and R. Yurchak, *Modeling HEDLA magnetic field generation experiments on laser facilities,* High Energy Density Physics, **9** (1), 172-177 (2013).

10. N. L. Kugland, D. D. Ryutov, P-Y. Chang, R. P. Drake, G. Fiksel, D. H. Froula, S. H. Glenzer, G. Gregori, M. Grosskopf, M. Koenig, Y. Kuramitsu, C. Kuranz, M. C. Levy, E. Liang, **J. Meinecke**, F. Miniati, T. Morita, A. Pelka, C. Plechaty, R. Presura, A. Ravasio, B. A. Remington, B. Reville, J. S. Ross, Y. Sakawa, A. Spitkovsky, H. Takabe and H-S. Park, *Self-organized electromagnetic field structures in laser-produced counter-streaming plasmas,* Nature Physics, **8**, 809-812 (2012).

11. J. S. Ross, S. H. Glenzer, P. Amendt, R. Berger, L. Divol, N. L. Kugland, O. L. Landen, C. Plechaty, B. Remington, D. Ryutov, W. Rozmus, D. H. Froula, G. Fiksel, C. Sorce, Y. Kuramitsu, T. Morita, Y. Sakawa, H. Takabe, R. P. Drake, M. Grosskopf, C. Kuranz, G. Gregori, **J. Meinecke**, C. D. Murphy, M. Koenig, A. Pelka, A. Ravasio, T. Vinci, E. Liang, R. Presura, A. Spitkovsky, F. Miniati, and H.-S. Park, *Characterizing counter-streaming interpenetrating plasmas relevant to astrophysical*

collisionless shocks, Phys. Plasmas, **19**, 056501 (2012).

12. P. Tzeferacos, M. Fatenejad, N. Flocke, G. Gregori, D.Q. Lamb, D. Lee, **J. Meinecke**, A. Scopatz, and K. Weide, *FLASH magnetohydrodynamic simulations of shock-generated magnetic field experiments,* High Energy Density Physics, **8** (4), 322-328 (2012).

Chapter 2

Theoretical Background

2.1 Description of Shock waves

A shock wave is an abrupt, surface discontinuity propagating through a medium at speeds faster than the speed of sound. It is characterised as a sudden change in density and temperature while preserving fundamental conservation laws. In addition, a shock wave carries energy upstream while heating and accelerating medium as it passes.

To understand the nature of shock waves, it is worth reviewing that the speed of sound is the group velocity at which longitudinal waves propagate through a material via elastic collisions. Longitudinal waves can be characterised by compression and decompression in the direction of travel. The speed of sound is thus defined as $\sqrt{K/\rho}$ where K, the bulk modulus, represents the compressibility of the material and ρ is the density. For an ideal gas, this relation can be further reduced to $c_s = (\gamma kT/m)^{1/2}$, where γ is the adiabatic index $1 + \frac{2}{f} \approx 1.67$ for monoatomic molecules with f degrees of freedom, k is Boltzmann's constant, T is the absolute temperature in Kelvin, and m is the molecular mass of the gas. This means the speed of sound in an ideal gas, where elastic collisions conserve the total kinetic energy of the system, depends directly on temperature rather than pressure and density.

2.1.1 Jump Conditions and Shock Relations

When the velocity of an expanding material exceeds the speed of sound in a medium, information can not be transmitted fast enough through typical elastic collisions. The material then 'forces' the information to propagate at supersonic speeds resulting in the formation of a shock wave. The nature of this shock wave can be determined from Euler's equations [12] assuming conservation of energy, momentum, and mass by Newton's second law of motion. Neglecting viscosity and heat conduction,

$$\textbf{Continuity:} \qquad \frac{\partial \rho}{\partial t} = -\nabla \cdot (\rho \mathbf{v}), \tag{15}$$

$$\textbf{Momentum:} \qquad \frac{\partial}{\partial t}(\rho \mathbf{v}) = -\nabla \cdot (\rho \mathbf{v}\mathbf{v}) - \nabla P, \tag{16}$$

$$\textbf{Energy:} \qquad \frac{\partial}{\partial t}\left(\frac{\rho v^2}{2} + \rho\epsilon\right) = -\nabla \cdot \left[\rho \mathbf{v}\left(\epsilon + \frac{v^2}{2}\right) + P\mathbf{v}\right] \tag{17}$$

where P is the scalar hydrodynamic pressure and ϵ is the internal energy per unit mass. If we consider the rest frame of the shock, then the mass flow lagging the shock front must be equal to the mass flow leading the shock front, $\rho_0 v_0 A_0 = \rho_1 v_1 A_1$. For an infinitesimal region, A_0 can be taken equal to A_1. Extending this approach to all the conservation equations, we find that

$$\rho_0 v_0 = \rho_1 v_1, \tag{18}$$

$$\rho_0 {v_0}^2 + P_0 = \rho_1 {v_1}^2 + P_1, \quad \text{and} \tag{19}$$

$$\left[\rho_0 v_0\left(\epsilon_0 + \frac{{v_0}^2}{2}\right) + P_0 v_0\right] = \left[\rho_1 v_1\left(\epsilon_1 + \frac{{v_1}^2}{2}\right) + P_1 v_1\right]. \tag{20}$$

A schematic diagram of this phenomena in the frame of reference of the shock is shown in Figure 6. Note the shock velocity is $v_{shock} = -v_0$ in this diagram, and it is the rate at which upstream material reaches the shock.

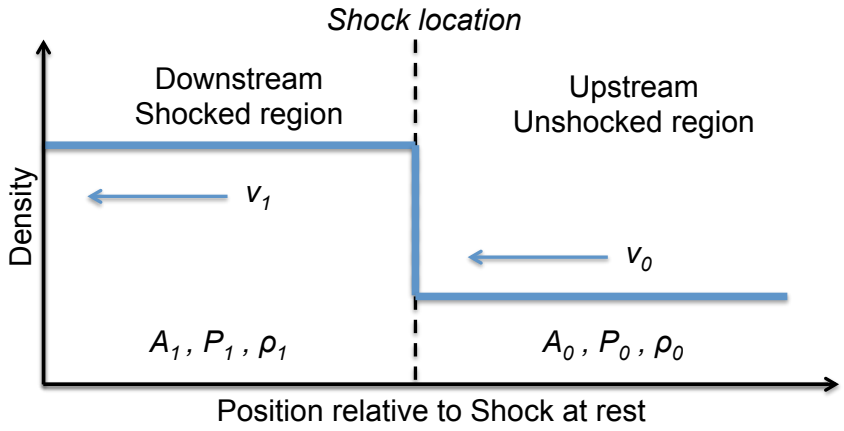

Figure 6: **Diagram of a shock wave characterised by a sudden change in density at the shock front.** Here the shock wave is considered stationary as background material moves from right to left.

If one assumes the fluid to be a polytropic gas where $PV^\gamma = constant$, then the equation of state of the internal energy follows the relation $\rho\epsilon = P/(\gamma - 1)$. The Mach number associated with the shock velocity is $M = -v_0/c_s = v_{shock}/c_s$. After some algebraic manipulation,

$$\frac{\rho_1}{\rho_0} = \left[\frac{P_1(\gamma+1) + P_0(\gamma-1)}{P_0(\gamma+1) + P_1(\gamma-1)}\right], \quad \text{and} \tag{21}$$

$$\lim_{P_1 \gg P_0} \frac{\rho_1}{\rho_0} = \frac{(\gamma+1)}{(\gamma-1)}, \tag{22}$$

which only depends on the adiabatic index γ. For an ideal monatomic gas, for which $\gamma \sim 5/3$, the density jump for a 'strong shock' is 4. Many high-energy-density physics experiments conducted at laser facilities, including the laser-produced shocks presented in Chapter 4, generate 'strong' shocks. Collisionless shocks can also occur in magnetised shocks when the mean free path for collision is larger than the Larmor radius. Experiments are currently underway to characterise such phenomena, but further discussion will go beyond the scope of this thesis.

2.1.2 Blastwaves: Energy Conservation and Sedov-Taylor Regime

When the original source of pressure ends, a rarefaction wave propagates forward to overtake the shock wave and forms a 'blast wave'. A shock wave with a constant source of pressure is analogous to a piston pushing material through a tube. The material near the piston is compressed and a shock wave propagates forward. If the piston is removed, material can then expand in both the forward and backward directions. The material propagating away from the shock will now see a decrease in density caused by the removal of the piston. As it flows from high to low density, a 'rarefaction wave' forms. Rarefaction waves are characterised by decompression in the sense that a spring recoils after being compressed. The rarefaction wave begins to travel in a direction opposing the expanding material but in the direction of the previously formed shock wave. Rarefaction waves behave as a free expansion and have a linear velocity profile: $M = 1 + x/c_s t$. Shortly, it catches up to the shock, compressing the envelope to form a blast wave. Blast waves are associated with a narrower peak in density and temperature than a typical shock wave.

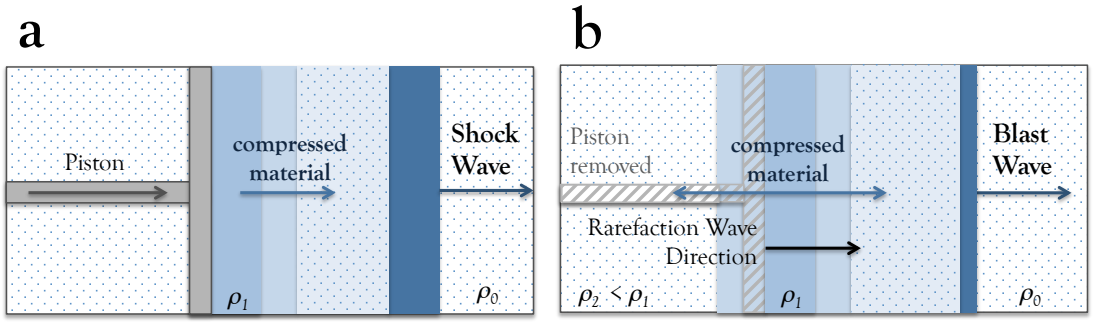

Figure 7: **Formation of shock waves and blast waves. a,** A shock wave is formed by a constant source of pressure, depicted here by a piston. **b,** However, a blast wave only forms when the source of compression (the piston) is removed, allowing the material to expand in both directions.

The energy associated with a blast wave in a polytropic gas with negligible losses to radiation and heat conduction is

$$E = M\left(\frac{2}{\gamma+1}\right)^2 \dot{R}^2, \tag{23}$$

where $\dot{R}$ is the shock velocity and $M = 4\pi\rho R^3/3$ for a spherical blast wave in an external medium of mass density ρ. The mass, M, is swept up by the leading strong shock which converts half of the incoming energy to kinetic energy and the other half into thermal energy. The Sedov-Taylor regime [12] occurs for point-like explosions typical in laser plasma experiments where a fast release of energy is deposited. Using Equation 23, energy conservation laws, and relevant transformation laws, the position of the blast wave can be described as

$$R = \frac{1}{Q}\left(\frac{E}{\rho_0}\right)^{1/5} t^{2/5}, \tag{24}$$

where E is the explosion energy and ρ_0 is the initial density of the surrounding material. For $\gamma = 5/3$ the constant Q has a value of 0.868. The Sedov-Taylor relations can apply to astrophysical shock waves [22] that emanate from a point-explosion such as supernova remnants that develop over hundreds to thousands of years (Section 2.6). It should be noted however, that the mechanism for driving shock waves in the laboratory is different from driving supernova remnants in the universe. Laboratory shock waves result from the instantaneous irradiation of a target by laser light whereas supernova remnants are generated by the gravitational collapse of a dying star. Though the mechanisms for generating the two blast waves are different, once formed, the resultant shocks behave in similar ways that allow for an astrophysical scaling of the laboratory plasma.

2.2 Formation of Astrophysical and Laser-produced Jets

A jet is a collimated bow shock that exhibits faster moving material along the flow axis and slower moving material concentrated at the edges [12][23]. A source generates a high Mach number jet that flows into an ambient medium, as depicted in Figure 8. This launches a bow shock into the ambient medium, leaving behind a shocked jet region labelled as the 'cocoon'. Along the contact discontinuity, entrainment of the ambient material occurs due to the Kelvin-Helmholtz instability along the edges of the jet. This results in slower yet higher luminosity material at the edges of the jet while the Kelvin-Helmholtz instability also generates vorticies and eddies along the contact discontinuity. Whenever two fluid regions flow past one-another, with a sufficiently narrow transition region at their mutual boundary (shear layer), fluctuations at the boundary are unstable and will grow– known as the Kelvin-Helmholtz instability. However, in the laser-produced jets in Chapter 5, the magnetic field is generated primarily by misaligned density and temperature gradients– the Biermann battery mechanism discussed in Section 2.4.

Laboratory jets can be generated using high-powered lasers. In some experiments, sophisticated foam tube assemblies or conical targets can drive jets. In the experiments presented in Chapter 5, the conical laser configuration incident upon a flat foil provided the pinching effect needed to generate a collimated jet. In comparison, astrophysical jets are emitted along the axis of rotation of a compact object with a deep gravitational well. Objects such as black holes and young stellar objects, surrounded by an accretion disk, periodically emit bipolar jets orthogonal to the accretion surface. These jets acquire mechanical energy from the gravitational binding energy of the system by exerting an external magnetic torque upon release from the central body [24]. Furthermore, astrophysical jets are different from laser-produced jets in that they carry an intrinsic magnetic field. Mate-

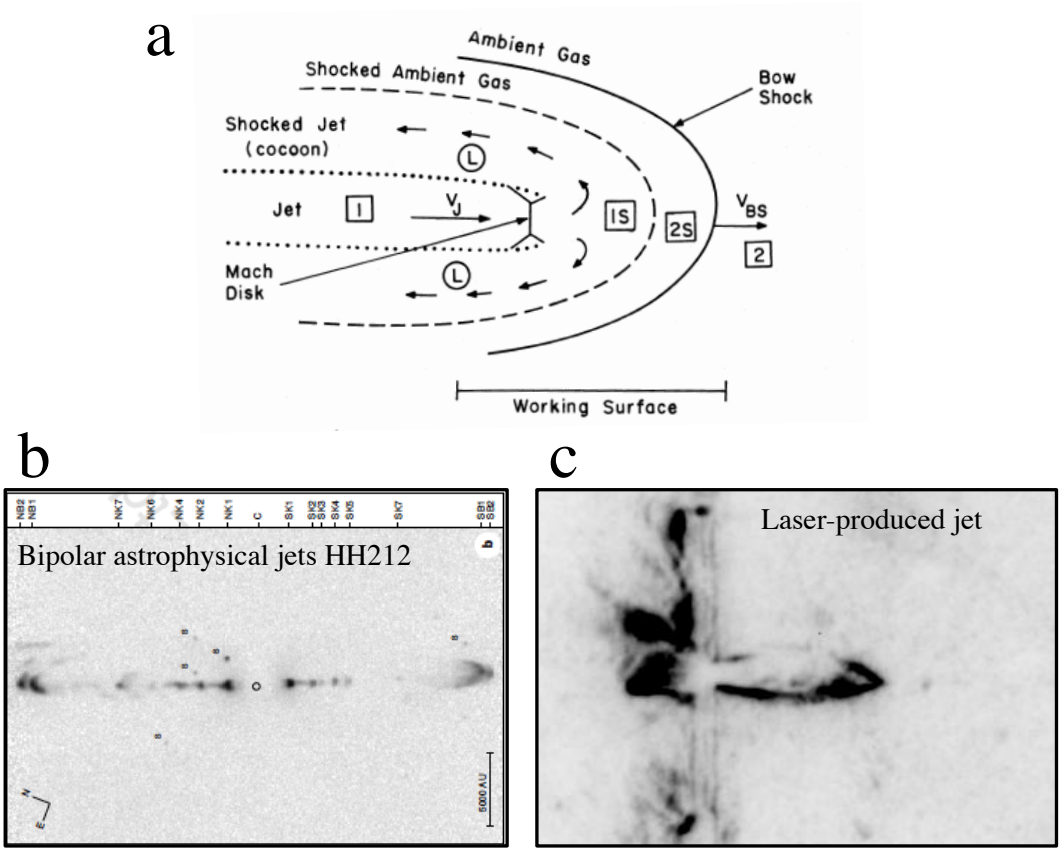

Figure 8: **Formation of astrophysical and laser-produced jets. a,** Schematic of the jet (1) as it expands into an ambient medium (2), driving a bow shock of velocity v_{BS}. The shocked ambient gas left behind (2s) has a contact discontinuity (dashed line) with the shocked jet region (1s) where Kelvin-Helmholtz instabilities drive vorticies and eddies. **b,** Bipolar astrophysical jets emanate from compact objects surrounded by accretion disks. Shown in the Herbig-Haro object HH212 from an Orion protostar (Zinnecker, *et al.* 1998). **c,** Laser-produced jets, though not emanating from a deep gravitational well, have similar characteristics.

rial within the accretion disk co-rotates with a threading magnetic field and occasionally material is ejected along open field lines. Upon release from the compact object, the astrophysical jet carries a toroidal and poloidal magnetic field that collimate the feature. For these reasons, the work presented will not feature an astrophysical scaling to jets, but instead, Chapter 5 will focus on the astrophysical relevance of the turbulent structures generating from the collision of two laser-produced jets.

2.3 Magnetohydrodynamics

Magnetohydrodynamics (MHD) is the study of magnetic field dynamics in an electrically conducting fluid, such as a plasma, where the macroscopic, hydrodynamic equations are applied. In particular, ideal MHD equations [21] are invoked for plasmas that are: (1) strongly collisional so that the time scale of collisions is shorter than the characteristic time scale of the system, leading to a Maxwellian distribution of particles; (2) resistivity due to collisions is small; and (3) the system length scales are much larger than the ion skin depth and Larmor radius of the field to allow for negligible Landau damping and to enable the system to evolve smoothly. The MHD equations will represent a single, electrically neutral and perfectly conducting fluid whose highly mobile electrons can rearrange quickly to keep the plasma neutral and cancel out any applied electric fields.

For the macroscopic description of the plasma, we will consider the five following variables: $\mathbf{J}$ the current density, $\mathbf{v}$ the bulk velocity, ρ the mass density of the fluid, P the fluid pressure, and $\mathbf{B}$ the magnetic field. With these variables, the ideal MHD principles can be summarised in five equations. (1) The continuity equation can be rearranged for a closed volume, V, over a surface, S, to describe the rate of change with time of the mass of the fluid, M_f, within the volume as

$$\frac{dM_f}{dt} = -\int_S \rho \mathbf{v} \cdot d\mathbf{S}. \tag{25}$$

Here $\rho\mathbf{v}$ has the dimensions of mass per unit time per unit area, or equivalently, momentum per unit volume. The continuity equation indicates the conservation of mass and electric charge. Using the convective time derivative, the continuity equation can be rewritten as $d\rho/dt = -\rho\nabla\cdot\mathbf{v}$. For an incompressible fluid, where ρ does not change, the equation simplifies to $\nabla\cdot\mathbf{v} = 0$. (2) The time evolution of the fluid velocity, $\mathbf{v}$, can be calculated by observing the rate of change of the velocity of a fluid element in response to an applied force. Since the fluid element contains a current density, $\mathbf{J}$, it will respond to a force, $\mathbf{J}\times\mathbf{B}/\rho$ per unit mass, in the presence of a magnetic field. Assuming a pressure force $-(1/\rho)\nabla P$ per unit mass, the time evolution of the fluid velocity is

$$\rho\frac{d\mathbf{v}}{dt} = \mathbf{J}\times\mathbf{B} - \nabla P. \tag{26}$$

(3) Since ρ and P are not independent, they can be related by the ideal gas equation of state $PV^{\gamma} = constant$, or

$$\frac{d}{dt}(P/\rho^{\gamma}) = 0 \tag{27}$$

where γ is the adiabatic index. This equation can be rearranged with the convective derivative to describe the evolution of P in terms of $\mathbf{v}$ and P only: $dP/dt = -\gamma P\nabla\cdot\mathbf{v}$. (4) Next, we seek the time evolution of $\mathbf{B}$. Using Ohm's law for a fluid element with conductivity σ, the current density is $\mathbf{J} = \sigma\mathbf{E}'$ where $\mathbf{E}'$ is the electric field experienced by a fluid element in its rest frame. The first order Lorentz transformation for $v^2 \ll c^2$ is $\mathbf{E}' = \mathbf{E} + \mathbf{v}\times\mathbf{B}$ which can be rewritten as $(1/\sigma)\mathbf{J} = \mathbf{E} + \mathbf{v}\times\mathbf{B}$. For an ideal fluid where conductivity is infinite, this relation can be reduced to $\mathbf{E} = -\mathbf{v}\times\mathbf{B}$. Taking the curl and substituting Faraday's induction law $-\frac{\partial\mathbf{B}}{\partial t} = \nabla\times\mathbf{E}$, the time evolution of the magnetic field can be given by

$$\frac{\partial\mathbf{B}}{\partial t} = \nabla\times(\mathbf{v}\times\mathbf{B}). \tag{28}$$

Even though $\mathbf{E}$ does not appear in this equation, the electric field plays an important role. The movement of the fluid relative to the magnetic field, generates an electric field.

Similarly, the curl of the electric field generates a magnetic field. This equation implies the concept of 'flux freezing', where the magnetic flux through a surface does not change as the surface moves and changes shape following the flow $\mathbf{v}(\mathbf{x}, t)$. (5) The last MHD equation that we seek describes the time evolution of the current density $\mathbf{J}$. Assuming $v^2 \ll c^2$ and $v_A \ll c$, where v_A is the Alfvén velocity, the spatial distribution of the magnetic field relative to its source is

$$\nabla \times \mathbf{B} = \mu_0 \mathbf{J}. \tag{29}$$

The Alfvén velocity is defined by a low-frequency travelling oscillation of ions in response to a magnetic field. The ion mass density provides inertia while the magnetic field tension acts as a restoring force. The resultant Alfvén velocity is defined as

$$v_A = \left(\frac{B^2}{\mu_0 n_i M}\right)^{1/2} = \left(\frac{\omega_{ci}}{\omega_{pi}}\right) c \tag{30}$$

$$= 6.9 \times 10^7 \left(\frac{B}{1\text{Tesla}}\right)\left(\frac{n_i}{10^{19}\text{m}^{-3}}\right)^{-1/2}\left(\frac{M}{m_p}\right)^{-1/2} \text{m s}^{-1} \tag{31}$$

where $\omega_{ci} = ZeB/M$ is the cyclotron frequency, $\omega_{pi} = (n_e Z e^2/\epsilon_o M)^{1/2}$ is the ion plasma frequency, and $n_i = n_e/Z$ is the ion number density for an electron number density, n_e, and charge state Z.

With these MHD equations, we can describe the forces that a magnetic field exerts on a fluid. A magnetic field in a conducting fluid with non-zero curl can set the fluid in motion,

$$\rho \frac{d\mathbf{v}}{dt} = -\nabla\left(P + \frac{B^2}{2\mu_0}\right) + \frac{1}{\mu_0}(\mathbf{B}\cdot\nabla)\mathbf{B}. \tag{32}$$

The equation can be further analysed to show that the force exerted by the magnetic field

is perpendicular to the field lines:

$$\rho\frac{d\mathbf{v}}{dt} = -\nabla P - \nabla_{\perp}\left(\frac{B^2}{2\mu_0}\right) + \frac{1}{R}\left(\frac{B^2}{\mu_0}\right)\hat{\mathbf{n}} \tag{33}$$

where $\hat{\mathbf{n}}$ is the vector normal to the magnetic field line and R is the radius of curvature. The second term on the right-hand side of the equation, $-\nabla_{\perp}(B^2/2\mu_0)$, is the magnetic pressure term that pushes the fluid away from regions of high magnetic field strength. In contrast, the third term, $(1/R)(B^2/\mu_0)\hat{\mathbf{n}}$, accelerates the fluid along $\hat{\mathbf{n}}$ towards the centre of curvature of the magnetic field line.

2.4 Generation of Seed Magnetic Fields

Since there is growing evidence that the universe is ubiquitously magnetised, the question becomes: What is the origin of these magnetic fields? To quote Professor Ellen G. Zweibel (**Nature** 1997), "The epoch when these fields originated, and the mechanism involved, are still uncertain. Both are aspects of what is arguably the most important issue in galactic magnetism: how the fields are generated and how they evolve." The MHD equation for the magnetic field evolution [21], including diffusion, does not include a term for magnetic field generation:

$$\frac{\partial\mathbf{B}}{\partial t} = \nabla\times\left(\mathbf{v}\times\mathbf{B}\right) + \eta\nabla^2\mathbf{B}. \tag{34}$$

Here the magnetic diffusivity coefficient is defined by $\eta = m_e v_c/n_e e^2$ where v_c is the collision frequency. Therefore, the third term in this equation characterises the time evolution of the magnetic diffusion while the second term represents the magnetic advection. For an initial magnetic field $B = 0$, it follows that $\partial\mathbf{B}/\partial t = 0$, so a fourth term for magnetic field generation is needed. There are a number of mechanisms that can generate magnetic fields such as Biermann battery, Weibel instabilities, resistive return currents, galactic outflows, relativistic self-generation, and primordial vorticity fluctuations.

2.4.1 Weibel Instability

Hydrodynamic instabilities can be driven in the interstellar and intergalactic medium by supersonic flows where shock waves behave like ordinary shocks on the macroscopic level but not at the microscopic level. In the case of supernova remnant SN 1006, Chandra x-ray observations have indicated densities of $n_i \sim 1$ cm^{-3} and temperatures of $T_i \sim 15$ keV, with a resultant Coulomb mean free path of ~ 13 pc. Since this Coulomb mean free path is of the order of the diameter of the remnant (~ 10 pc) and much larger than the shock thickness (~ 0.04 pc), it is evident that Coulomb collisions are not responsible for the observed shock width. Nonlocal, non-binary collisions of particles on the self-generated microscopic field fluctuations are responsible for scattering of the incoming un-shocked flow and cause irreversible dissipation and heating in the downstream plasma. These are believed to be long-range collective interactions between particles and electromagnetic fields which mediate the formation of 'collisionless' shocks. We now adopt cgs units used in literature.

In collisionless plasmas, where the mean free path for collision is larger than the Larmor radius, Weibel instabilities can generate magnetic fields for high Mach number, colliding ion-electron streams (M $>$ 43 for intergalactic medium flows). The counter-streaming beams generate electromagnetic perturbations that result in filamentation structures [25][26][27]. The resultant anisotropic bi-Maxwellian electron-ion distribution causes electromagnetic fields in the plasma to help restore momentum space isotropy, generating magnetic fields. More specifically, for counter-streaming ions, a non-zero perturbation of the magnetic field perpendicular to the flow causes particles moving in one direction to concentrate at one point while the ones moving in the other direction begin to diverge. This creates a current that reinforces the initial perturbation and the magnetic field can grow rapidly. Saturation of magnetic fields occurs when the growth rate is on the order of the electron cyclotron frequency $\gamma \sim \omega_p v_0/c \sim \omega_c$, implying $B \sim m\omega_c/e$. Furthermore,

when the magnetic field has saturated, it is near equipartition with the incoming ram pressure of the flow. Large magnetic fields can be generated by Weibel instabilities, but their scale is determined by the electromagnetic ion skin depth:

$$l_{\mathrm{EM}} \sim K\frac{c}{\omega_{pi}} \approx 3K \times 10^{-9}\left(\frac{n_{\mathrm{IGM}}}{10^{-4}\mathrm{cm}^{-3}}\right)^{-1/2} \mathrm{pc} \tag{35}$$

where ω_{pi} is the ion-plasma frequency and $K \sim 10 - 100$ is a numerical coefficient determined by particle-in-cell simulations. This leads to

$$B_{EM} \sim 10^{-8}\left(\frac{\eta_B}{10^{-3}}\right)^{1/2}\left(\frac{\nu_s}{10^{7}\mathrm{cm/s}}\right)\left(\frac{n_{\mathrm{IGM}}}{10^{-4}\mathrm{cm}^{-3}}\right)^{1/2} \mathrm{G} \tag{36}$$

where ν_s is the shock speed and η_B is an efficiency factor determined by numerical simulations. Since the electromagnetic ion skin depth is tiny on intergalactic scales, the magnetic field is only found in the shock transition layer and dissipates quickly in the absence of additional magnetic field generation mechanisms.

For the laser-produced plasma experiments in Chapters 4 and 5, magnetic fields produced by Weibel instabilities are not dominant. For our collisional conditions, the magnetic-field energy density is significantly larger than the ramp pressure of the incoming ionised plasma: $\epsilon_B^{\mathrm{ion}} = B^2/\mu_0 n_e^0 m_{\mathrm{ion}} v_{\mathrm{shock}}^2 > 0.1$ for $n_e^0 \approx 10^{14} cm^{-3}$ inferred electron density ahead of the shock. For the Weibel instability, the dominant contributors to the magnetic energy density are the protons with $\epsilon_B < \eta \sim 0.1$. Therefore, the kinetic Weibel instability does not play an important role in our experiments. Furthermore, a Weibel-generated field would be $\epsilon_B^{\mathrm{ion}} \approx m_e/m_{\mathrm{ion}} \approx 10^{-3}$ G compared to a measured magnetic field of $2 - 5$ G in the laser-produced shock experiments presented in this thesis.

2.4.2 Return Currents

It has been suggested that cosmic-ray protons generated by the first generation of galaxies, escaped into the intergalactic medium carrying an electric current [28][29], $\mathbf{j_c}$, that induces return currents, $\mathbf{j_t}$, and an associated electric field $\mathbf{E} = \eta \mathbf{j_t}$. The resistivity term [30], $\eta(T) = \eta_0 (T/k_B)^{-3/2}$, depends on the temperature of the intergalactic medium which is highly inhomogeneous due to adiabatic contraction and shocks produced by structure formation. Therefore, the curl of the electric field generates a magnetic field:

$$-\frac{\partial \mathbf{B}}{\partial t} = \nabla \times \mathbf{E} = \nabla \times \eta \mathbf{j_t} \tag{37}$$

For the laser intensities in our experiments, $I = 2 \times 10^{14}$ W cm^{-2}, the hot electrons are distributed with temperature $T_{\text{hot}} \approx 5$ keV. With a Bdot probe induction coil placed 3 cm from the target, the hot electrons would reach the coil on the nanosecond timescale. The magnetic field time history measured by the Bdot probe induction coils, indicate a peak field around $\sim \mu$s, which implies that return currents do not contribute to the magnetic field generation observed in our experiments.

2.4.3 Biermann Battery Mechanism

Asymmetrical shock waves are believed to seed magnetic fields due to misaligned density and temperature gradients that drive currents via the Biermann battery process [31]. The Biermann battery mechanism as a source of magnetic fields in the IGM was first proposed in the context of ionisation fronts produced during the epoch of cosmic reionisation [32][33][34]. Observations of quasar (QSO) spectra indicate the early universe was almost completely ionised below redshifts of $z \sim 5$, and the baryonic matter is believed to then recombine into a more neutral form at $z \leq 1300$ as the universe began to cool below 4000 K. During this recombination, sources of ionising radiation began to ionise the IGM, cre-

ating regions where magnetic fields can be thermally generated. E. R. Harrison suggests the magnetic fields generated in proto-galaxies during this period are weak compared to the present-day intensity of galactic magnetic fields, and therefore must be amplified as compact objects such as galaxies form and evolve.

In terms of the seed mechanism, K. Subramaniam *et al.* describe that pressure gradients exist at ionisation fronts where the temperature can vary by $\sim 10^4$ K and the gas changes from being almost ionised to completely neutral. Both electrons and protons feel a pressure force but the lighter electrons experience a larger acceleration. The collisions between electrons and protons provide a frictional force that tries to maintain a quasi-steady-state, resulting in an electric field that couples back positive and negative charges. In the case of a fluid with misaligned density and temperature gradients, an electric field with a non-vanishing curl arises. By Faraday's law of induction, this can seed a magnetic field. Furthermore, misaligned density and temperature gradients are prevalent in the universe. At ionisation fronts, the temperature gradients tend to be normal to the front and point away from the source of ionising photons. However, density fluctuations in the IGM can collapse to form compact structures such as galaxies and clusters with very little relation to the ionisation fronts sweeping across these objects. Therefore, this leads to a curl of the electric field, and through induction, to the seeding of the universe with magnetic fields by the 'Biermann battery mechanism'. Simulations conducted by N. K. Gnedin *et al.* also suggest magnetic field generation occurred during the epoch of reionisation of the universe at cosmological ionisation fronts emanating from stars in proto-galaxies. Magnetogenesis can continue as ionisation fronts propagate through high-density neutral filaments, and these simulations indicate seed fields of $B_0 \approx 10^{-19}$ G [34].

Experimental observations of the Biermann battery mechanism date back to the late 1960's when a team of researchers at the P. N. Lebedev Physics Institute made measurements of magnetogenesis from a spark produced by focusing a laser in a gas [35]. Using a q-switched ruby laser that delivered 2 J in a pulse duration of 30 nsec, a focused beam

generated a spark that seeded magnetic fields diagnosed with a 10 mm diameter induction coil. The team observed a magnetic moment generated by the laser interaction which encouraged other groups such as G. A. Askar'yan *et al.* to conduct similar experiments on solid targets [36].

In particular, a detailed examination of spontaneous magnetic fields of the order of kilogauss, generated in laser-produced plasmas, was conducted by J. A. Stamper *et al.* at the U. S. Naval Research Laboratory on solid targets [37]. In this experiment, a 250 μm Lucite fiber was ablated by 60 J of a neodymium-doped glass laser in a 30 nsec pulse within a background gas of 200 mTorr nitrogen. Using 1 mm diameter induction probes, the team characterised the magnetic field profile from the front surface of the solid target with a maximum field of $\sim$ 450 kG closest to the target. They noticed a few distinguishing traits: (1) the generated field traveled at the velocity of the shock wave $(1-5)\times10^7$ cm/s, and (2) the fields were in a primarily azimuthal direction at distances $>$ 1 cm from the target. One source of magnetic flux proposed in this experiment was the pressure gradient, assuming $\nabla n \times \nabla T \neq 0$. This is considered the 'battery' which drives currents and subsequent magnetic fields. However, theory predicts much larger, megagauss, fields to exist closer to the target at the focal region [38][39].

A few years later, the same group of researchers, used non-invasive methods to measure these MG fields generated by the Biermann battery mechanism [40]. Specifically, two Faraday rotation diagnostics were used to characterise the generated fields. (1) The first method used second harmonic (0.53 μm) light at the surface of the target and measured a 0.2 rad rotation angle, corresponding to a 4.8 MG Biermann battery field. (2) The second method used reflected laser light of the first harmonic (1.06 μm) at the critical region and measured a $\pi/8$ rotation, corresponding to a 1.6 MG field. These two methods were in agreement within a factor of 3 to 4 and also confirmed numerical studies and models [38][39]. Since the 1970's, a range of experiments involving the investigation of generated magnetic fields continued [41][42][43][44]. By the second millennium, the field

of laboratory astrophysics came to prominence and magnetic fields were (and continue to be) an important topic in terms of the magnetogenesis of our universe. Further discussion of this topic can be found in Section 4.2.

In laser-plasma experiments there are many sources of shock asymmetry. For instance, an asymmetrical laser drive or inhomogeneities in the ambient medium can generate asymmetrical shock waves. The generation of Biermann battery fields can be better understood by starting with the fluid equation of motion in a plasma, neglecting viscosity for now:

$$\rho\frac{d\mathbf{v}}{dt} = -n_e e\Big(\mathbf{E} + \mathbf{v}\times\mathbf{B}\Big) - \nabla P_e. \tag{38}$$

The inertia term $d\mathbf{v}/dt$ can be neglected since its contribution is only appreciable on longer time scales. From Maxwell's equations, recall Faraday's law of induction and substitute it into Equation 38:

$$\frac{\partial\mathbf{B}}{\partial t} = \nabla\times\Big(\mathbf{v}\times\mathbf{B}\Big) - \nabla\times\Big(\frac{1}{n_e e}\nabla P_e\Big), \tag{39}$$

where the pressure is defined as $P = nk_BT$. The final equation of the induced magnetic field, with the addition of a viscous term, is

$$\frac{\partial\mathbf{B}}{\partial t} = \nabla\times(\mathbf{v}\times\mathbf{B}) - \frac{k_B}{e}\frac{\nabla n_e\times\nabla T_e}{n_e} + \eta\nabla^2\mathbf{B}. \tag{40}$$

The second term is only nonzero when there is an initial magnetic field in the system, and the fourth term for magnetic diffusion is negligible for plasmas with large Magnetic Reynolds numbers, Rm. It is now apparent that a seed magnetic field can be generated by misaligned density and temperature gradients, known as the Biermann battery process:

$$\frac{\partial\mathbf{B}}{\partial t} = -\Big(\frac{k_B}{n_e e}\Big)\nabla n_e\times\nabla T_e. \tag{41}$$

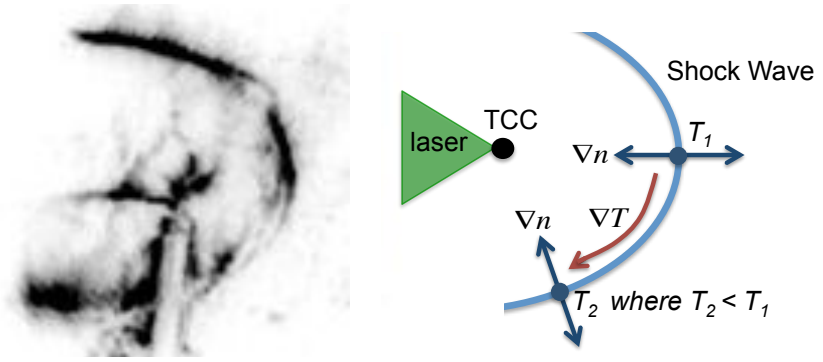

Figure 9: **Generation of magnetic fields via the Biermann battery mechanism.** Misaligned density and temperature gradients generate vortices that can induce seed magnetic fields. Biermann battery at the shock is dominant in asymmetrical shock waves that are typically generated in laser plasma experiments (left). Note that a perfectly spherical shock wave would not generate Biermann battery seed fields at the shock.

Furthermore, there is an important equivalence between the magnetic field and vorticity [45]. For vorticity $\omega = \nabla \times \mathbf{v}$, the equation of motion can be expressed as

$$\frac{\partial \omega}{\partial t} = \nabla \times (\mathbf{v} \times \omega) + \nu \nabla^2 \omega - \frac{\nabla P \times \nabla \rho}{\rho^2} \tag{42}$$

where the kinematic viscosity (momentum diffusivity) is $\nu = \mu/\rho$ the ratio of the dynamic viscosity μ to the fluid density. Therefore, the Biermann battery magnetic field generation in terms of vorticity, can be estimated as

$$B_{\text{vort}} = \frac{m_{\text{ion}}}{e}\omega \approx \left(\frac{(\xi-1)^2}{\xi}\right)\left(\frac{m_{\text{ion}}}{e}\right)\left|\frac{\partial \mathbf{v}_{\text{shock}}}{\partial S}\right| \tag{43}$$

where $\xi \approx 3-4$ is the shock compression ratio for a strong shock and $\partial \mathbf{v}_{\text{shock}}/\partial S \sim \kappa v/r$ is the tangential gradient of the shock velocity. For a shock velocity $v_{\text{shock}} = 5$ km/s, shock asymmetry coefficient $\kappa = 0.1$ based on density gradients measurements (Schlieren), and shock position $r = 3$ cm, the magnetic field would be $B \sim 10$ G. It should be further noted that the dominant Biermann battery generated fields measured in Chapter 4 originate

from the shock front– not the laser spot. It is possible to generate strong fields near the target that can be frozen into the plasma. However, shots with and without an ambient gas, indicate that this contribution is small. If Biermann battery at the laser spot was the dominant mechanism, then the measured field should not change in the absence of an ambient gas (and therefore absence of a shock wave). It follows that vorticity drives magnetic field generation at the shock.

2.5 Development of Turbulence

According to Richard Feynman, turbulence is "the most important unsolved problem of classical physics," and yet it is so common that we observe it in our every day lives. In fact Werner Heisenberg said, "When I meet God, I am going to ask him two questions: Why relativity? And why turbulence? I really believe he will have an answer for the first." A general definition of turbulence is the presence of structures having a range of spatial scales that are smaller than the spatial scales of the motions that provide the energy source producing the structure. Turbulent flows are dominated by rotating motions called vortices which produce small-scale fluctuations and the recognisable chaotic swirling patterns seen in the environment. Large eddies form during the turbulent driving process transferring kinetic energy into the potential energy of the system, generating smaller and smaller vortices that lose their energy by viscous dissipation.

A more rigorous set of definitions proposed by Andrey Kolmogorov in 1941, include [46]:

Definition 1 The turbulence is called locally homogeneous if the system has evolved to a state that is independent of the initial conditions.

Definition 2 The turbulence is called locally isotropic if the system is homogenous and invariant with respect to rotations and reflections. It follows that $\overline{v(x,y,z)} = 0$.

For low Reynolds numbers, $\mathrm{Re} = vL/\nu$ where ν is the viscosity, the flow remains dominated by large-scale structures and boundary conditions. The Reynolds number is a dimensionless ratio of the inertial forces of a fluid to the viscous forces. Typically, turbulent flows have large $\mathrm{Re} \sim 10^4$ where the system develops fine-scale structures with homogeneous distribution. In Chapters 4 and 5, we generate plasmas with $\mathrm{Re} \sim 10^6$ and quantify the level of turbulence by examining the energy power spectrum and cascade of vortices.

There are three scalelengths to describe vortices generated in a turbulent flow: Integral length scales, Taylor microscales, and Kolmogorov length scales [12]. (1) Integral length scales account for the largest vortices with the lowest frequencies. They obtain their energy from the mean fluid flow, carry most of the energy, and are highly anisotropic. The maximum length of an integral scale eddy is the characteristic size of the system. As turbulence begins to form in a fluid, boundary conditions can not be ignored and therefore sharp edges can occur in the resultant eddies. As the eddies evolve, viscous diffusion smoothes the edge of the shear layer to produce a laminar boundary layer of scale length $\sqrt{\nu t}$. On the timescale of the large eddies, l/ω_e, the boundary layer scale length can be rewritten in terms of Re as $\lambda_i = l/\sqrt{\mathrm{Re}}$. These large vortices transfer their energy to smaller and smaller vortices until they become invariant to global processes– where the vortex size is less than the Taylor microscales.

(2) The Taylor microscale is most commonly associated with the onset of turbulent flow and is the intermediate step between the large integral length scale vortices and smallest Kolmogorov scale vortices [48]. During this stage, large eddies pass down their energy to smaller eddies without dissipation, on a length scale given by $\lambda_T/l = \sqrt{15}\mathrm{Re}^{-1/2}$. As Re increases, the difference between the Taylor microscale and Kolmogorov length scale becomes increasingly large, and the flow of energy from larger to smaller scales is governed by the vorticity dynamics. Kolmogorov determined a simple scaling of vortices from the Taylor microscale down to the Kolmogorov scale, by showing the wavenumber spectrum of

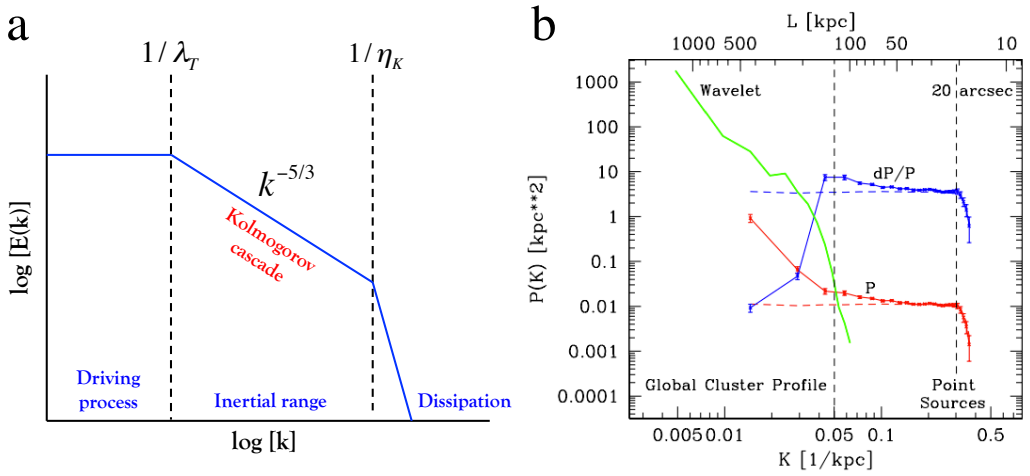

Figure 10: **Development of Kolmogorov turbulence. a,** Schematic of the turbulent kinetic energy spectrum. At smaller frequencies, turbulence is governed by the driving processes. The structure drawn can vary depending on the driving conditions. Large vortices transfer energy to smaller vortices until global processes no longer influence the turbulent structures at $k > 1/\lambda_T$, where vortices cascade down to smaller diameters by the Kolmogorov relation $k^{-5/3}$. At $k > 1/\eta_K$, dissipation dominates. **b,** The power spectrum of the Coma cluster shows the similar transitions (Image: Schuecker 2014). The blue continuous line is the normalised pressure distribution (dP/P), the red continuous line is the raw spectrum of the cluster profile (P), and the vertical dashed lines are the characteristic scales [47].

the kinetic energy, $E(k)$, is proportional to $k^{-5/3}$, the 'Kolmogorov cascade':

$$E(k) = C_K \epsilon^{2/3} k^{-5/3} \tag{44}$$

where C_K is the Kolmogorov constant, ϵ is the rate of kinetic energy transport from large to small scales, and the exponent 5/3 is not a universal constant and can be 6/3 for Mach numbers greater than one (Oboukhov 1941). This cascade region of the energy spectrum can also be referred to as the 'inertial range' where inertial effects are much larger than viscous effects, implying viscosity does not play a large role in the internal dynamics as the eddies decrease in diameter. This inertial range appears when Re is large enough that

$50\eta_K < \lambda_T$ for the Kolmogorov scale length η_K, implying Re $\sim 10^4$.

During the cascade process, the vortices become smaller in diameter with higher frequency until (3) they reach the Kolmogorov scale length, the smallest scales in turbulent flow, where viscosity dominates and the kinetic energy is dissipated into heat [48]. The length scale η_K, time scale τ_K, and velocity scale v_K, can be written in terms of the Reynolds number:

$$\eta_K = \frac{l}{\mathrm{Re}^{3/4}}; \quad \tau_K = \frac{l}{\omega_e \ \mathrm{Re}^{1/2}}; \quad \text{and} \quad v_K = \frac{\omega_e}{\mathrm{Re}^{1/4}}. \tag{45}$$

Using our defined rotational velocity, ω, and vortex diameter, λ, this implies the rotational time scale is λ/ω while the viscous damping time scale is λ^2/ν. When the vortices reach the Kolmogorov scale length, they are damped by viscosity in the order of one rotation. Setting the rotation time scale equal to the damping time scale, the smallest vortex is $\omega\lambda/\nu \sim 1$. Rewritten with the Kolmogorov variables, $\eta_K v_K/\nu = 1$ which is satisfied by Equation 45.

In summary, turbulence develops over three stages: (1) The Integral scale length, where vortices are influenced by global processes and begin to transfer energy from the largest eddies $\lambda = L$, to smaller vortices. (2) The inertial range that begins when the vortex diameter is less than the Taylor microscale, λ_T. The eddies undergo a Kolmogorov cascade down to smaller vortex diameters. (3) The smallest eddies, with vortex diameter η_K, where dissipation of kinetic energy occurs. The final consideration is to address the fluid dynamics of a turbulent system. Taking the curl of the fluid equation, the vorticity dynamics can be described by

$$\frac{\partial \omega}{\partial t} = \nabla \times (\mathbf{v} \times \omega) + \nu \nabla^2 \omega, \tag{46}$$

which is identical to Equation 42 without the magnetic field generation term. This indicates that the vorticity will diffuse in the absence of a net flow. The second term indicates

that, similar to frozen-in magnetic fields, the vorticity can become 'frozen' into the fluid flow. Furthermore, the final term in this equation indicates that the kinematic viscosity contributes to diffusion and transfers momentum, or vorticity, from the structure being damped into the surrounding fluid.

2.5.1 Magnetic Field Amplification by the Turbulent Dynamo Mechanism

The dynamo effect is the amplification of magnetic fields by fluid motions. There are two types of dynamo: 'mean-field dynamo', where the magnetic fields grow at scales larger than the scales of the fluid motion, and 'fluctuation dynamo', where the magnetic-fluctuation energy grows at or below the outer scale of the fluid motions. The magnetic Prandtl number, Pm, plays an important role in assessing dynamos, because it determines the relative size of viscous and resistive scales in the system. Defined by $\mathrm{Pm} = \mathrm{Rm}/\mathrm{Re} = \nu/\eta$, the Prandtl number is the ratio of viscosity to magnetic diffusivity where the magnetic Reynolds number is $\mathrm{Rm} = vL/\eta$. The magnetic resistivity [30], η, is

$$\eta(\mathrm{cm}^2/\mathrm{s}) = 2.4 \times 10^5 \frac{\ln\Lambda}{T_e^{3/2}}. \tag{47}$$

When $\mathrm{Rm} \ll 1$, the magnetic fields become diffusive and are no longer confined to the flow but rather the boundary conditions of the system. However, when $\mathrm{Rm} \gg 1$ the magnetic 'bulk motion' dominates and the flux lines are advected with the fluid flow. When $\mathrm{Pm} \gg 1$, the ratio of the resistive scale, l_η, to viscous scale, l_ν, is $l_\eta/l_\nu \sim \mathrm{Pm}^{-1/2} \ll 1$, and the resistive scale lies within the viscous range, outside the inertial range, where the velocity field is laminar. Even for $\mathrm{Pm} \sim 1$, turbulent dynamo can be operating because the bulk of the magnetic energy resides below the viscous scale. Physically, for $\mathrm{Pm} \geq 1$, the fluid motions are stretching, twisting, and folding the magnetic fields lines to amplify magnetic energy to equipartition.

Mean-field dynamo is most commonly associated with liquid-metal cores of planets and therefore a magnetic Prandtl number Pm $\ll 1$. Whereas, fluctuation dynamo occurs in the interstellar medium and intracluster medium of galaxy clusters, where Pm $\gg 1$ [11]. Our ultimate goal is to better understand the latter, small-scale dynamo which is likely responsible for the ubiquitous presence of dynamically strong magnetic fields in the universe– further referred to as 'turbulent dynamo'. For instance, the supernova remnant Cassiopeia A, presented in Chapter 4, has Pm = 94. The laboratory experiments presented in this thesis were limited due to laser capabilities and reached Pm $\sim 10^{-4}$. However, current experimental preparations using the NIF laser indicate that plasma conditions should reach Pm > 1.

Determining the presence of dynamo analytically is nearly impossible and we rely heavily on numerical simulations to indicate the onset of turbulent dynamo. However, the magnetic-energy spectrum can indicate the presence of dynamo and simulations have indicated that a $k^{+3/2}$ spectrum, otherwise known as the Kazantsev or Kulsrud and Anderson spectrum, is typical for Pm $\gg 1$. For Pm above and just above unity, the spectrum slope is positive and peaks at the resistive scale. The slope of the magnetic-energy spectrum depends on Pm but not Re or Rm individually. For low Pm, the slope becomes negative and the peak of the spectrum shifts towards the outer scale of the system. When $l_\eta \gg l_\nu$, the magnetic fluctuations are heavily dissipated below the resistive scale and cannot feel the spatially smooth viscous-scale motions. The magnetic cutoff lies within the inertial range, far from both the viscous and outer scales, where $l_\eta/l_\nu \sim \mathrm{Pm}^{-3/4} \gg 1$.

2.5.2 Turbulent Induction of Magnetic Fields for low Pm

In the presence of a large-scale magnetic field, the fluid motions can tangle fields lines to generate small-scale magnetic fluctuations, an effect known as 'magnetic induction'. Turbulent magnetic induction is a nonlocal energy-transfer process in which the uniform

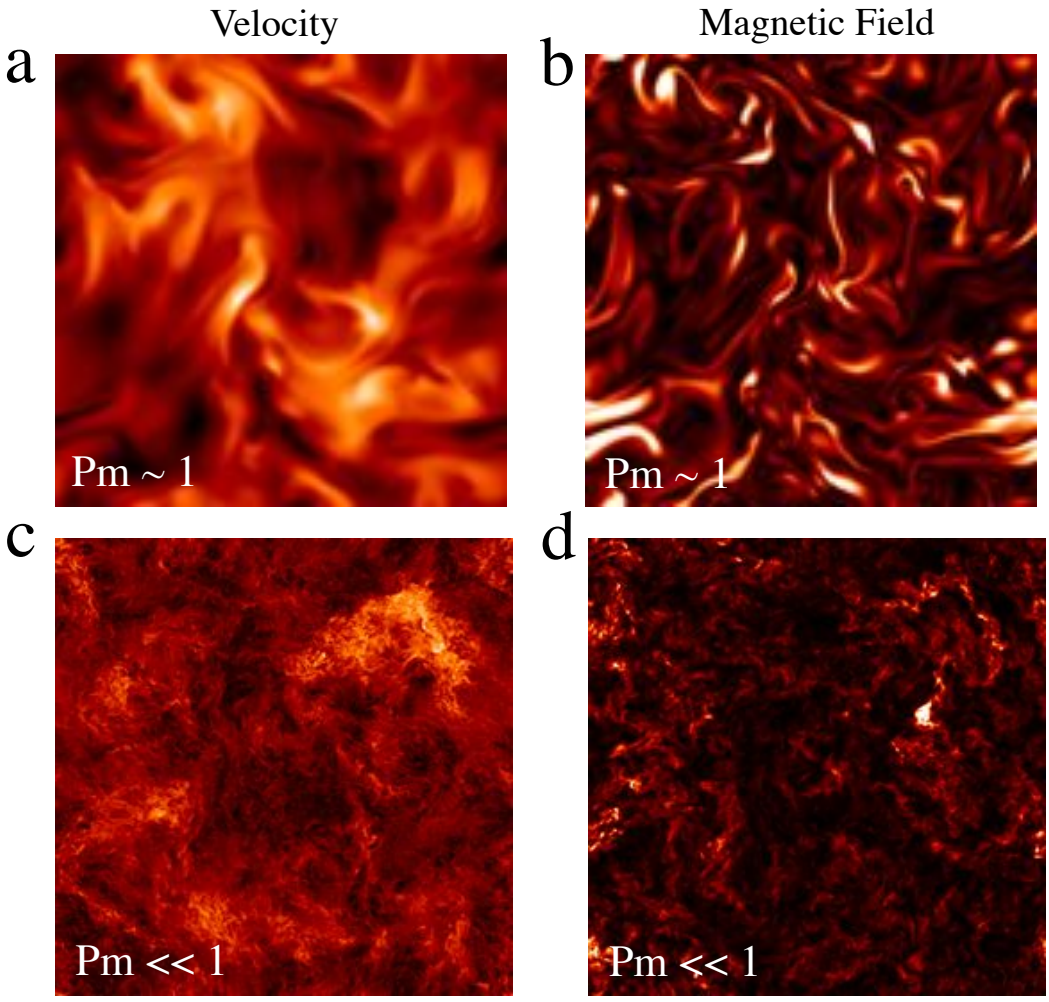

Figure 11: **Simulations of turbulent dynamo. a,** Cross-section of the absolute value of the velocity and **b,** the growing magnetic field for Pm $\sim$ 1, where Rm = Re $\equiv$ 440. **c,** Velocity and **d,** growing magnetic field for Pm $\ll$ 1, where Rm $\equiv$ 430 and Re $\equiv$ 6200 (Schekochihin 2007).

mean magnetic field, generated or maintained by some mechanism, couples to small-scale motions resulting in magnetic fluctuations. This means in the absence of dynamo, for Pm $\ll$ 1 but Rm $>$ 1, magnetic fields can become frozen into the fluid motions, resulting in amplification [11]. The extent of the turbulent magnetic field amplification depends

on the Rm attained from the plasma conditions. If we consider the magnetic field to be represented as the sum of a uniform mean field and a fluctuating field, $\mathbf{B} = \mathbf{B_0} + \delta\mathbf{B}$, the induction equation can be written as

$$\frac{\partial \delta \mathbf{B}}{\partial t} + \mathbf{v} \cdot \nabla \delta \mathbf{B} = \delta \mathbf{B} \cdot \nabla \mathbf{v} + \eta \nabla^2 \delta \mathbf{B} + \mathbf{B_0} \cdot \nabla \mathbf{v}. \tag{48}$$

For dynamically weak mean fields, the absence of dynamo will give rise to a saturated level of magnetic-fluctuation energy, proportional to the mean-field energy,

$$\langle |\delta \mathbf{B}|^2 \rangle = f(\mathrm{Rm}) {\mathbf{B_0}}^2 \tag{49}$$

where $f(\mathrm{Rm})$ is a coefficient that can be determined for the cases of low Rm and high Rm.

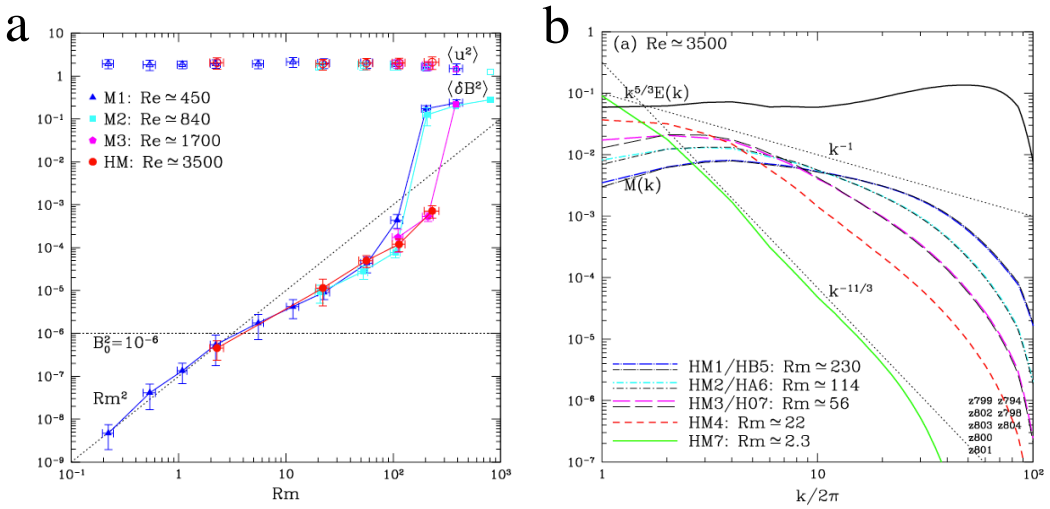

Figure 12: **Turbulent induction of magnetic fields. a,** The mean square induced magnetic field $\langle |\delta \mathbf{B}|^2 \rangle$ versus Rm for a small, uniform magnetic field $B_0 = 10^{-3}$ generated by some mechanism. Turbulent induction begins at Rm ~ 2 and continues amplifying the magnetic fields until turbulent dynamo sets in at Rm ~ 200. **b,** The normalised magnetic energy spectra indicate the onset of turbulent induction at $k^{-11/3}$, known as the Golitsyn spectrum [49]. As Rm increases, the magnetic energy spectrum becomes less negative [11].

For small values of Rm, the diffusion term in Equation 48 dominates the nonlinear terms, indicating that the magnetic field saturation is governed by the 'quasistatic' balance: $\eta\nabla^2\delta\mathbf{B} = -\mathbf{B_0}\cdot\nabla\mathbf{v}$. This means that $\langle|\delta\mathbf{B}|^2\rangle \sim Rm^2B_0^2$, so the level of magnetic field amplification is directly related to the Rm attained in the plasma. The quasistatic approximation can be rewritten in terms of the magnetic energy and kinetic energy in wavenumber space:

$$\eta k^2\delta\mathbf{B_k} = \mathbf{i}(\mathbf{k}\cdot\mathbf{B_0})\mathbf{v_k} \quad \rightarrow \quad M(k) = \frac{B_0^2E(k)}{3\eta^2k^2}. \tag{50}$$

For a turbulent plasma with a Kolmogorov kinetic energy spectrum (Equation 44), the magnetic energy spectrum at low Rm is known as the Golitsyn spectrum [49]:

$$M(k) \sim B_0^2\eta^{-2}\epsilon^{2/3}k^{-11/3}. \tag{51}$$

Numerical simulations indicate that at Rm ~ 2, the mean square $\langle|\delta\mathbf{B}|^2\rangle$ becomes larger than B_0^2, and moderate magnetic field amplification begins to occur. The purpose of this thesis is to present the first measurements of nonlinear amplification of magnetic fields by turbulent induction in a laboratory plasma, a precursor to turbulent dynamo. Figure 12 shows a horizontal cutoff at Rm ~ 2 where nonlinear magnetic field amplification begins to develop until turbulent dynamo is reached at Rm ~ 200.

Even in the presence of dynamo, large magnetic fields can continue to develop small-scale structures by the turbulent induction process; however, distinguishing between contributions from induction and dynamo can be difficult. As the Rm increases, the slope of the magnetic energy spectrum decreases within the inertial range that lies above the resistive scale, $L \gg l \gg l_\eta$. The diffusive term can be ignored and the magnetic field source term B_0 can be set equal to the nonlinear terms. When $\delta B \sim B_0$, the magnetic energy in wavenumber space is $M(k) \sim B_0^2k^{-1}$. Therefore, magnetic field amplification by the turbulent induction process occurs when the slope of the magnetic energy spectrum lies

within the range of $k^{-11/3}$ to k^{-1}. As the slope flattens and becomes positive, the turbulent dynamo process supersedes this effect and begins to dominate. Experimental results of turbulent induction of magnetic fields for $\mathrm{Pm} \ll 1$ and $\mathrm{Rm} \sim 2 - 14$ in a laser-produced plasma will be presented in Chapters 4 and 5. These results laid the groundwork for current experiments in Chapter 6 being conducted by the author at the National Ignition Facility to measure turbulent dynamo for $\mathrm{Pm} \sim 3$ and $\mathrm{Rm} \sim 9,000$.

2.6 Scaling of Laboratory Plasmas to Astrophysical Phenomena

Utilising the scale invariance of MHD equations, scaled astrophysical environments can be created in the laboratory [9]. Plasmas that are centimetres in diameter and develop over a few microseconds, can be scaled to objects such as supernovas that are light years in diameter and develop over centuries. If these two systems (laboratory plasmas and astrophysical objects) behave as ideal compressible hydrodynamic fluids, then the Euler equations for a polytropic gas remain invariant under a set of transformation rules. There are four conditions for an ideal hydrodynamic fluid that must be satisfied to make this transformation: (1) the system must be collisional; (2) convective transport needs to dominate conduction; (3) radiation energy flux needs to be negligible; and, (4) viscosity must be negligible.

2.6.1 Hydrodynamic Similarity Conditions

We will discuss the case of an ideal compressible hydrodynamic fluid, a polytropic gas in which the energy density per unit volume, ϵ, is proportional to the pressure, P. The following scaling equations are not true for all ideal gases. For instance, if higher degrees of freedom are excited in a gas at higher temperatures, then a laboratory scaling would not apply. However, the similarity conditions will hold for a fully ionised gas and for a gas

that is dominated by radiative pressure. The Euler equations (Equations 15 - 17) used to describe the behaviour of shock waves, remain invariant under the following transformations between two systems [9] denoted by 1 and 2:

$$L_2 = aL_1; \quad \rho_2 = b\rho_1; \quad P_2 = cP_1; \quad t_2 = a\left(\frac{b}{c}\right)^{1/2} t_1; \quad \mathbf{v_2} = \left(\frac{c}{b}\right)^{1/2} \mathbf{v_1} \tag{52}$$

with arbitrary positive numbers a, b, and c. Therefore, the hydrodynamic processes in both systems will be identical if the dimensionless 'Euler Number',

$$\mathrm{Eu} = v_1\left(\frac{\rho_1}{P_1}\right)^{1/2} = v_2\left(\frac{\rho_2}{P_2}\right)^{1/2}, \tag{53}$$

is equal in both systems. There is also a relation between the timescales of the two systems given by

$$t_1 = t_2\left(\frac{L_1}{L_2}\right)\left(\frac{\rho_1}{\rho_2}\right)^{1/2}\left(\frac{P_2}{P_1}\right)^{1/2}. \tag{54}$$

2.6.2 Scaling Assumptions

To use these scaling equations, the system must fulfil four major requirements of Euler's hydrodynamic equations [9]: (1) The system must be collisional. This means the system must demonstrate fluid-like behaviour by keeping the particles localised on spatial scales smaller than L, the scale of the system. Localisation of particles occurs when either the ion Larmor radius, $r_{L\mathrm{ion}}$, or the collisional mean free path, l_c, are much less than L:

$$\frac{r_{L\mathrm{ion}}}{L} \approx 10^{-4}\left(\frac{v_d(\mathrm{cms}^{-1})}{B(\mathrm{G})L(\mathrm{cm})}\right) \ll 1 \tag{55}$$

or

$$\frac{l_c}{L} \cong 3 \times 10^{13}\left(\frac{T(\mathrm{eV})^2}{\ln\Lambda n_i L}\right) \ll 1 \tag{56}$$

where v_d is the driving velocity and n_i represents the ion density.

(2) Convective heat transport needs to dominate conduction. This means the system must transport heat due to the bulk motion of the particles rather than collisions of diffusive particles during a random walk. We require the Peclet number, as defined below, to be large in both the laboratory and astrophysical systems,

$$\mathrm{Pe} = \frac{vL}{\chi} \gg 1, \tag{57}$$

where χ is the thermal diffusivity. The thermal diffusivity is the ratio of the thermal conductivity to the volumetric heat capacity and represents the ability of a material to conduct thermal energy relative to its ability to store thermal energy. For our purposes, the thermal diffusivity can be simplified to the following relations:

$$\chi(\mathrm{cm}^2/\mathrm{s}) = \begin{cases} 1.0 \times 10^{21} \frac{T_e^{5/2}}{n \ln\Lambda}, & \text{in the laboratory} \\ 8.6 \times 10^{9} \frac{T_e}{B}, & \text{in a SNR} \end{cases} \tag{58}$$

Therefore, the Peclet number is better understood as the ratio of the rate of advection to the rate of thermal diffusion. Note that χ here can either represent unmagnetised or magnetised electrons. We have also assumed that the plasma is singly ionised in both environments, and consists of just protons and electrons in, for example, a supernova remnant (SNR).

(3) Energy fluxes due to radiation must be small compared to energy fluxes from hydrodynamic processes. For an optically thin plasma, photons have a longer mean free path than the plasma length, so radiative cooling is dominated by bremsstrahlung, radiation produced from the deceleration of charged particles. This means the cooling time, τ_{rad}, associated with radiation must be much larger than the characteristic hydrodynamical

time,

$$\mathrm{R}_c = \frac{\tau_{rad}}{t} \gg 1, \tag{59}$$

where

$$\tau_{rad}(\mathrm{s}) = 2.4 \times 10^{13} \frac{T_e^{1/2}}{n}. \tag{60}$$

Shock waves observed in the universe tend to be optically thin, otherwise radiation would not be emitted or detected for scientific study. Similarly, laser-produced shock waves in the experiments presented are optically thin, meaning that photons can travel through the material with few interactions where $\lambda_{Brem} > L$.

(4) Viscosity needs to be negligible, requiring a Reynolds number, Re, much larger than unity. Viscosity is a measure of a fluid's resistance to deformation by shear or tensile stress and can be thought of as the number of collisions between neighbouring particles. A viscous fluid like honey would have less collisions than a fluid such as acetone. For our purposes, the viscosity [50] can be simplified to:

$$\nu(\mathrm{cm}^2/\mathrm{s}) = \begin{cases} 2.0 \times 10^{19} \frac{T_i^{5/2}}{nA^{1/2}\ln\Lambda}, & \text{in the laboratory} \\ 7.8 \times 10^{-5} \frac{n^2 \ln\Lambda}{B^2 T_i^{1/2}}, & \text{in SNR} \end{cases} \tag{61}$$

where A is the atomic weight of the laboratory ions ($A \approx 40$ in our case). When $\mathrm{Re} \ll 1$, viscous forces dominate and the fluid motion is more smooth and continuous. This means that when the Reynolds number is high, inertial forces dominate and the flow is more turbulent, resulting in vorticies and other instabilities.

Our scaling relations are also applicable in presence of magnetic fields if those remain dynamically unimportant in the hydrodynamic evolution of the system. Equivalently, we require that the ratio, β, between the hydrodynamical pressure and the magnetic pressure, $B^2/2\mu_0$, be large in both the laboratory and astrophysical environment.

2.7 Laser-Matter Interactions

At irradiances of 10^{12} to 10^{16} W/cm^2, laser light incident upon a target immediately produces a plasma at the surface. As laser light penetrates the plasma, it undergoes three processes: (1) refraction, (2) reflection, and (3) absorption [12]. For lasers relevant to the work presented in this thesis (nanosecond pulses of visible light) the frequency of the laser is large enough that the ion motion is negligible on the timescale of the laser propagation. Furthermore, due to their lighter mass, the laser energy is primarily deposited by heating the electrons, which then transfer energy to the ions either through collisions or through charge-separation acceleration. The density scalelength of the plasma can be approximated [51] as $L \approx c_s \Delta t_L$ where Δt_L is the laser pulse duration and the sound speed, c_s, is defined in Section 1.1. Long scalelength plasmas occur at $L \gg \lambda$. For the experiments presented in this thesis, we employed a green $\lambda = 527$ nm, 1 ns laser pulse (with I $\sim 10^{14}$ W/cm^2) and generated a plasma with $c_s \sim 2.2 \times 10^5$ cm/s, implying that $L \sim 2200$ nm.

For a Maxwellian distribution of particles, the rate of collision between electrons and ions is

$$\upsilon_{ei} = \frac{1}{3(2\pi)^{3/2}} \frac{Z\omega_{pe}^4}{n_e v_e^3} \ln\Lambda = 3 \times 10^{-6} \ln\Lambda \frac{n_e Z}{T_e^{3/2}} [s^{-1}] \tag{62}$$

where $v_e = \sqrt{T_e/m_e}$ for T_e in eV, and the electron plasma frequency is $\omega_{pe} = \sqrt{4\pi e^2 n_e/m_e} = 5.64 \times 10^4 \sqrt{n_e}$ rad/s for n_e in cm^{-3}. Therefore, the propagation of electromagnetic waves in a plasma can be described by the dispersion relation [12],

$$\omega_0^2 - \frac{\omega_{pe}^2}{1 + (\upsilon_{ei}/\omega_0)^2} - c^2k^2 + i\frac{\upsilon_{ei}/\omega_0}{1 + (\upsilon_{ei}/\omega_0)^2}\omega_{pe}^2 = 0 \tag{63}$$

in which k is the wavenumber of the laser light. The imaginary component causes damping of the wave while the real component describes the propagation of the wave. When k approaches zero at approximately $\omega_0 = \omega_{pe}$, the wave can no longer propagate and is either

reflected or absorbed. Physically, the electrons are resonantly oscillating at the frequency of the laser light, creating a mirror surface, or 'critical surface', to reflect light. The critical surface, in terms of the laser wavelength (in microns), is $n_{crit}(cm^{-3}) = 1.1 \times 10^{21}/\lambda_{\mu m}^2$.

2.7.1 Nonlinear Wave Effects

Often in experiments, waves are observed to exhibit nonlinear behaviour. For instance, as a wave's amplitude increases, it can begin to change shape, generating Fourier components at other frequencies. A wave that changes from a sinusoidal form to a less symmetric pattern develops more Fourier components at other wave numbers. This wave can often "break" like ocean waves as they move to shore, converting wave energy into thermal energy of the particles. Furthermore, the waves can trap particles in potential troughs, as seen in nonlinear Landau damping, and actually change the property of the medium in which it propagates.

When a plasma is strongly excited to form a continuous spectrum of frequencies, the plasma is considered "turbulent". In a turbulent plasma, the electrons are slowed down by collisions with random electric field fluctuations, rather than with ions, a phenomenon known as "anomalous resistivity". This effect is used in ohmic heating of plasmas to attain high temperatures where ordinary resistivity is insufficient. In terms of the physical mechanism, waves can interact using the fluid approximation and neglecting the contributions of individual particles. A wave first decays by generating harmonics of its fundamental frequency, and then those harmonics interact with each other to form waves at the beat frequencies. Next, these waves continue to grow larger and interact to form many more beat frequencies until the frequency spectrum becomes continuous. At this point, turbulence has developed and can be described in terms of long-wavelength and short-wavelength modes. In fluid dynamics, the long-wavelength modes tend to decay to short-wavelength modes since the large eddies contain more energy and can only decay by splitting into

smaller, less energetic eddies. These small eddies can convert their kinetic motion into heat by viscous damping. In a plasma, the opposite usually occurs and short-wavelength modes coalesce into less energetic long-wavelength modes.

2.7.2 Electron Motion in a Laser Field

The motions of single particles can be used to better understand the force on an electron in a laser field. If the electric and magnetic field of the laser are written as plane waves propagating in the x-direction, then $\mathbf{E}(\mathbf{r},t) = E_0 cos(\omega_L t - kx)\hat{y}$ and $\mathbf{B}(\mathbf{r},t) = B_0 cos(\omega_L t - kx)\hat{z}$ where $k = 2\pi/\lambda$ for the laser wavelength, λ, and $\omega_L = 2\pi c/\lambda$ for the angular laser frequency, ω_L. The nonrelativistic Lorentz force indicates the equation of motion for an electron in this laser field,

$$m_e \frac{\partial \mathbf{v_e}}{\partial t} = -q[E_0 cos(\omega_L t - kx)\hat{y} + \mathbf{v_e} \times B_0 cos(\omega_L t - kx)\hat{z}]. \tag{64}$$

Using the phase velocity $v_\phi = c = \omega_L/k$, it can be shown by Faraday's Law that $|\mathbf{E}| = |\mathbf{B}|\omega_L/k = cB_0$. This indicates that the magnetic field contribution is negligible for $|bfv_e| \ll c$, reducing the expression to:

$$v_e = -\frac{qE_0}{m_e\omega_L} sin(\omega_L t - kx). \tag{65}$$

This motion is an oscillation in the direction of the electric field with a peak velocity, the quiver velocity $v_{quiver} = eE_0/m_e\omega_L$, that is phase-shifted with respect to the driving field. The quiver energy that the electron gains during oscillation is known as the ponderomotive potential and is given by

$$\Phi_p = \frac{e^2 E_0^2}{4 m_e \omega_L^2} \sim I\lambda^2 \tag{66}$$

where I is the laser intensity. The ponderomotive force, $\mathbf{F_p} = -\nabla\Phi_p$, will physically push electrons away from regions of locally higher intensities, orthogonal to the laser propagation.

This means the electron will begin to drift away from the laser focus, gaining a velocity of $v \sim v_{quiver}$ along the way.

2.7.3 Ionisation Mechanisms

Laser pulses can ionise materials via several mechanisms including: the photoelectric effect, multi-photon ionisation, tunnelling ionisation, and barrier suppression. For a single-photon ionisation process, a photon of energy $E = h\nu$, where $h \sim 6.63 \times 10^{-34}$ J·s is Planck's constant and ν is the photon frequency, can ionise an atom by exciting an electron into a continuum state. By overcoming the ionisation potential $E = h\nu_0$, the resultant electron will have an energy of $E = h(\nu - \nu_0)$. For instance, the hydrogen atom has an ionisation potential of 13.6 eV which corresponds to a 90 nm wavelength photon. When the laser intensity increases above $\sim 10^{10}$ W·cm^{-2}, the atom can absorb multiple photons via a series of virtual states to overcome the potential well. The ionisation rate is given by $R_N = \sigma_N I^N$ where σ_N is the cross-section for N-photon absorption. The electron undergoes quick virtual transitions of energy $h\nu$ until it has achieved enough energy to leave the potential well.

Both the photoelectric effect and multi-photon ionisation assume the atomic binding potential is unaltered by the laser. However, for laser intensities $> 10^{12}$ the structure can be modified by the electric field of the laser. The resultant potential of the superposition of both the nucleus and laser contributions, indicates

$$\Phi(r) = -\frac{Ze^2}{4\pi\epsilon_0 r} - eEr. \tag{67}$$

This means the Coulomb barrier has been suppressed to a lower potential, allowing an electron to 'tunnel' through the barrier. When the laser's electric field is strong enough, the potential can be suppressed below the binding energy of the atom, allowing an electron to escape spontaneously. This process known as 'barrier suppression' can occur when the laser's electric field is $E = (E_i on^2 \pi\epsilon_0)/(Ze^3)$ for an ionisation potential E_{ion}. Furthermore,

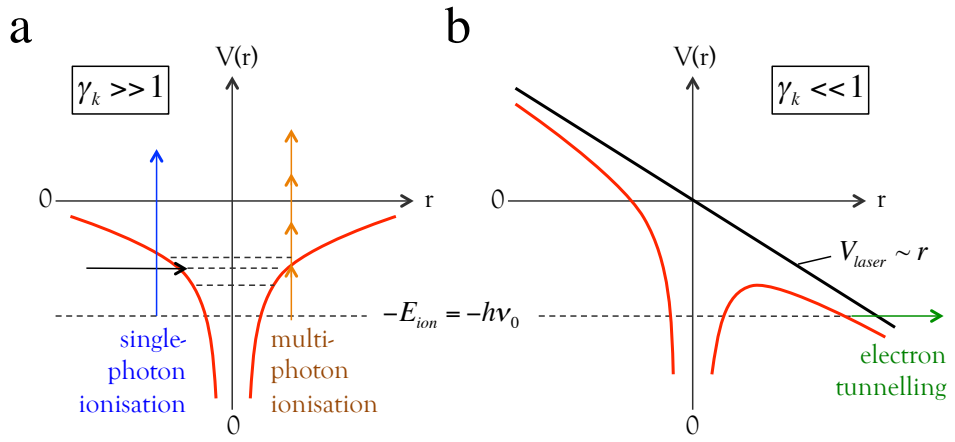

Figure 13: **Ionisation mechanisms for laser-matter interactions. a,** For $\gamma_K \gg 1$ and lower laser intensities, single-photon and multi-photon ionisation dominates. **b,** For $\gamma_K \ll 1$, and higher laser intensities, the potential well is distorted and electrons can escape via tunnelling or barrier suppression.

to determine which process dominates [52], we can examine the Keldysh parameter $\gamma_K = (E_{ion}/2\Phi_p)$, where the ponderomotive potential is $\Phi_p \approx I\lambda^2$ and represents the quiver energy an electron acquires during oscillation. For $\gamma_K \gg 1$, the multi-photon ionisation process dominates while for $\gamma_K \ll 1$ the potential is distorted by the laser, resulting in tunnelling ionisation and barrier suppression.

2.7.4 Absorption of Electromagnetic Waves

Absorption of laser light can occur from either collisional or non-collisional processes. In the case of collisions, laser-heated electrons can transfer energy to the plasma through deflections in the ion Coulomb fields within the plasma. In the absence of collisions, the electrons undergo oscillatory motions in the laser field and no net energy gain. Collisions with ions disrupt the oscillatory motions of electrons, transferring energy into randomised plasma thermal energy– called 'Inverse Bremsstrahlung Heating'. Assuming the

electrons contribute their peak energy to the plasma upon every collision, the heating rate is $n_e \upsilon_{ei}(1/2 m_e v_{quiver}^2)$ where the quiver velocity is $v_{quiver} = eE/m_e\omega_L$. Furthermore, if we assume that $(\upsilon_{ei}/\omega_0)^2$ is small enough to be ignored in Equation 63, we can consider $k = k_r + ik_{EM}/2$ to solve for laser absorption. Here k_r is the spatial rate of absorption of the laser energy and $k_{EM}/2$ is the spatial rate of change of the electric field, E. Solving Equation 63, for the case of $k_{EM} \ll k$, the absorption of laser light is

$$k_r = (\omega_0/c)\sqrt{1 - n_e/n_{crit}} \quad \text{and} \tag{68}$$

$$k_{EM} = \upsilon_{ei}\frac{\omega_{pe}^2}{\omega_0^2}\frac{1}{c\sqrt{1 - n_e/n_{crit}}} = \frac{\upsilon_{ei} n_e}{v_g n_{crit}} \tag{69}$$

where v_g is the group velocity of the laser light. This means the proportion of laser light energy that participates in electron oscillations, n_e/n_{crit}, can be affected by electron-ion collisions at a rate of υ_{ei}/v_g, the temporal collision rate divided by the rate of energy propagation in space.

The plasma can also gain energy from non-collisional processes such as resonant absorption. Resonant absorption can occur when the laser is near the critical density and can excite an electron plasma wave travelling at v_g. Background electrons in the plasma travelling faster or slower than the plasma wave experience a sinusoidally varying potential but are out of phase with it and experience no net effect. However, electrons with velocities close to v_g will see a stationary potential and may become trapped within the troughs of the potential. These electrons are resonant with the wave and can be accelerated. According to Ginzburg (1964), this process only occurs for long scalelength plasmas where there is sufficient underdense plasma. Resonant absorption cannot be driven with a purely normal incidence light beam. Irradiation at an oblique angle allows the electric field to be directed up the density gradient at reflection and reduces the maximum density to $n_e = n_{crit}\cos^2\theta$ with an evanescent field at the critical density [53].

Short-scalelength absorption processes can occur as L/λ decreases and the classical resonant absorption becomes less effective. From a physical perspective, the electrons at the boundary of an overdense plasma surface become accelerated by the electric field of the laser. They then return back into the overdense plasma with a random phase and velocity $v_e \approx eE_{laser}/m_e\omega$ where the laser field no longer has an effect due to shielding. In terms of energy, as the field changes direction, the electrons can gain enough kinetic energy to penetrate the critical surface and move independently of the laser field as they change direction. Therefore, a fraction of laser energy can be coupled into the plasma, and for intensities $\geq 10^{15}$ Wcm^{-2}, this fraction can be up to 70%. This type of absorption is known as "vacuum heating" or "Brunel absorption".

For relativistic intensities $\geq 10^{18}$ Wcm^{-2}, the magnetic field of the drive laser becomes significant and can begin to heat the plasma by "relativistic $\mathbf{J} \times \mathbf{B}$ heating". The Lorentz force drives a longitudinal oscillation in the electrons and upon a break in symmetry, this oscillation can accelerate hot electrons into the plasma. The electrons are accelerated twice by the magnetic field per laser cycle. This phenomenon is unique in that it is most effective at normal incidence to the plasma unlike other mechanisms previously mentioned which require obliquely incident light.

2.7.5 Landau Damping

Landau damping is the damping of longitudinal waves in plasma that prevents instabilities from developing by creating a region of stability. Landau damping is prevalent in collisionless plasmas and has astrophysical applications. For instance, in galaxy formation, Landau damping can halt the instability growth of the gas of stars which causes spiral arms to form. This effect is linked to particles with velocity close to the resonant velocity of the wave. Since they move with the wave and do not see an changing electric field which allows them to exchange energy with the wave effectively. A simplified physical explanation for

Landau damping can be represented by a surfer on waves. If a surfer is not moving, then he will bob up and down as waves pass and on average, gain no energy from the passing wave. However, if the surfer starts at a speed close to the speed of the wave, he will get caught up in the flow and gain energy as the wave loses energy (or dampens). However, if the surfer is moving faster than the wave, the surfer losing energy and the wave gains some energy.

In a plasma, there are both faster and slower moving particles. From the Maxwelliam distribution, there are more particles moving slower than the phase velocity, so on average the wave loses energy. Furthermore, particles moving close to the phase velocity are trapped in the wave, resulting in a flattening of the particle distribution near this phase velocity. However, if the particle distribution included more fast moving particles, than the wave would gain energy from the particles. This occurs in the finite-temperature analogy of the two-stream instability.

2.7.6 Parametric Instabilities

Parametric instabilities can arise during wave-wave interactions in a plasma. Let's consider two cases: when $\omega_0 < \omega_\phi$ and $\omega_0 > \omega_\phi$. For the first case, let's assume there is a small density perturbation in the plasma and the wave is being driven at ω_0 with an electric field E_0. Since the wave frequency is less than the phase frequency, it represents the motion of the cold electron fluid. These electrons will move in the opposite direction of the electric field while the massive ions remain nearly stationary on the relevant time scales. This charge separation then causes an electric field E_1 to form that oscillates at ω_0. The ponderomotive force pushes the electrons from regions of low density to regions of high density, bringing the ions along for the ride:

$$F_p = -\frac{\omega_\phi^2}{\omega_0^2}\frac{\partial}{\partial x}\frac{\langle 2E_0E_1\rangle}{2}\epsilon_0 \tag{70}$$

The result is an instability that grows until the ponderomotive force is sufficient to overcome the pressure that smooths out the density. This parametric instability is known as the "two-stream instability". For the case of $\omega_0 > \omega_\phi$, the ponderomotive force instead moves ions from regions of high density to regions of low density. The electrons will oscillate at a large amplitude if the pump field is near the natural frequency of the electron fluid. Therefore, both the ion and electron waves are excited at the expense of the pump wave, giving way to the "parametric decay instability" often seen in the ionosphere.

Chapter 3

Instrumentation and Experimental Methods

3.1 High-Energy Lasers

Nature often creates high-energy-density conditions with pressures ≥ 1 Mbar found in powerful events such as supernova explosions, jets emanating from accretion disks, and even conditions within the core of planets such as Jupiter. To study this astrophysical phenomena, it is necessary to create similar high-energy-density conditions in the laboratory. For instance, a laser-produced shock wave might travel at 10 km/s in a material that is ~ 1 g/cc, corresponding to 1 Mbar of pressure, which falls within the realm of high-energy-density physics [12]. To create these conditions, we need to employ lasers that are capable of depositing large amounts of energy within a short amount of time onto a target. Here we will introduce high-energy lasers, including the quantum mechanical description, laser construction, and examples of large laser facilities.

3.1.1 Quantum mechanical description of lasers

Let's establish the quantum mechanical description before moving onto specific types of facilities. In 1917 Albert Einstein postulated that a beam of radiation passing through a material can gain energy by inducing excited atoms to emit identical photons – stimulated emission. It was not until 1960 that Theodore Maiman of Hughes Laboratories harnessed this result to obtain light pulses from a ruby crystal rod excited by a flash-tube – the first

laser [54]. The guiding principle behind a laser is that amplification of radiation can occur when radiation interacts with matter; specifically, when photons interact with electrons.

There are many ways in which radiation can interact with matter including but not limited to: absorption, spontaneous emission, and stimulated emission. Considering a simple, two energy level system of an atom where E_1 represents the energy in the lower level and E_2 represents the energy in the upper (excited state) level, these three processes can be defined more concisely. Absorption occurs when an atom's electron in the lower level is excited to the upper level by a photon of energy $\hbar\omega_{21}$. The rate by which atoms are excited to the upper level is $N_1 B_{12} \varrho(\omega_{21})$ where N_1 is the number of atoms per unit volume in level 1, B_{12} is a constant, and $\varrho(\omega_{21})$ is the energy density of radiation of angular frequency ω_{21}. When atoms are in an excited energy state, the system becomes unstable and will eventually decay back down to its ground state. Spontaneous emission occurs when atoms decay from the upper to lower level, emitting a photon of corresponding energy $\hbar\omega_{21} = E_2 - E_1$. The rate at which atoms decay to the lower level 1 is $N_2 A_{21}$ where N_2 is the number of atoms per unit volume in level 2 and A_{21} is a constant. However, Einstein's exciting result was that an incident photon could trigger the decay of an atom in an excited state, releasing a second photon of energy $\hbar\omega_{21}$ known as stimulated emission. The rate at which stimulated emission occurs is equal to $N_2 B_{21} \varrho(\omega_{21})$ where B_{21} is also a constant.

The three constants A_{21}, B_{12}, and B_{21} are known as Einstein's coefficients and represent the probability of such an event occurring in an atom. The relation between spontaneous and stimulated emission is

$$\frac{A_{21}}{B_{21}} = \frac{\hbar\omega_{21}^3}{\pi^2 c^3} \tag{71}$$

where $g_1 B_{12} = g_2 B_{21}$ and g_i refers to the degeneracy. However, our goal is to understand how these forms of emission relate to a laser. The key to a laser is 'population inversion', meaning that there are more atoms in the upper state which allow for optical gain in the

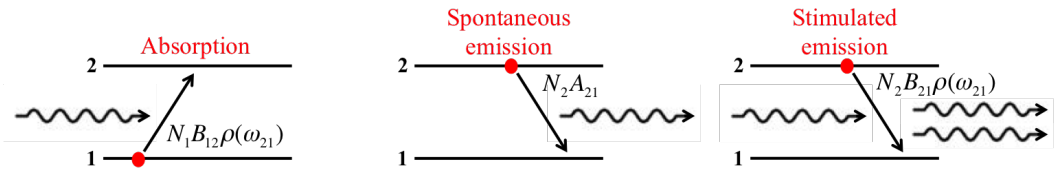

Figure 14: **The interaction of radiation and matter.** Einstein identified three processes by which radiation could interact with matter: absorption, spontaneous emission, and stimulated emission. The schematics shown read from left to right and show that the energy separation between an upper (excited) energy level, E_2, and lower energy level, E_1, is simply $\hbar\omega_{21}$. The number densities are given by N_1 and N_2, the energy densities are denoted by $\rho(\omega_{21})$, and the Einstein coefficients (A_{21}, B_{12}, B_{21}) are used to describe the transition rates for each phenomena. For instance, absorption occurs when a photon excites an electron from the lower energy level, E_1, to a higher energy level. Excited states are not stable and eventually decay back down to a more stable configuration at a rate N_2A_{21}, releasing a photon of equal energy to the originally absorbed photon.

system. In order to achieve population inversion, $N_2 > \frac{g_2}{g_1}N_1$ and the system is no longer in thermal equilibrium. Furthermore, the optical gain cross-section of the laser transition can be described in terms of an incident photon, ω, as

$$\sigma_{21}(\omega - \omega_0) = \frac{\pi^2 c^2}{\omega_0^2} A_{21} g_H(\omega - \omega_0) \tag{72}$$

where $g_H(\omega - \omega_0)$ is the normalised homogenous line-shape. This equation describes the strength with which an incident photon can interact with an atom. For incident photons of frequency similar to the central frequency ω_0, the optical gain will be large. In fact, saturation occurs at an intensity $I_s = \frac{\hbar\omega}{\sigma_{21}\tau_2}$ where τ_2 is the fluorescence lifetime of the upper level.

Why is this important? For the high-energy laser systems used in Chapters 4 – 6, one of the goals of the laser design is to optimise the energy output. Therefore, a high saturation intensity I_s, or fluence, is required for high energy output. Reducing the optical gain cross-section, σ_{21}, increases the saturation intensity and the population inversion density. When

more energy is stored in the population inversion, more energy can be extracted in the laser pulse. To put this in practical terms, for a Nd:glass laser, $\sigma_{21} = 4.1 \times 10^{-20}$ cm^2, many orders of magnitude less than a handheld laser pointer $\sim 10^{-12}$.

Quite possibly the most profound results from the quantum mechanical description refer to timing. It is not useful to us if an absorbed photon is immediately emitted back out. Instead we want the system to absorb as many photons as it can, build up a large number of excited states, and then release a large number of photons in a burst of high energy. The time dependence of the energy levels can be written as

$$\frac{dN_2}{dt} = R_2 - \frac{N_2}{\tau_2} \tag{73}$$

$$\frac{dN_1}{dt} = R_1 + N_2 A_{21} - \frac{N_1}{\tau_1} \tag{74}$$

where R_1 is the pump rate of atoms per unit volume to the lower laser level and R_2 is the pump rate of the upper level. For steady-state conditions, these two equations can be rearranged into the form

$$\frac{R_2}{R_1}\frac{\tau_2}{\tau_1}\frac{g_1}{g_2}\left[1 - \frac{g_2}{g_1}A_{21}\tau_1\right] > 1. \tag{75}$$

This indicates that at least one of the following situations must be met: (1) Selective pumping ($R_2 > R_1$)– the upper laser level is pumped more quickly than the lower laser level; (2) Favourable lifetime ratio ($\tau_2 > \tau_1$)– the lower level decays much faster than the upper level, resulting in a small population of the lower level; and/or (3) Favourable degeneracy ($g_1 > g_2$) where the population per state of the lower laser level is small. Additionally, it is necessary but not sufficient for $A_{21} < \frac{g_1}{g_2}\frac{1}{\tau_1}$ so that the lower level can empty sufficiently quickly for population not to build up by spontaneous emission on the laser transition.

3.1.2 Solid-state laser construction

Solid-state lasers use optically pumped transitions within ions doped as an impurity species into a solid host. They are one of the most common types of lasers in high-energy density physics because they are capable of producing very narrow bandwidth radiation over the electromagnetic spectrum between near-infrared and ultraviolet wavelengths [55]. In the previous section, a two-level laser system was described. However, most solid-state lasers make use of a four-level laser system to optimise the population inversion for maximum radiation output.

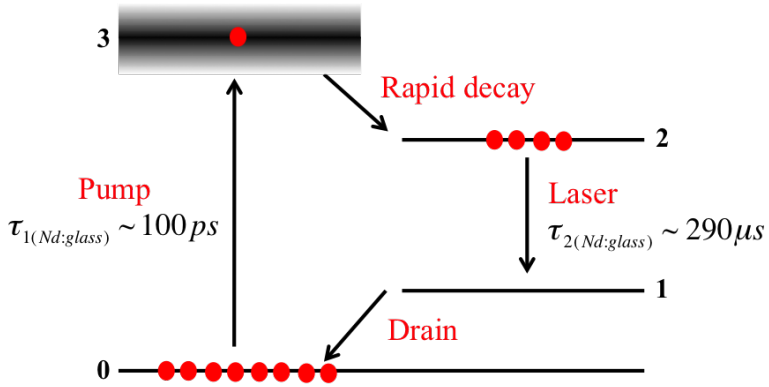

Figure 15: **Schematic diagram of a four-level laser system.** Many optically pumped solid-state laser systems make use of four energy levels to optimise the radiation output. Absorption occurs from level 0 to level 3. For a typical Nd:glass laser, much like the Vulcan laser used for the experiments in this thesis, the timescale is ∼100ps. Electrons in level 3 are unstable and rapidly decay to level 2 which is slightly more stable and has a characteristic decay time of $\sim 290\mu$s for Nd:glass lasers. To create a large population inversion, the laser occurs on the transition from level 2 to 1, and the final transition to level 0 is known as the drain.

A four-level laser system, as seen in Figure 15, optically pumps bands $0 \rightarrow 3$. These pumps bands are broad in their nature, making it easier to match the pump light's wavelength. This means a four-level laser can be pumped by a broad-band, readily available source such as a flashlamp. Once an electron is excited to level 3, it decays rapidly through

non-radiative processes down to level 2. This is where the electrons sit until a population inversion is achieved. The laser occurs on the transition from level 2 to level 1, and then the final transition down to level 0 is called the 'drain'. Though it is possible to create a laser without a drain, population inversion is easier to attain with this last level. For instance, in a 3-level laser system (without a drain), a population inversion would need to be created from level 0 to level 2 which can be difficult if the ground state population is large. A four-level laser system allows a population inversion to be attained between level 1 and level 2, which is ideal because the population in level 1 is quite often much less than level 0 . The important feature to note here is the timing. For a typical solid-state laser, $\tau_1 \ll \tau_2$ which fulfils the favourable lifetime ratio needed for a laser. In fact, Nd:glass lasers have $\tau_1 \sim 100$ps and $\tau_2 \sim 290\mu$s, allowing the system plenty of time to achieve a population inversion.

The simplest construction of a solid-state laser consists of a gain medium which is pumped by some form of radiation within the confines of an optical cavity. This is typically referred to as the ' laser oscillator' and is used to increase the power of an input beam. In high-powered lasers, the output energy can be further increased by large amplifiers which, in the case of the National Ignition Facility, can be as long as three (American) football fields.

Solid-state lasers use either crystal, glass, or ceramic gain mediums, and the exact choice makes a profound impact on the resultant laser properties [55]. When choosing a gain medium, the physical properties to consider include: hardness which allows for optical-quality polishing; high thermal conductivity, so the waste heat may be conducted away rapidly; ease of growth to meet the size requirements of the laser; low thermal lensing which refers to the spatial variation of the refractive index of the laser gain medium arising from spatial variations in temperature and thermal stresses within the material; and low thermally induced birefringence which is the change in refractive index resulting from thermally induced strain within the crystal.

The lasers used in the author's experiments employ glass gain mediums. Glass can easily be shaped in many forms and sizes, preserving the homogeneity and optical quality. Large, planar sheets are prevalent on the NIF laser. Furthermore, glass is inexpensive and has low birefringence. Thermal management of glass gain mediums can be difficult due to low thermal conductivity and optical transitions that are always inhomogeneously broadened. This can be an advantage for high-energy lasers though. First, broad-band sources such as flashlamps can be used to pump such materials because the output laser will also be broad. Second, this implies that the optical cross-section will be small, allowing the system to build up a larger population inversion. Overall, glass hosts are able to extract more energy in a laser amplifier than, for instance, a crystalline host.

The gain medium can then be optically pumped by either a flashlamp or diode laser. Inexpensive, pulsed flashlamps are often employed on laser facilities and operate at several hundred millibars pressure with a discharge current of $\sim$100 A. The spectral output of a common Krypton flashlamp supplies weak emission lines that are dominated by a broad quasi-blackbody continuum which result from electron-ion recombination and bremsstrahlung radiation. This means the majority of energy from flashlamps is not used to pump the laser. Most flashlamps convert about 50% of electrical energy into radiation that spans several hundreds of nanometers around the resonant frequency of the laser. Typically about 10% of the optical output is absorbed by the pump bands, resulting in significant electrical inefficiencies. Furthermore, some of the energy is used to excite states above the upper laser level. Upon the downward cascade of these levels, energy is lost into the laser medium in the form of heat, resulting in thermal lensing and thermally induced stress. The emission duration is typically 100 μs to 10 ms and can supply 10^7 to 10^8 pulses when not continuously operated. More expensive diode lasers can improve efficiency since they are spectrally matched to the laser pump bands and can convert almost all of the available electrical energy.

The laser, in its simplest form, consists of a gain medium within an 'optical cavity' that

determines the resonant frequency of the resultant laser. The allowed frequencies of a long cavity, in direction z, can be given by

$$\nu_{lmp} \approx \frac{c}{2L_c} p \Rightarrow L_c = \left(\frac{\lambda_{lmp}}{2}\right) p \tag{76}$$

for integers l, m, p and cavity length L_c which indicates the influence of the longitudinal mode, p, on the resultant resonant frequencies. The transverse modes instead influence the spatial profile of the laser. Furthermore, the quality of the laser cavity can be determined by the ratio of the resonant frequencies to the width of the resonance: $Q = \omega_p/\Delta\omega_c$ and can be as high as 10^9. The lifetime of the cavity can be described by: $\tau_c \approx 1/\Delta\omega_c$. The goal of high-energy lasers is to maximise the energy output, so this requires a large Q value. A useful technique for optimising population inversion is called ' Q-switching' and involves the release of controlled pulses of high energy rather than a low energy, steady-state operation [56].

Without going into detail of all the configuration types, a Q-switch is simply a means of keeping the beam within a cavity long enough to build up a large population inversion. For instance, sometimes this involves blocking one of the output mirrors so that the beam bounces back and forth through the gain medium several times to build up excited states. At some point the mirror will become unblocked, releasing the light in one large pulse of high Q value. Solid-state lasers are ideal for Q-switching because the upper level lifetime is quite long ($\sim 100\mu s$) compared to gas lasers with lifetimes of $\sim$ ns. Using flashlamp pumps, the pulse repetition is typically $10 - 50$ Hz yielding pulsed of $5 - 10$ ns duration and energies of $10 - 100$ mJ from the laser cavity. The laser energy can then be increased to hundreds of joules by utilising additional amplifier stages.

3.1.3 Nd: glass lasers

Many solid-state lasers utilise $4f^n - 4f^n$ transitions in trivalent rare-earth ions such as Nd^{3+}, used as a dopant in gain mediums such as oxide-, fluoride-, and sulphide-based glasses. Nd:glass lasers can be pumped by broad band sources but particularly strong pumping occurs between 810 nm and 750 nm. Within this energy band there are ~ 9 pump bands ranging from $^4G_{9/2}$ (19100 cm^{-1}) to $^4F_{3/2}$ (11520 cm^{-1}) that are closely spaced, allowing for rapid non-radiative transitions until the excited ions populate the $^4F_{3/2}$ state. Electrons will stay in this upper level for $\sim 290\mu s$ in a metastable state because the transition down to a lower state, ^4I manifolds, corresponds to an energy difference of ~ 4698 cm^{-1}. This means that the transitions from $^4F_{3/2}$ to the ^4I manifolds is almost entirely radiative [57]. The energy-level diagram of this four-level laser system can be seen in Figure 16.

Lasing occurs on the transition from the $^4F_{3/2}$ to the ^4I manifolds and includes more than 20 transitions to the $I_{13/2}$, $I_{11/2}$, and $I_{9/2}$ levels, ranging in wavelength from 1319 nm to 946 nm. The strongest transition occurs from $^4F_{3/2}$ to the $^4I_{11/2}$ and corresponds to wavelengths of $\sim$ 1054-1062 nm depending on the glass host. Even though several radiative frequencies are being generated from the gain medium, the specific laser output frequency is determined by the size of the cavity. The temperature-dependent laser transition is also strongly inhomogeneously broadened to 6.5 THz ($\Delta\lambda \approx 25$ nm) which means the gain cross-section is small enough to allow for a large population inversion, $\sigma_{21} = 4.1 \times 10^{-20}$ cm^{-2}. The repetition rate of these amplifiers is restricted significantly by the low thermal conductivity of glass. However, the output energy of an Nd:glass laser can reach hundreds of joules or more after passing through several amplifiers, as we will now discuss in terms of both the Vulcan and NIF lasers.

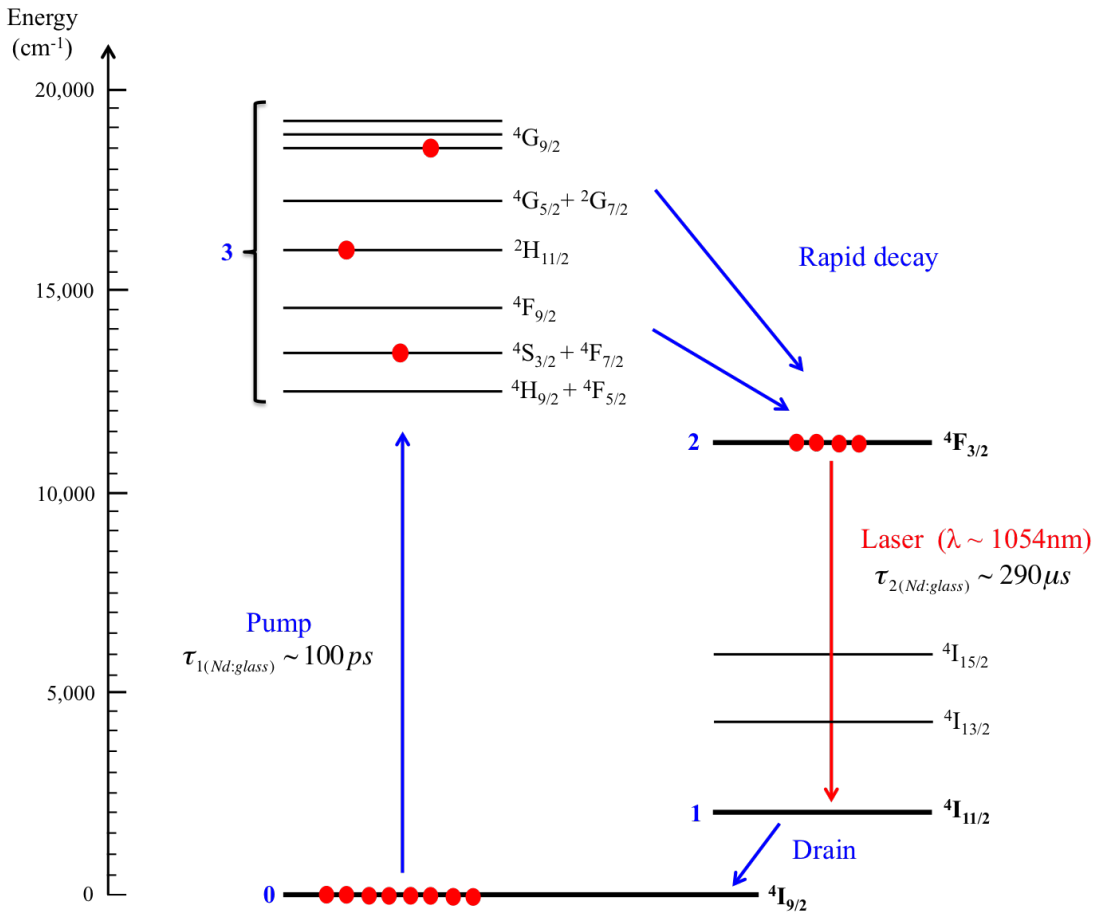

Figure 16: **Energy-level diagram of the Nd:glass laser.** Like many other solid-state lasers, the Nd:glass laser operates as a four-level system which can be pumped from the lowest level, $^4I_{9/2}$, by either a flashlamp or frequency-matched diode laser. There are several pump bands which are closely spaced– this allows for quick transitions down to the metastable level $^4F_{3/2}$. It takes only a few hundreds of picoseconds to pump electrons to the upper level. The energy difference between the upper and lower level ($^4I_{11/2}$) is quite large, so transitions happen much slower, allowing plenty of time for a population inversion to build up. By selecting an appropriate cavity size, the laser occurs on the transition $^4F_{3/2} \rightarrow ^4I_{11/2}$, releasing photons of wavelength $\sim$ 1054-1062 nm.

3.1.4 RAL Vulcan Target Area West laser

The Vulcan laser at the Rutherford Appleton Laboratory is located in Didcot, Oxfordshire, and can deliver hundreds of joules of laser light, producing high-energy-density conditions relevant to astrophysical objects. The facility has two experimental areas: Vulcan Target Area (TA) West (which we will discuss) and Vulcan Petawatt. TA West has eight separate beam lines, two short pulse beams and six long pulse beams. For the purposes of the author's experiments, we will only discuss the relevant long pulse capabilities.

Vulcan can deliver up to 2.6 kJ of 1054 nm light onto a target. The six long pulse beams can each deliver $50-300$ J of energy with a pulse length of $0.5-8.0$ ns with a 150 ps jitter. One of the benefits of using the Vulcan laser is that the beams can each be separated by centimeters or more if desired. In the author's experiment, the facility was able to separate the beams into two cones (3 long pulse beams each) directed at targets separated 6 cm apart. The Vulcan laser is powered by a 3.2 MJ capacitor bank that contains 18 capacitor charging modules each connected to banks of 4 to 5 capacitors. The capacitors can deliver 50 kJ of energy to a series-coupled flashlamp pair in a pulse length of 600 μs with each disc amplifier containing eight flashlamps.

The flashlamps are used to store energy in the rod and disc amplifiers until the laser pulse comes along. When the seed pulse is emitted from the cavity, the laser gets amplified to a few joules of energy by passing through pink-hued Nd: glass rod chains. Vulcan has two rod chains, the simplest of which consists of a 16 mm diameter rod, a 25 mm diameter rod, and a 45 mm diameter rod. However, the laser rods can not be grown large enough to amplify the laser energy up to hundreds of joules. To do this, the facility uses Nd: glass disc amplifiers. After the laser passes through the rods, it continues onto long 1 m slabs of pink glass. Disc amplifiers are particularly useful for high energy lasers which can damage optics easily. Using a Nd: glass disc, the beam diameter can be expanded to 10-20 cm, reducing the spot intensity well below the damage threshold of the gain medium. The

final output beam is directed into the target area where it can be frequency doubled and directed into the 1 m diameter chamber for experiments as seen in Figure 17.

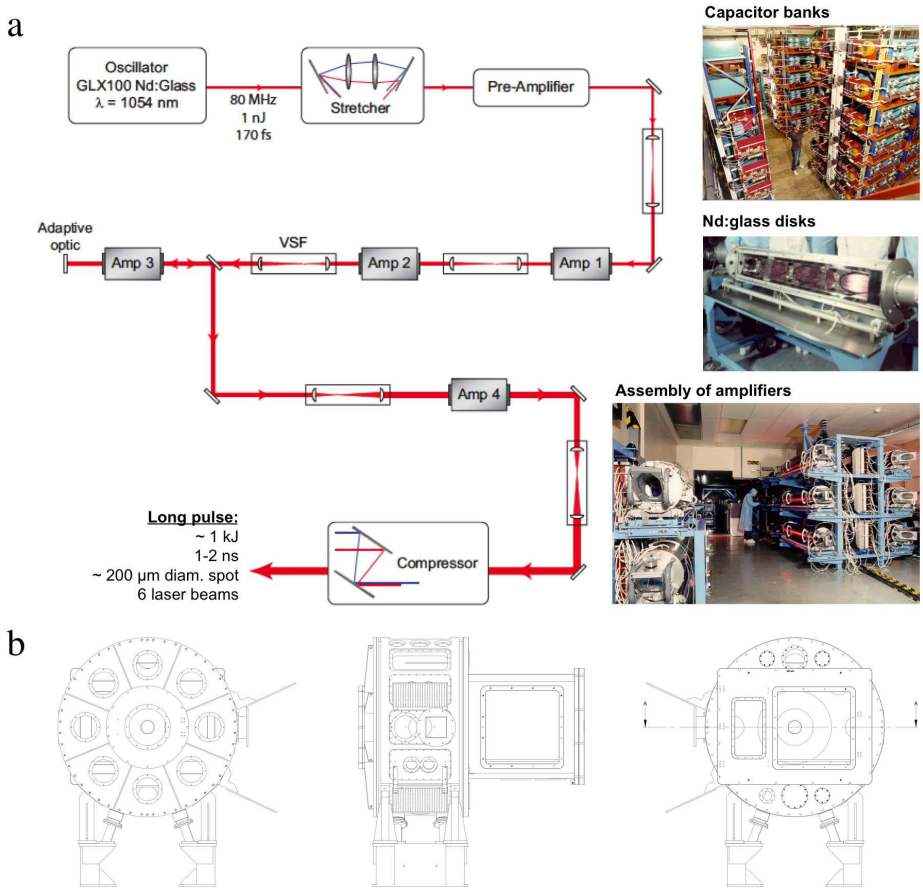

Figure 17: **Schematic diagram of the Vulcan Target Area West laser at the Rutherford Appleton Laboratory (UK). a,** Pulses from the oscillator are stretched so that amplification can be carried out at lower intensities to reduce damage to optics. After several amplification stages and intermediate vacuum spatial filters, the beam is re-compressed to ∼1 ps. An adaptive optic, or deformable mirror, is used to correct for some spatial phase aberrations to improve the focusability. **b,** Schematic diagram of the 1 m diameter target chamber. Laser beams can enter through the ∼ 16 window ports along the side of the cylindrical chamber.

3.1.5 Titan laser

The "Titan" kilojoule-class Nd-glass laser is similar to the Vulcan laser in many ways and was used in Chapter 4 to demonstrate the reproducibility of magnetic field amplification in laser-produced shock waves. Located at the Jupiter Laser Facility at the Lawrence Livermore National Laboratory, the Titan laser features both a long-pulse and short-pulse beam. The long-pulse beam can deliver up to 1 kJ of 1053 nm light within $0.35 - 20$ ns with the option to frequency-double the light. Operating at a repetition rate of two shots per hour, the beam has best focus at 20 μm but can be increased using $200 - 1000$ μm phase plates. The short-pulse beam uses the Janus West beam by replacing its nanosecond oscillator front end with an Optical Parametric Chirped Pulse Amplification (OPCPA) seed pulse and amplifying the chirped pulse with the Janus chain. The amplified chirped pulse is then compressed in a grating compressor using a pair of 40×80 cm multi-layer dielectric gratings. The short pulse can deliver $350 - 530$ J of 1053 nm light in $0.4 - 10$ ps. Though both lasers were used on the experiment, data from the long-pulse laser is only presented in this thesis.

3.1.6 NIF laser

The National Ignition Facility laser is the most energetic laser on Earth. Located at the Lawrence Livermore National Laboratory in California, this facility is the size of three football fields and delivers energies of 2 MJ onto target in a few nanoseconds. The NIF features a Nd: glass laser, supplying 500 TW in 192 beamlines to a 10 m diameter target chamber. Though primarily used for interial confinement fusion research, the NIF provides academic time for 'discovery science' each year. This thesis will present current experimental efforts to measure turbulent dynamo using the NIF. Furthermore, the experimental results in Chapters 4 and 5 allow the author and team to move their experiment to a larger facility.

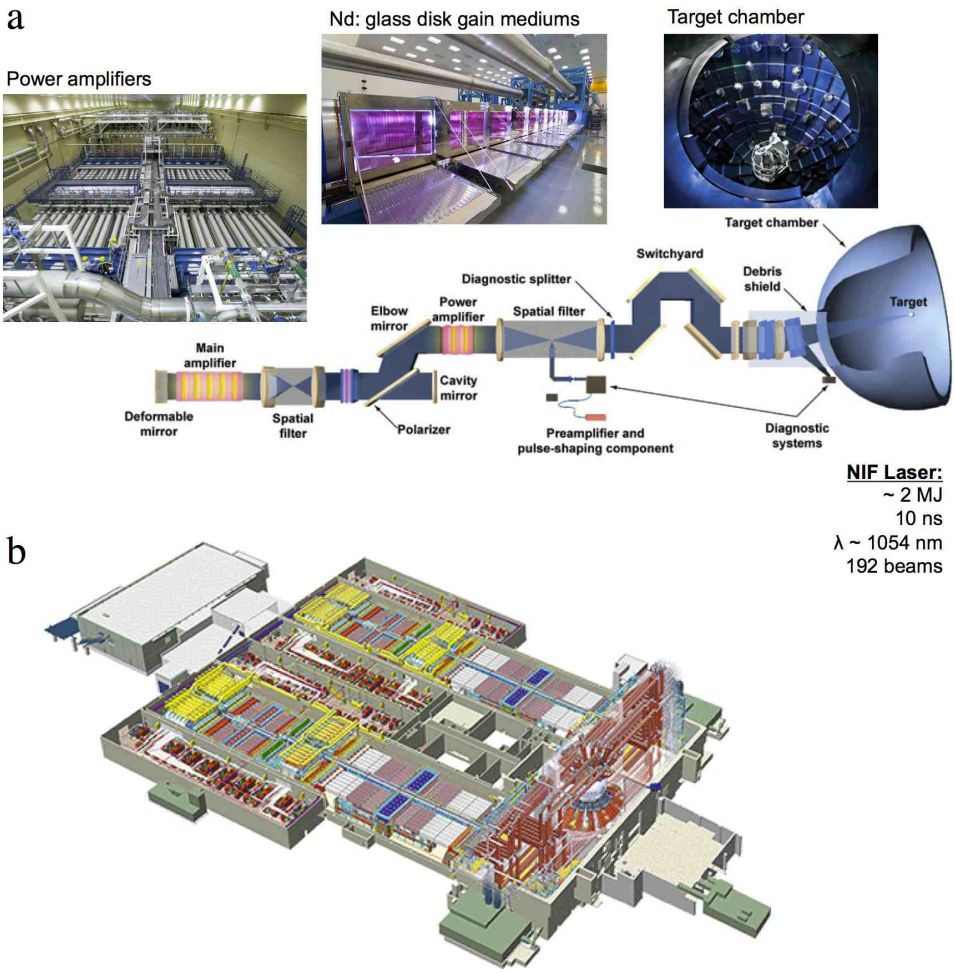

Figure 18: **Schematic diagram of the National Ignition Facility laser at the Lawrence Livermore National Laboratory (USA). a,** The laser originates in the Master oscillator ∼nJ and is amplified by the Preamplifier Modules (PAMs) to ∼mJ and finally through a large series of amplifiers and spatial filters to 2 MJ on target (1.8 MJ in UV). 192 beamlines are directed into a 10 m diameter target chamber. **b,** The NIF drawing, demonstrating the great length of the main amplifier stages.

Construction of the NIF began in 1997 and finished in 2009. By 2010, academic users began taking fundamental science shots. The number of academic shots has increased from 3 shots in 2010 to 21 shots in 2015. Similarly, the number of available diagnostics on the

NIF has increased from 5 in 2009 to more than 50 in 2014. These diagnostics now range from x-ray to optical to nuclear, providing outside users with the opportunity to conduct laboratory astrophysics.

The NIF laser starts with a Master Oscillator which provides a low-power flash of 1053 nm of infrared light to a ytterbium-doped optical fiber. This light is split into 48 Preamplifier Modules (PAMs) containing a two-stage amplifier. In the first stage, the seed pulse is amplified from nanojoules to millijoules by passing $30 - 60$ times through the regenerative amplifier. The second stage amplifies the energy to 6 J by passing four times through a neodymium glass medium. The laser pulses then move onto the main amplifiers which extend 1,500 m in length. Each amplifier is pumped by 422 MJ of electrical energy into 7,680 Xenon flashlamps. The flashlamps excite the Nd: glass discs and the passing pulse picks up the available energy. The beam also passes through several spatial filters that focus light down to a point, filter out the stray rays, and defocus the beam back to a large diameter before the beam passes through large sheets of pink glass gain medium. The beam is finally converted from infrared light to ultraviolet (351 nm) by passing through a potassium dihydrogen phosphate crystal. The resultant energy is $\sim$1.8 MJ.

3.2 Optical Diagnostics

Optical diagnostics are essential in our laser-produced plasma experiments. They allow us to measure the density, temperature, and speed of a plasma– information that is necessary for an astrophysical scaling– with the ease of assembling and aligning diagnostics in optical wavelengths. Here we will discuss three main optical diagnostics: Schlieren, interferometry, and spectroscopy. Both Schlieren and interferometry require a laser probe to backlight the interaction region. As demonstrated in Chapter 2, low-intensity electromagnetic waves can be used for optical image backlighting in regions where the plasma electron density is below the critical density, n_{crit}. As the probe beam light passes through the refractive medium,

phase is added to the wavefronts, allowing otherwise transparent objects to be imaged. In contrast, spectroscopy requires the direct collection of light emitted from the interaction region.

3.2.1 Schlieren Imaging

Schlieren diagnostics can be used to image an otherwise transparent material and determine the position of a plasma flow. After the main beams ablate a target, a second (collimated) probe beam passes through the underdense plasma, undergoing refraction upon traveling through the inhomogenous material. Schlieren was first observed by Robert Hooke in 1665 using a large convex lens and two candles. In his studies, one candle was used as the light source while the hot air rising from the second candle was used as the medium. Conventionally, the diagnostic was developed by August Toepler who used the method to determine the schlieren, or 'streaks', in glass to make lenses.

Schlieren allows us to collect refracted rays of light which correspond to density gradients in the material. After the probe passes through the plasma, a converging lens images the light according to the thin lens equation:

$$\frac{1}{f} = \frac{1}{d_0} + \frac{1}{d_i} \tag{77}$$

where f is the focal length of the lens, d_0 is the distance from the object to the lens, and d_i is the distance from the image of the object to the lens. Some of the rays will be deflected from their original direction due to density gradients while other rays will remain unchanged. To retrieve information about the deflected rays, the light is focused down to a point determined by the focal length of the incident collimated beam. Whereas, rays which are no longer collimated, will focus at a different point. Once the collimated rays come to focus, they can be blocked out with an object (e.g. a knife or dot), leaving behind only the deflected rays to be imaged. In the case of a shock wave, the outer shock envelope

is usually visible, indicating the position of the shock front.

Light travels through a homogeneous material with speed $v = c/n$, where c is the speed of light in vacuum and n is the refractive index of the material. When light travels from a material of refractive index n_a to n_b, the angle of refraction changes: $n_a sin\theta_a = n_b sin\theta_b$. According to Huygen's principle, each point along a propagating wavefront becomes the source of a spherical wave and the sum of these secondary waves determines the form of the wave at any subsequent time. Depicted in Figure 19 are wavelets [58] propagating through a spatially uniform material, n_0, that are continuing to travel in the direction of the initial probe rays. During a given time, Δt, the individual wavelets travel the same distance $\Delta x_0 = \Delta t \cdot c/n_0$ as long as n_0 is equal at all three points. The result is a wavefront parallel to the y-axis.

The inhomogeneous material (e.g. laser-produced plasma) is depicted in shades of blue indicating a positive refractive index along the y-axis such that $\Delta n = (0, dn/dy, 0); dn/dy > 0$. When the wavelets enter into the inhomogeneous environment, they will each travel at a different speed based on the refractive index at that location. For instance, if we consider a wavefront moving from position x_1 to x_2, denoted as Δx, that wavelet will travel in a period $\Delta t = \Delta x \frac{\eta(y_0)}{c}$. Similarly, the wavelets emitted at $(x_1, y_0 + \Delta y/2)$ and $(x_1, y_0 - \Delta y/2)$ travel distances $c\Delta t/n_+$ and $c\Delta t/n_-$ respectively with the substitution $n_\pm = n(y_0 \pm \Delta y/2)$. Therefore, the refracted ray will be deflected by an angle, θ, in the inhomogeneous material:

$$\theta(y) = \frac{n(y)}{n_- n_+} \left(\frac{n_- - n_+}{\Delta y} \right) \Delta x \tag{78}$$

From this equation we can make some more profound statements about the behaviour of the wavefront [59]. For instance, perhaps the refractive index is a function of all three axes $n \rightarrow n(x, y, z)$ and the distance between points along the wavefront is close to zero,

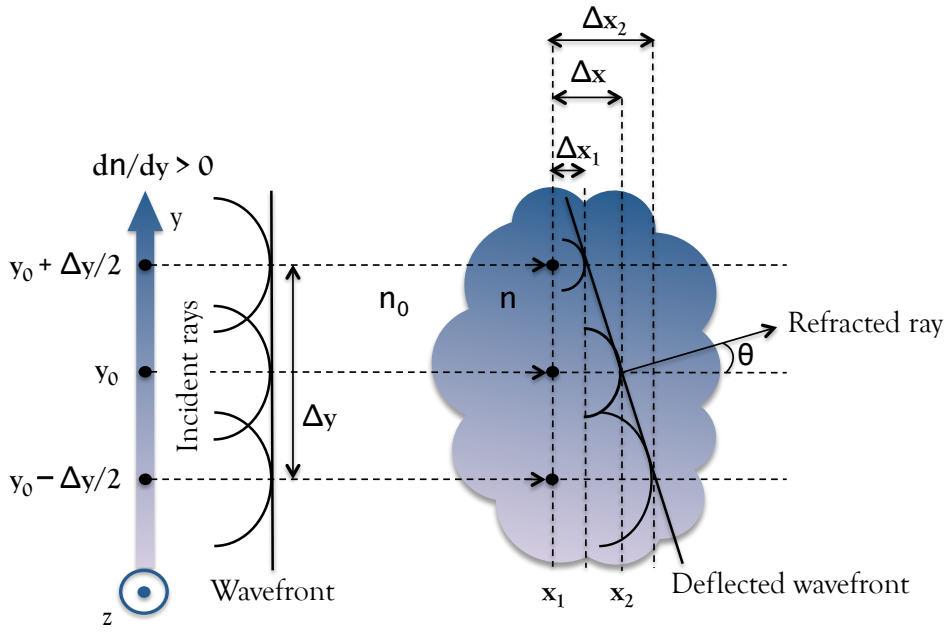

Figure 19: **Visualisation of deflected wavelets in a inhomogeneous material.** Wavelets traveling through a uniform material, n_0, will propagate with an uniform wavefront. Once the wavelets begin to traverse through a material with a changing refractive index, n, along the y-axis, the individual wavelets will travel at different distances depending on the speed at that location. The resultant effect is a deflected wavefront at an angle, θ, from the original trajectory.

$\Delta y \to 0$. Equation 78 can then be generalised to:

$$\theta_y = \int \frac{\partial n}{\partial y} dx \quad \text{and} \quad \theta_z = \int \frac{\partial n}{\partial z} dx \tag{79}$$

This means that any variation in $\frac{\partial n}{\partial y}$ or $\frac{\partial n}{\partial z}$ will result in angular deflection along these axes– a phenomena known as 'shadowgraphy'. These light intensity variations can be projected onto a camera and the deflected rays will shift from the coordinate (y, z) to (y', z') with the translation $y' = y + L\theta_y$ and $z' = z + L\theta_z$. Typical plasma sizes, L, in our experiments are $\sim 1 - 6$ cm. By substitution into Equation 79, the resultant position of

the rays is:

$$(y', z') = \left(y + L\frac{\partial}{\partial y}\int n dx, z + L\frac{\partial}{\partial z}\int n dx \right) \tag{80}$$

In experiments, both the collimated and deflected rays are usually imaged onto a camera, producing a 2D projected image of the light intensity at a specific location in the plasma. If the backlighting probe has uniform intensity, I_0, then the detector will observe an intensity, I_d given by $I_d dz'dy' = I_0 dzdy$ due to the conservation of flux. Substituted into Equation 80, the relative increase in detected signal is proportional to $\nabla^2 n$:

$$\frac{\Delta I}{I_0} = \frac{I_d - I_0}{I_0} = L\left(\frac{\partial^2}{\partial y^2} + \frac{\partial^2}{\partial z^2}\right)\int n dx \tag{81}$$

It is important to note that shadowgraphy will image both the collimated and deflected rays from the probe beam– making it difficult to distinguish the strong density gradients. In order to resolve this information, a lens is placed along the beam path as shown in Figure 20. Collimated rays will all come to focus at a distance f after passing through the lens. Whereas, deflected rays will focus at a different point. By blocking out all of the collimated rays at f, the only remaining light rays are those which were refracted by strong density gradients in the plasma. This is known as ' dark-field' Schlieren.

As seen in Figure 20, the ideal Schlieren stop would be a dot. However, in practice, dots can be difficult to align. Larger diameter dots can help with alignment but at the cost of useful information– small density perturbations will result in small angle deflections that can be easily blocked by a Schlieren dot. Alternatively, a popular choice of stops includes 'knife edges' capable of being aligned at the edge of the focus of the collimated rays. The obvious drawback here is that some of the deflected rays are also blocked, affecting the symmetry of the light intensity of the imaged plasma. For instance, a spherical shock wave might show strong density gradients along one axis but not another which is not entirely representative of the actual density profile. To determine the spot size of collimated rays

in the setup for Chapters 4 and 5, a variety of different Schlieren stops were used until the minimum size ($\sim 500\mu$m) was determined. It is worth noting that there are limitations to the refracted rays which can be collected from this Schileren diagnostic. Small angle deflections can be blocked out by the Schlieren stop itself while large angle deflections might not be collected by the first optic. Assuming the Schlieren stop was close to the minimum width to block collimated rays, then the large angle deflection cutoff is $\sim 7^\circ$ since the first 10 inch collection optic is located 1 m from the plasma interaction region.

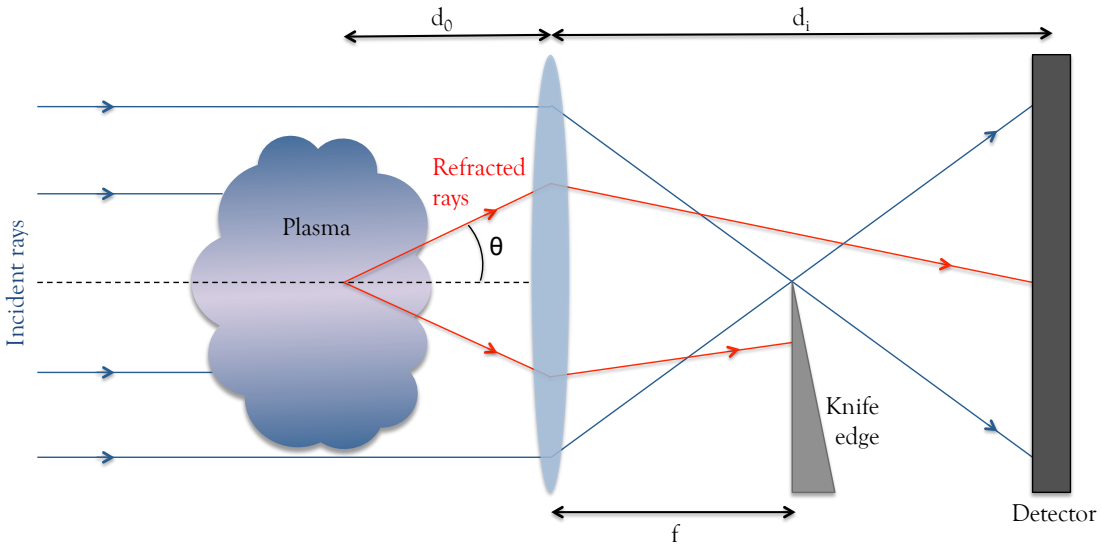

Figure 20: **Ray diagram of the Sclieren diagnostic used to detect density gradients associated with a media.** A collimated probe beam passes through an object of inhomogeneous density, causing light rays to be deflected by an angle, θ. Both the collimated and refracted rays are focused down with an lens, and a knife edge blocks out collimated rays which come to focus at a distance f. The resultant image on the detector is composed of the light intensity from deflected rays, indicating the density gradients in the material.

3.2.2 Mach-Zehnder Interferometer

Interferometry is a technique of measuring the phase difference between two waves, one that is perturbed through a medium and one that is unperturbed, to determine the change in refractive index and therefore electron density of the medium. The resulting interference pattern can be deconvoluted to obtain the phase shift, ϕ, of the original probe beam, and the electron density can be calculated [60] assuming that the refractive index, η, is dominated by the electrons:

$$\eta \approx \eta_e = \sqrt{1 - \left(\frac{\omega_{pe}}{\omega}\right)^2}. \tag{82}$$

For $n_e \ll n_{crit}$, this equation can be simplified to $\eta \approx 1 - (n_e/2n_{crit})$. Furthermore, if the change in refractive index between the medium and vacuum is $\Delta\eta \approx \eta_{plasma} - 1$, then the total phase shift indicates both the change in refractive index and electron density of the medium:

$$\phi = \frac{2\pi}{\lambda}\int_{path}(\eta_{plasma} - 1)dx = -\frac{\pi}{\lambda n_{crit}}\int_{path} n_e dx. \tag{83}$$

A Mach-Zhender interferometer depicted in Figure 21 was used for Vulcan experiments in Chapters 4 and 5. A probe beam is split with a 50/50 beamsplitter optic to produce two identical beams with equal phase. The reference beam remains unperturbed in vacuum while the other beam probes the medium, undergoing a phase shift corresponding to the refractive indexes present in the material. The two beams, taking equal length paths, recombine before imaging onto a camera. The camera detects fringe shifts corresponding the the electron density of the medium [61],

$$g(x, y) = a(x, y) + b(x, y)\cos(2\pi k_0 x + \phi(x, y)) \tag{84}$$

where a and b are scale factors arising from intensity variations and k_0 is the unshifted

spatial fringe frequency. Rewritten in the exponential form to take the Fourier transform:

$$F_x(g(x,y)) = F_x(a(x,y)) + F_x\left(\frac{1}{2}b(x,y)e^{i\phi(x,y)}\right) + F_x\left(\frac{1}{2}b(x,y)e^{-i\phi(x,y)}\right). \quad (85)$$

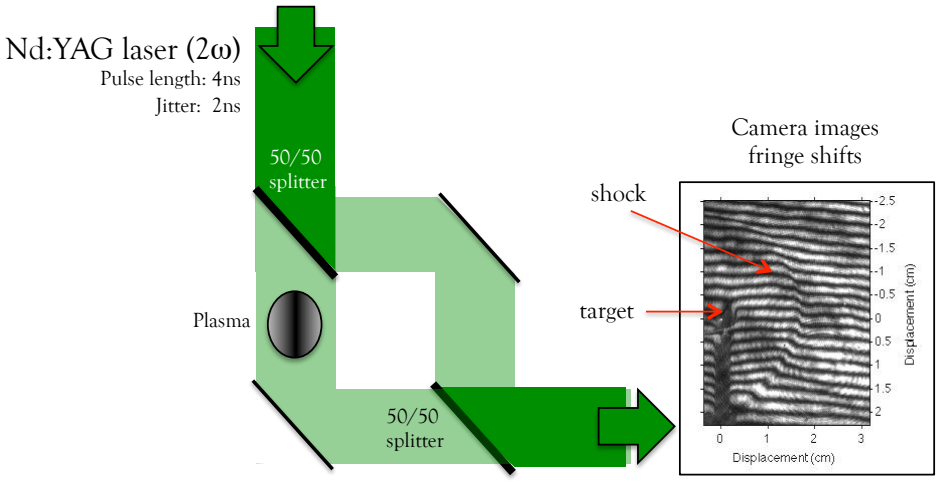

Figure 21: **Mach-Zehnder interferometer to measure the electron density of a plasma.** Two identical beams with equal path lengths are superpositioned to determine constructive and deconstructive interference that produces fringe shifts on a camera. The reference beam travels through vacuum, unperturbed, while the other beam travels through the plasma, undergoing a phase transition due to the changing refractive index of the medium.

In practice, the PAT(Phase calculation Abel inversion and Tomography programme) software, developed by Matthias Hohenberger and James Lazarus, was used to measure the electron density. After taking the Fourier transform in Equation 85, the data is examined in wavenumber space and features two strong peaks shifted by k_0 from the centre. One of these features is selected with a Hann window and shifted back to the centre. Then an inverse Fourier transform is performed to determine $\frac{1}{2}b(x,y)e^{i\phi(x,y)}$, and the imaginary part of the natural logarithm indicates the phase. To determine the electron density, we assume

cylindrical geometry which allows us to perform an 'Abel inversion' to recover an axially symmetric function from a projection. The inverse radial transform [60] in cylindrical coordinates is

$$n_e(r) = \frac{\lambda}{\pi^2} n_{crit} \int_r^R \frac{d\phi}{dy} \frac{dy}{\sqrt{y^2 - r^2}}, \tag{86}$$

where R is the shock wave radius.

3.2.3 Spectroscopy

Spectroscopy is the measurement of radiation intensities as a function of frequency, and the ratio of line intensities can be used to determine electron temperatures within a plasma. There are three types of radiative transitions which can be detected with a spectrometer: bound-bound, bound-free, and free-free. Bound-bound transitions occur when the electron is bound to the atom in both states. Here, the peak intensity is located at frequencies corresponding to $\Delta E = E_2 - E_1$ for two transition levels. Bound-free transitions occur when an electron is ejected out of an atom and into a continuum state, leaving an ionised atom behind. Free-free transitions occur when free electrons are accelerated or decelerated, resulting in emission or absorption. For instance, bremsstrahlung is a type of free-free transition that is characterised by the deceleration of an electron through collisions. This results in a loss of kinetic energy which is converted into a photon. Emitted radiation by bremsstrahlung processes is distributed continuously over all frequencies, unlike line radiation whose peak intensities refer to specific frequencies.

When spectroscopy is employed as a diagnostic, emitted light is collected through a spectrometer, dispersed by a grating, and then imaged onto a camera. The spectral resolution is predominantly determined by the slit width at the entrance of the spectrometer, the choice of grating, and spectrometer length. Typically slit widths of 50-200 μm are used to balance signal with resolution. To increase the spectral dispersion, larger spectrometers (i.e. 1m long) can be used in combination with larger gratings. Gratings are used to

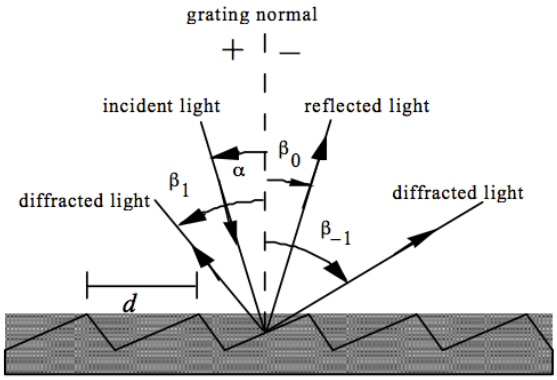

Figure 22: **Diffraction grating used for spectroscopy.** Light rays incident upon a grating are diffracted along several discrete paths. The light undergoes diffraction at an angle $\beta_{1,-1}$ and reflection at an angle β_0. When the grating is at zero order, $m = 0$, the grating acts as a mirror and the wavelengths are not separated. The distribution of power is maximised at the blaze angle $2dsin(\theta_B) = m\lambda$ where the incident and diffracted rays follow the law of reflection when viewed from the facet [62].

diffract light into discrete directions according to the equation: $Gm\lambda = sin(\alpha) + sin(\beta)$, where $G = 1/d$ is the groove density measured in grooves/mm [62]. The angles α and β are depicted in Figure 22 and the blaze angle θ_B is the angle normal to the groove surface where incident and diffracted rays follow the law of reflection when viewed from the facet. Often gratings are blazed for a particular wavelength, λ_B, to maximise efficiency where $\lambda_B = (2d/m)sin(\theta_B)$. The maximum resolving power for a grating is determined by $R_{max} = 2Nd/\lambda$ assuming a uniform groove spacing, d, over the surface. It is worth noting that the grating will diffract light for $m = 1, 2, ...$ so it is possible for a first order spectral line to overlap with a second order spectral line. In practice, the author typically picks a wavelength setting that will mostly employ strong first order lines that do not overlap with troublesome second order lines. The National Institute of Standards and Technology's Atomic Spectra Database provides quick information regarding the brightness of spectral lines that can be used to help plan an experiment.

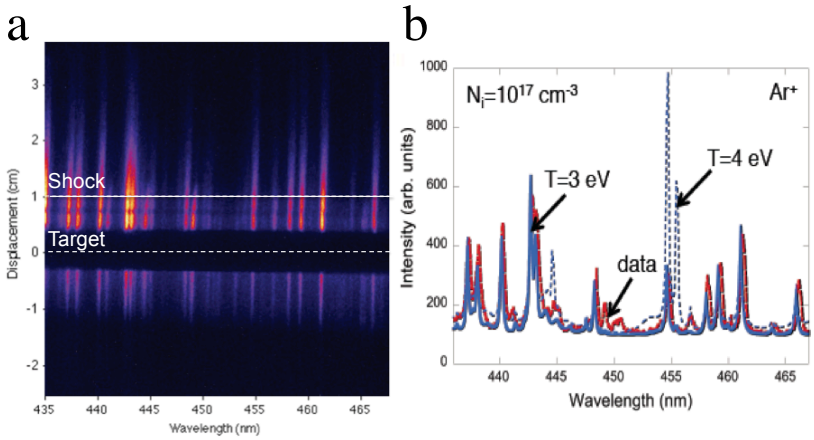

Figure 23: Spectroscopy data (*left*) showing spatially resolved transition lines in singly ionised Argon at 0.3 μs integrated over a camera gate width of 20 ns. A 1 mm wide line-out (*right*) was taken at the position of the shock (1 cm from the target) shown in red with a modelled PrismSPEC fit shown in blue. This shot was conducted at the Vulcan laser facility by ablating a 500μm thick carbon rod with 292 J of green light in an Argon gas filled chamber at 1.12 mbar.

Armed with spectroscopy data, electron temperature measurements can be made by analysing the ratio of line intensities. For an optically thin plasma, the line intensity along the line of sight, s, is

$$I_{2,1} = \frac{1}{4\pi} \int n_2 P_{2\to1} h\nu_{2,1} ds \tag{87}$$

where n_2 is the upper level population density, and P is the transition probability. Thus, the ratio of two line intensities can be written as

$$\frac{I_1}{I_2} = \frac{n_1 P_1 h\nu_1}{n_2 P_2 h\nu_2}. \tag{88}$$

If the two levels are in local thermodynamic equilibrium, then the relative population is only a function of electron temperature. From the Boltzmann relation, we can determine

the relationship between temperature and measured spectral intensities:

$$\frac{I_1}{I_2} = \frac{g_1 P_1 h\nu_1}{g_2 P_2 h\nu_2} exp\left[-\frac{E_1 - E_2}{k_B T_e}\right] \tag{89}$$

where g_1 and g_2 are statistical weights. When spectroscopy is employed in the laboratory, the optical efficiency of the system needs to be determined in order to properly calculate the line-ratio intensities. A calibrated white light source, such as a tungsten lamp, can be placed at the source, or target interaction region. As the light passes through the optics (mirrors, beam splitters, lens, etc.) the light is not necessarily decreased in brightness with spectral uniformity. In fact, many mirrors leak light of higher or lower frequencies and even doublet optics still do not necessarily prevent spectral distortion. By comparing the white light measurement through the system with the known spectral output, the data can be corrected for a better measurement of the plasma temperature. Codes such as PrismSPECT are then used to analyse the ratio of line intensities. PrismSPECT is a collisional-radiative spectral analysis code designed to simulate the atomic and radiative properties of laboratory plasmas.

3.3 Magnetic Field 'Bdot' Probes

High bandwidth, three-axis induction coils known as 'Bdot' probes were used to diagnose transient magnetic fields at a specific location in our laser-produced plasma experiments. The Bdot probes consist of three sets of wired loops that can detect a transient magnetic field passing through the coil [63]. From Faraday's Induction Law, a magnetic field flux through a loop of wires can induce a current, driving an electromagnetic force $\varepsilon = -N\frac{d\Phi_B}{dt}$ where N is the number of loop turns and Φ_B is the magnetic field flux. By measuring the induced voltage on an oscilloscope, we can determine the strength and direction of the passing magnetic field relevant to our laser-produced plasma.

Due to our experimental conditions, it was useful to employ Bdot probes instead of another magnetic field diagnostic for three reasons. (1) Each probe has a bandwidth of ∼200 MHz which means it can detect phenomena on the order of nanoseconds. We are interested in looking at magnetic field evolution on a nanosecond to microsecond scale, so the probes allow us to collect this desired time-history. (2) The magnetic fields produced are quite small (∼ a few Gauss), and the probes have detected fields as small as 0.5 G on Vulcan experiments. The sensitivity limit depends mostly on the noise caused by firing the Vulcan laser, which generates a considerable amount of electronic noise that can be detected by the coils. So the probes meet the sensitivity requirement. (3) Our laser-produced shock waves have electron temperatures of ~ 2 eV, travel at 20 km/s, and carry a $2-5$ G field, resulting in an electron Larmor radius of $200-600\mu$m. The probes used in these experiments have a coil diameter of 1 mm which is close to the Larmor radius and allows us to study in detail the generation of small fields. For these three reasons, the Bdot probes were an ideal tool for our experiments.

3.3.1 Design and Construction

The Bdot probe design has three main features: (1) a tip enclosing coiled wires around a $0.5-3$ mm diameter cubed-core, (2) a shaft and shield that terminates with a 18-pin LEMO cable, and (3) a differential amplifier [63]. Each probe was handmade by the author at the University of Oxford under the guidance of our engineer, Adam Baird. Every probe is custom-made for the type of experiment and has been commissioned for other universities (e.g. Osaka) and private companies (e.g. Lam Research).

The probe tip consists of a cubed core with twin-twisted wires wrapped around each axis as seen in Figure 24. The core is made of Vespel, a high-performance polyimide-based plastic manufactured by DuPont, due to its favourable qualities. Vespel can withstand repeated heating up to 300 °C without altering its thermal and mechanical properties,

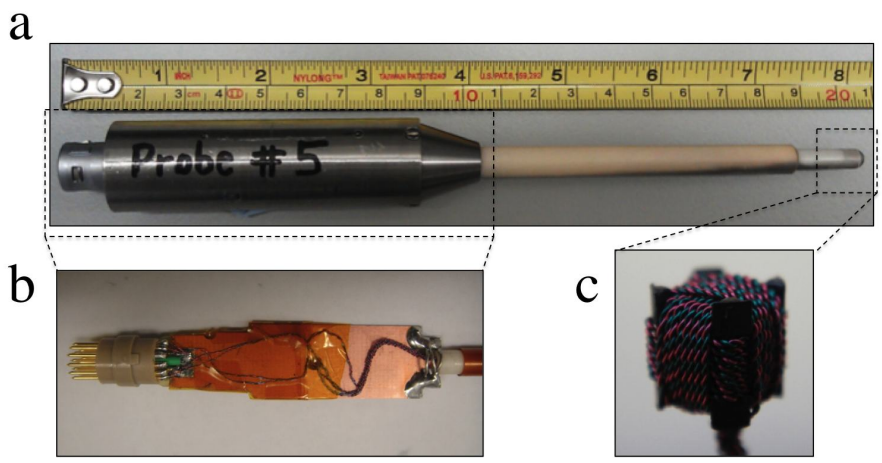

Figure 24: **Bdot probe used to measure transient magnetic fields at a specific location in space. a,** Probe assembly measuring 20 cm in length. Three-axis induction loops are twin-twisted around a **c,** 1 mm cubed core and enclosed in a white, Macor ceramic tube. All of the induction wires are bundled together and twisted down the shaft of a ~ 10 cm long alumina tube. A tungsten and mu-metal shield are used to protect **b,** exposed wires that are soldered to a LEMO 18-pin connector.

making its thermophysical properties highly reproducible and consistent. Furthermore, Vespel SP-1 at 21.8 °C has a low magnetic susceptibility (-(9.02 $\pm$ 0.25) $\times 10^{-6}$) close to that of water at room temperature, indicating that the material should not significantly respond to an applied magnetic field. The cores range in size from $0.5 - 3$ mm diameter. The 1 mm and 3 mm diameter cores can be 3-D printed at the University of Oxford and are carefully designed with 'ears' on each cube corner to hold-in the wired loops as seen in Figure 24(c). The smaller 0.5 mm cores are manufactured by Chris Spindloe at the Rutherford Appleton laboratory.

Each axis has a twin-twisted pair of wires wound around the trough of the cubed core. The wires are twin-twisted to reduce electrostatic noise. Magnetic fields induce equal but opposite voltages in each loop, while induced electrostatic voltages have the same polarity. By subtracting the current in one wire from the current in the other wire, the electrostatic

component (V_E) is eliminated while the magnetic component (V_B) is doubled,

$$V_1 - V_2 = (V_B + V_E) - (-V_B + V_E) = 2V_B. \tag{90}$$

Though time did not permit, the author would have liked to build a probe without the twin-twisted wires to determine, quantitatively, the accuracy of eliminating the electrostatic noise. The 1 mm probes used on the Vulcan experiment employ 50 μm thick insulated copper wires, wound around each axis four times. In addition to these three sets of twin-twisted wires, we also include a fourth set of wires that terminate before the core (but are otherwise identical to the other wires) and do not have a loop at the end. This 'dummy' set of wires is there to assess the level of electrostatic noise still present in the Bdot probe.

In total there are four sets of wires: one set for each of the three axes and one set for the 'dummy' channel. All four sets of wires are twisted together from the base of the cube to the LEMO connector to minimise electrostatic noise. The looped wires are enclosed and epoxied in a 600 μm-1 mm thick, 2 cm long Macor tube. Macor is a machinable glass-cermanic manufactured by Corning Inc. with a white, porcelain, appearance. It acts as a good thermal insulator and is stable up to temperatures of 1000 °C with little thermal expansion or outgassing. The material is primarily silica (46% of SiO_2) with additional magnesium oxide (17%), aluminium oxide (16%), potassium oxide (10%), boron trioxide (7%), and fluorine (4%). The magnetic susceptibility is also desirably low (-0.8 $\times 10^{-5}$).

The 16 leads, four per axis and two per loop, coming off the cube are tightly bundled and twisted down the core of a $\sim$10 cm long alumina tube to reduce any stray electronic pickup. Aluminium oxide (Al_2O_3) known as alumina is an electrical insulator and protects the induction wires from the surrounding plasma. The alumina shaft is secured onto a machined tungsten tube (7 cm in length, 2.5 mm thick) with an additional 1 mm thick Mu-metal shield. Inside the shielding, the wires are organised onto a printed circuit board and connected to the 18-pin LEMO cable. From this configuration, the LEMO cable can

either be connected via coaxial cables to a chamber flange or directly to a coaxial cable that terminates at the differential amplifier box. Each axis pair is terminated with a 50 Ω load at the input of the differential amplifier.

The purpose of the differential amplifier is to mitigate the electrostatic contribution in the induction loops [63]. When the probe is placed in a plasma, there is a potential difference between the probe and plasma, resulting in a capacitive effect on the probe, $V_{electrostatic}$. Since the electronic contribution is about the same on loop 1 and 2, the differential amplifier subtracts these two signals, leaving behind the magnetic field contribution to the voltage, $V_{meas}(t)$. Estimates of the voltage levels and corresponding magnetic field strengths are examined in Section 3.3.3.

3.3.2 Calibration Technique

Before implementation on an experiment, the Bdot probes need to be calibrated in a known magnetic field to determine the characteristic response of the coils [64][65][66]. A time-varying magnetic field is generated with a Helmholtz coil, driven by a network analyser that sweeps frequencies of 9 kHz to 500 MHz. The Bdot probe is placed within the known magnetic field to determine the probe's cross section area, a, of each coil axis and relaxation parameter, τ_s, relevant to the self- and mutual inductance of the wires.

By looking at an individual loop [67], the circuit can be simplified as shown in Figure 25 where the magnetic field $B(t)$ supplied by the Helmholtz coil acts as a voltage source $V_{meas}(t)$. The equation describing this circuit is

$$an\frac{d}{dt}B(t) = \left(1+\frac{r}{R_s}\right)V_{meas,1}(t)+\left(\frac{L_s+M}{R_s}+rC_s\right)\frac{d}{dt}V_{meas,1}(t)+(L_s+M)C_s\frac{d^2}{dt^2}V_{meas,1}(t), \tag{91}$$

where n is the number of turns in a loop, r is the internal resistance of the loop, R_s is the load resistance on the loop, L_s is the self-inductance, M is the mutual inductance between

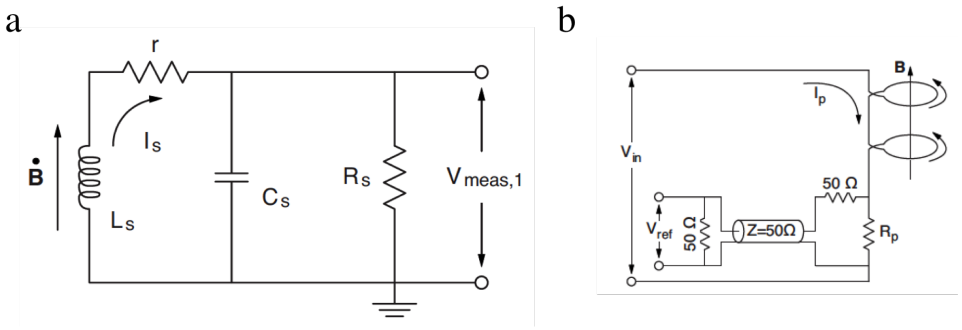

Figure 25: **Circuit diagrams of the Bdot probe calibration technique using a Helmholtz coil. a,** Simplified circuit schematic for an individual loop (loop 1) wound around the cubed core that can detect transient magnetic fields. **b,** Each probe is placed within a Helmholtz coil that is driven by a network analyser during the calibration process. The probes measure an induced voltage from the magnetic field generated by the Helmholtz coils, and the circuit can be represented in this way.

the two sets of loops, and C_s is the internal capacitance of the loop. Taking the Fourier transform of this equation, we can determine an expression between the induced voltage $V_{meas}(\omega)$ and the Helmholtz's magnetic field $B(\omega)$ in frequency space [63]. Assuming the load resistance is much larger than the internal wire resistance ($r/R_s \ll 1$) and $\omega C_s R_s \ll 1$, the resultant equation is

$$\frac{V_{meas}(\omega)}{B(\omega)} = 2g\frac{V_{meas,1}(\omega)}{B(\omega)} = aNg\frac{\omega}{1+(\tau_s\omega)^2}[\omega\tau_s + i]e^{i\omega\tau} \tag{92}$$

for identical loops 1 and 2 where $V_{meas,1}(t) = -V_{meas,2}(t)$. Here g is the differential amplifier gain (measured at 0.5 for our calibrations), N is the total number of turns per axis ($2n = N$), τ_s is a relaxation parameter defined by $\tau_s = (L_s + M)/R_s$, and the expression $e^{i\omega\tau}$ can be expanded to $e^{i\omega\tau} \approx 1 + i\omega\tau$. There are cable length differences between the probe and magnetic field generator circuits, so τ represents the electrical time delay, measured at -16.7 ns with the network analyser. This equation indicates that the capacitor behaves like a short at high frequencies (where $\omega \to \infty$) and puts a limit on the

probes operational frequency range (200 MHz in our case). At low frequencies, $\omega\tau_s \ll 1$, the probe's signal $V_{meas}(t)$ is proportional to the first time derivative of the magnetic field. Whereas at higher frequencies, $1 \ll \omega\tau_s \ll \tau_s/R_sC_s$, all of the frequency dependence drops out and the probe's signal is directly proportional to the magnetic field [63].

The 8 mm radius Helmholtz coil was driven by a Rohde & Schwarz R&S ZNC3 Vector Network Analyser, and a reference voltage $V_{ref}(t)$ was measured across a resistor $R_p = 0.22\Omega$ to compare with the probe's response $V_{meas}(t)$. Through careful placement of the probe tip in the Helmholtz coils, only one axis measured the magnetic field at a time. The network analyser compared the voltage across R_p with the induced voltage in the probe to generate the real and imaginary parts of $V_{meas}(\omega)/V_{ref}(\omega)$. This technique is also used to determine the coil axis to cable lead orientation and the direction of transient fields through the loop. The magnetic field generated by the Helmholtz coils is known and can be described by the following equation:

$$B(\omega) = \left(\frac{4}{5}\right)^{3/2} \frac{\mu_0}{rR_p}[2V_{ref}(\omega)] \tag{93}$$

where $r = 0.008m$ is the radius of the Helmholtz coil, and the relative permeability μ_r of Vespel is close to unity. Due to the unique wiring of our probes in comparison to that of Everson *et al.*, the probes show resonance effects at relatively high frequencies as shown in Figure 26. Using only the approximation that $|\omega\tau| \ll 1$ and therefore $e^{i\omega\tau} \approx 1 + i\omega\tau$, the ratio of the reference voltage and induced voltage is

$$\frac{V_{meas}(\omega)}{V_{ref}(\omega)} = aNg\left(\frac{16}{5^{3/2}}\right)\frac{\mu_0}{rR_p}\frac{\omega}{1+(\tau_s\omega)^2}([\omega\tau_s - \omega\tau] + i[\omega^2\tau_s\tau + 1]). \tag{94}$$

This equation can be used to fit the graphs of $Im\{\frac{V_{meas}(\omega)}{V_{ref}(\omega)}\}$ and $Re\{\frac{V_{meas}(\omega)}{V_{ref}(\omega)}\}$ measured by the network analyser [63]. The two free variables a and τ_s can be adjusted to fit the data as shown in Figure (26). The variable a tends to have a larger effect on the imaginary

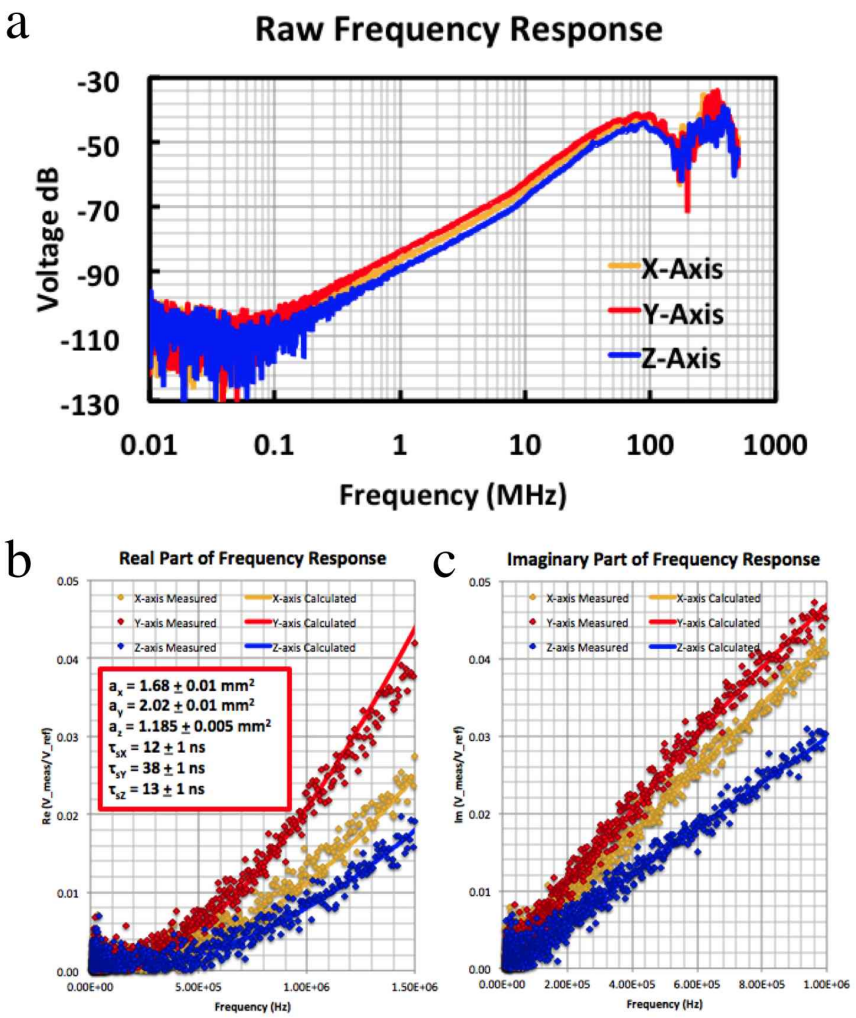

Figure 26: **Calibration data of Bdot probes. a,** Raw frequency response of the probe in a known magnetic field generated by a set of Helmholtz coils. The log-plot of $\frac{V_{meas}(\omega)}{V_{ref}(\omega)}$ data shows a linear trend up to $\sim$ 200 MHz on all three probe axes. **b,** The real and **c,** imaginary components of the induced magnetic field in the probe can each be fit with the expected magnetic field from the Helmholtz coils. By fitting the data, the two unknown variables a, the cross-sectional area, and τ_s, the relaxation parameter, of each axis can be determined. Shown is the calibration of Probe #6 used on Vulcan.

component while τ_s has a larger effect on the real component.

3.3.3 Interpretation of Data

During an experiment, the magnetic field flux at a specific location in space is measured by carefully aligning a Bdot probe to the location and collecting the corresponding voltage trace on a 14-bit 800 MS/s ZTEC ZT4442 oscilloscope. Out of convenience, we align one of the probe axes to the plasma flow. For instance, with laser-produced shock waves, the seed magnetic field is generated by the Biermann battery effect and aligned orthogonal to the plasma flow. By aligning one axis to the flow, we can confine the induced magnetic fields to only two of the three probes axes. This is highly useful during data analysis.

The entire diagnostic assembly includes (in order): 1mm Bdot probe aligned to the plasma flow, 2m long insulated coaxial cables connecting the probe (18-pin connector) to a LEMO flange on the chamber wall with 4-pin connectors, LEMO flange with o-ring seals around twelve 4-pin connectors, 10 m long insulated coaxial cable, low pass 50 Ω filter, attenuators (if needed), differential amplifier box, and finally the ZTEC oscilloscope. This entire setup is reconstructed during the calibration procedure to ensure that the response of the entire assembly (all 12 m of cables and connectors) is taken into consideration.

The voltage trace is collected on the oscilloscope and integrated over time with additional corrections to determine the magnetic field passing through the loops. In the simplest case, the voltage can be integrated using Faraday's Induction Law,

$$aNg\frac{d}{dt}B(t) = \left[1 + \tau_s\frac{d}{dt}\right]V_{meas}(t), \tag{95}$$

and then integrated discretely to solve for $B(t)$. In reality, this procedure is not sufficient to deal with noisy data. Firing a large laser generates a significant amount of electronic noise that can be detected by the probes. Even with the twin-twisted wires and shielding,

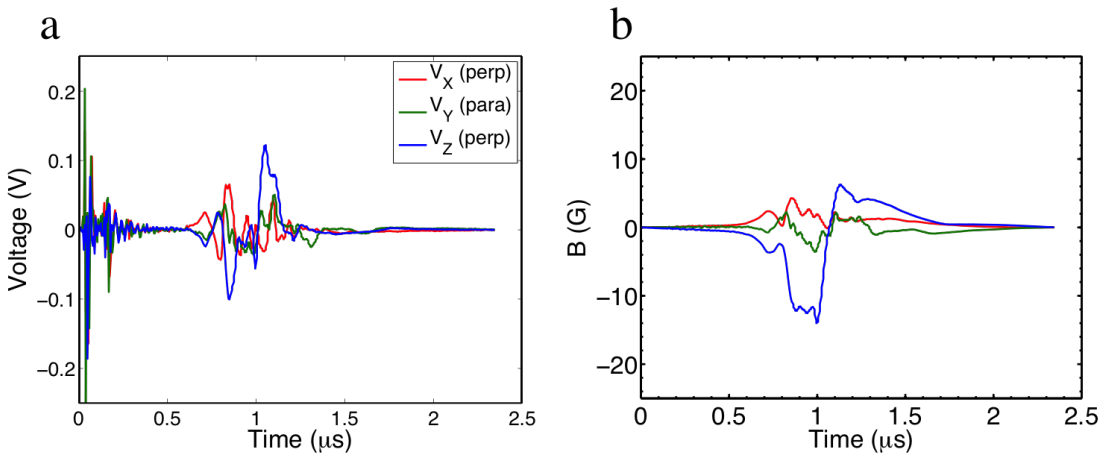

Figure 27: **Analysis of Bdot probe data.** **a,** The raw voltage signal shows high-frequency noise within the first 300 ns associated with both the laser being fired and fast electrons. The magnetic field associated with the Biermann Battery mechanism arrives at 700 ns and is substantially larger and longer-lived. A fast Fourier transform is applied to the raw voltage data along with integration according to Faraday's law. The integrated data **b,** represents the Biermann battery magnetic field, in this case, at a location 3 cm from the target.

we measure the arrival of the laser as a sharp noise peak at $t = 0$. Furthermore, when the probe is placed along the flow direction, fast electrons can generate high-frequency noise and their own transient magnetic field. Since we are not interested in the fast electron contribution or noise, the probes are placed far enough from the target to separate these signals. By the time the shock wave or jet arrives, $\sim 1\mu$s after the drive laser, the laser noise has damped out and the fast electrons have passed. So the background signal drops back down to its nominal value as seen in Figure 27, and the high-frequency noise can be reduced during the analysis process.

Instead of integrating the measured voltage by Equation 95, a fast Fourier transform is performed on the induced voltage. The data is integrated in frequency space, and then an inverse fast Fourier transform is performed on the analysed data. In total, the

following 8 steps are performed: (1) A nominal background subtraction is taken off the raw induced voltage $V_{meas}(t)$. By sampling the last 30 ns of data, assuming the voltage returns to its nominal background level at the end of the oscilloscope trace, an averaged background value can be determined. The averaged background is typically $0.1 - 0.5\%$ of the maximum voltage. (2) As a rule, we can determine the arrival of the laser pulse by looking at the dummy channel. On every experiment, we have noticed that the dummy channel does not measure a Biermann battery field and all induced voltage is within the average background level (a few mV). This is what we would expect since the dummy channel only consists of twin-twisted wires that terminate at the base of the cube and does not include a loop of wire to detect transient magnetic fields. We use this channel to keep an eye on the electrostatic noise and check that there isn't, for example, a low-level ringing in the system that could affect the magnetic field measurement. The low-level signal of the dummy channel is subtracted from the data (for completeness) but in reality has almost no effect on the overall results which means the construction of the twin-twisted probe wires efficiently reduces electrostatic noise that could be otherwise induced in the wires.

After all of the background subtractions have been made, the $V_{meas}(t)$ is analysed. We would like to apply a Matlab fast Fourier transform and (3) rotate the data by a half-cycle to move the high-frequency noise into the middle of our trace, resulting in $V_{rot}(t)$. (4) Matlab's operation Y=fft(X) and X=ifft(Y) is defined for functions X and Y of length n as follows [68]:

$$Y(k) = \sum_{j=1}^{n} X(j) W_n^{(j-1)(k-1)} \tag{96}$$

$$X(j) = \frac{1}{n} \sum_{k=1}^{n} Y(k) W_n^{-(j-1)(k-1)} \tag{97}$$

where $W_n = e^{(-2\pi i)/n}$ is one of n roots of unity. $V_{rot}(t)$ undergoes this fast Fourier transform to produce $V_{rot}(\omega)$. (5) Another half-cycle rotation is performed on the data to return it to the original order. (6) Using Equation 92, $B(\omega)$ can be determined in frequency space.

The values of a and τ_s are shown in Figure 26 and similar for all 1 mm Bdot probes. (7) The analysed data $B(\omega)$ undergoes another half-cycle rotation, and (8) an inverse fast Fourier transform is performed to returned the data to real space, $B(t)$. (9) After one last half-cycle rotation to return the data to the original order, with the first point at $t = 0$, the Bdot analysis procedure is complete.

As a sanity check, both this method and straight integration are performed, separately, to ensure that the two calculations are relatively similar. On average, the difference in magnetic field amplitude is $< 10\%$ when comparing these two methods– this is ideal. When the Fourier transform method is not used, straight integration often results in magnetic fields that do not return to $B = 0$ after long times. This could imply that the differential amplifier is not working correctly. However, before an experiment, all the equipment, including the differential amplifier, is checked by placing the probe in a known magnetic field, supplied by a Helmholtz coil. Using the exact same setup as the experiment (including cables, etc.), each probe is recalibrated to ensure proper measurements. This means that the entire setup, including the probe, cables, flange connection, and differential amplifiers, are all working correctly. So if the probe signal terminates at some nonzero value in an experiment, then this is physically incorrect for late times when the shock has fully passed through the probe loops. To resolve this issue, the application of a Fourier transform ensures that the data returns to zero and therefore makes physical sense. In our experiments, the average speed of a laser-produced shock wave is 20 km/s and passes through a 1 mm diameter Bdot coil, taking 50 ns to pass. Therefore, the induced magnetic field represents the average magnetic field over a 1 mm^3 region within a span of 50 ns.

Lastly, what effect does the Bdot probe tip have on the plasma flow? One reasonable concern could be that the probe tip, though successful in protecting the coils inside, disturbs the plasma flow and associated magnetic fields. Ideally we would like a diagnostic that is invisible to the plasma, but every diagnostic has its own disadvantage. In the Vulcan experiments, the Rm was low ($\sim 2 - 5$) so magnetic field diffusion was dominant. Using

the diffusion equation, we can estimate an upper limit to magnetic diffusion:

$$\frac{\Delta B}{t} \sim D\frac{1}{L^2}B \Longrightarrow \frac{\Delta B}{B} = D\frac{1}{vL} \tag{98}$$

where $D = \frac{\eta c^2}{4\pi}$, v is the plasma velocity, and L is the Bdot coil diameter. The magnetic field disturbance due to the probe tip is $\sim 30\%$ and can provide error bars for our data. Physically, as the magnetic fields pass by the probe tip, most are diffused through the Macor shielding and induce the voltage we measure. For turbulent dynamo experiments on the NIF where diffusion is negligible, other magnetic field diagnostics will be used to characterise the fields.

Chapter 4

Magnetic Field Amplification of Laser-Produced Shock Waves

X-ray [69][70][71] and radio [72][73][74] observations of the supernova remnant Cassiopeia A reveal the presence of magnetic fields about 100 times stronger than those in the surrounding interstellar medium. Field coincident with the outer shock probably arises through a nonlinear feedback process involving cosmic rays [71][75][76]. The origin of the large magnetic field in the interior of the remnant is less clear but it is presumably stretched and amplified by turbulent motions. Turbulence may be generated by hydrodynamic instabilities at the contact discontinuity between the supernova ejecta and the circumstellar gas [77]. However, optical observations of Cassiopeia A indicate that the ejecta are interacting with a highly inhomogeneous, dense circumstellar cloud bank formed before the supernova explosion [78][79][80]. Here we investigate the possibility that turbulent amplification is induced when the outer shock overtakes dense clumps in the ambient medium [81][82][83]. We report laboratory experiments that indicate the magnetic field is amplified when the shock interacts with a plastic grid. We show that our experimental results can explain the observed synchrotron emission in the interior of the remnant. The experiment also provides a laboratory example of magnetic field amplification by turbulence in plasmas, a physical process thought to occur in many astrophysical phenomena.

4.1 Astrophysical Motivation– Supernova Remnant Cassiopeia A

High-resolution X-ray images and radio polarization maps of Cassiopeia A show two distinct strong magnetic field regions [72][73][70][80]. Narrow X-ray filaments, a fraction of a parsec in width, are observed at the outer shock rim at a radius of about 2.5 pc. These structures are produced by synchrotron radiation from ultrarelativistic electrons (with teraelectronvolt energy) and can be explained by magnetic fields of the order of 100 G or more [71][70]. The interior of the remnant contains a disordered shell (about 0.5 pc in width at a radius of 1.7 pc) of radio synchrotron emission by gigaelectronvolt electrons [73]. The inferred magnetic field in these radio knots is a few milligauss, about 100 times higher than expected from the standard shock compression of the interstellar medium [83].

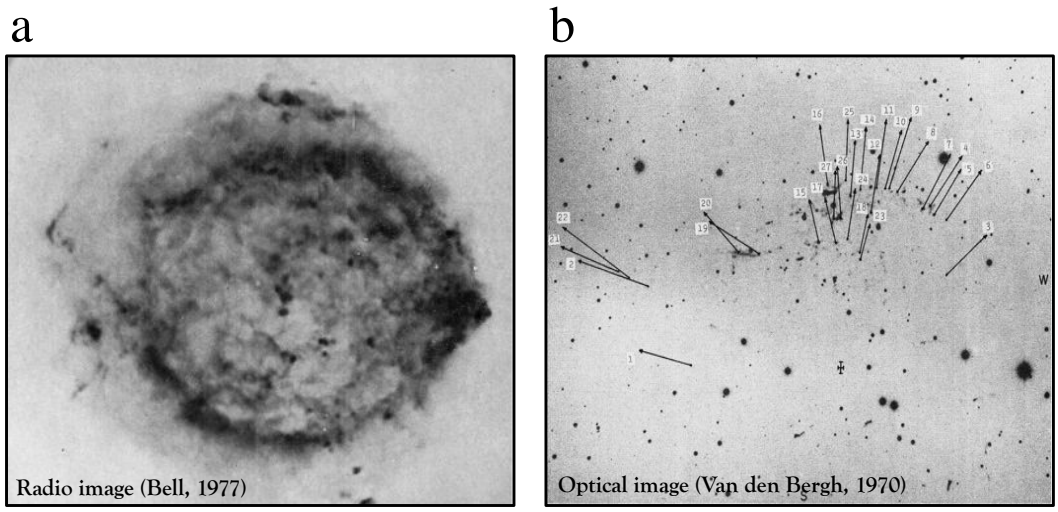

Figure 28: **Astrophysical observations of supernova remnant Cassiopeia A. a,** Radio image of the remnant shows clumpy material in the interior of the supernova, indicating a turbulent environment that can amplify seed magnetic fields. **b,** Optical image of the remnant shows the existence of dense cloud banks that are thought to generate turbulence in the outward supernova remnant flow.

Optical observations of Cassiopeia A show the presence of both rapidly moving (5,000 - 9,000 km/s) and essentially stationary dense knots. Although the moving knots themselves have a high velocity, their overall pattern is nearly stationary [78]. This led to the suggestion [78] that a dense pre-existing inhomogeneous stationary cloud bank could be present. New rapidly moving knots predominantly appear at a position broadly coincident with the shell of bright radio emission [74]. Sizes of the observed small-scale features within the shell range from 0.01 to 0.1 pc arranged in larger patterns extending to 0.52 pc [84]. Interaction between the ejecta and the cloud bank may excite turbulence that amplifies the magnetic field and makes Cassiopeia A an exceptionally bright radio source [73]. The interaction is akin to the Rayleigh Taylor instability otherwise proposed as a source of turbulence and magnetic field at the contact discontinuity between the ejecta and the swept-up ambient medium [77] except that the interaction begins with an already disturbed density configuration.

4.2 Background and Previous Work

The standard model for the origin of galactic and intergalactic magnetic fields is through the amplification of seed fields by means of turbulent processes or dynamo to the level consistent with current observations [4][5][6]. There are a number of mechanisms that can generate seed fields, including the Biermann battery process. Currents generated from misaligned density and temperature gradients accompany the formation of galaxies in the absence of a primordial field. Driven by the geometrical asymmetries in shocks associated with the collapse of protogalactic structures [1], the Biermann battery mechanism can generate tiny seed 'primordial' fields to a level of $\sim 10^{-21}$ G [85][31]. With the advent of high-power lasers, scaled astrophysical objects can be created in the laboratory due to the invariance of MHD equations [9][8].

Previous work conducted on the generation of seed fields [86] was performed at the

Laboratoire pour l'Utilisation de Lasers Intenses (LULI 2000) laser facility. The team characterised the first observations of tiny seed fields $\sim 10^{-21}$ G in the laboratory, led by Professor Gianluca Gregori. A 500 μm carbon rod target was ablated with 350 J of frequency-doubled green (527 nm) light in a 1.5 ns pulse with a 400 μm focus. The chamber was filled with helium gas at a pressure of $0.8 - 1.6$ mbar. After ablation of the target, the heated solid matter initially underwent a ballistic expansion until the shocked mass was roughly equal to the ejected mass, and then the shock transitioned to a Sedov-Taylor blast wave [87][88] at a distance <10 mm from the target. Optical diagnostics measured $n_e = 5 \times 10^{15}$ cm^{-3} and $T_e = 2$ eV. For a Bdot probe located $r = 3$ cm from the target, the peak magnetic field arrived at 1 μs and is defined as the characteristic timescale. The characteristic length scale of the system is approximately $2r/\kappa = 18.8$ cm where $\kappa \sim 0.1 - 0.3$ is the tangential gradient scale coefficient determined from 2D MHD simulations and consistent with protogalactic halos [85]. The Bdot probes measured a $10 - 30$ G field orthogonal to the flow direction that is indicative of the Biermann battery mechanism.

The laboratory plasma was scaled to the intergalactic medium (IGM) to indicate that curved intergalactic shocks in protogalactic structures, with changing curvature at the level of a few tens of a percent on scales of about one megaparsec, can generate magnetic fields with values of around 10^{-21} G. According to the G. Gregori *et al.* publication, they reported Re $= 7.9 \times 10^3$ and Rm $= 16.5$ for their laboratory plasma. This meant that a 18.8 cm plasma was similar to the IGM that expands over 1 Mpc– an astrophysical environment more than 10^{24} cm long. Furthermore, this plasma fully evolved over 1 μs compared to 0.7 Gyr (or $10^{22}\mu$s). This is the type of environment we want to create in the laboratory– a small scale version of an astrophysical event that can evolve on fast timescales. This experiment laid the foundation for the Vulcan experiments in this thesis.

4.3 Experimental Arrangements

Our experiments focused on magnetic field amplification in a clumpy medium by making in situ magnetic field measurements in the turbulent wake of a laser-produced shock. To generate seed magnetic fields via the Biermann battery mechanism, an asymmetrical shock wave was driven using the Vulcan Target Area West laser facility. A 500 μm diameter carbon rod target was ablated in a 1 mbar ambient gas-filled chamber, launching a Sedov-Taylor shock wave analogous to nearby supernova remnants. The interaction of a shock with large density perturbations was reproduced in the laboratory by passing a laser-produced shock through a plastic mesh with $l = 1.1$ mm grid cell size, and 0.4 mm-thick wires. In situ magnetic field measurements were made in the turbulent wake of the shock, and a range of diagnostics were used to characterise the plasma conditions for a hydrodynamic scaling [9][8].

Three beams were angled into the Vulcan Target Area West chamber with two beams at 15° above the target horizon, separated by 5°, and one beam 15° below the target horizon. All three beams were focused onto the carbon rod with a spot size of 300 μm onto a 500 μm diameter target as shown in Figure 29. Each beam was carefully aligned and focused onto the upper half of the carbon rod stalk with an accuracy of ~ 30 μm. During the day, the beam alignment can change due to the laser bay alignment. To ensure the lasers were hitting the target correctly, we checked the pointing and focus for each shot by observing very low intensity light on the target with a camera. We did not use phase plates on this experiment to allow for a tighter, more accurate focus. The laser energies were not identical for all three beams– they ranged from $50-150$ J per beam, but the total energy of all three beams was 300 ± 30 J. The corresponding laser intensity was $I_L = 4 \times 10^{14}$ W·cm^{-2}. The lower beam consistently delivered the least amount of energy. Before entering the target chamber, each beam was frequency-doubled to 527 nm of green light and then delivered with a 1 ns square pulse.

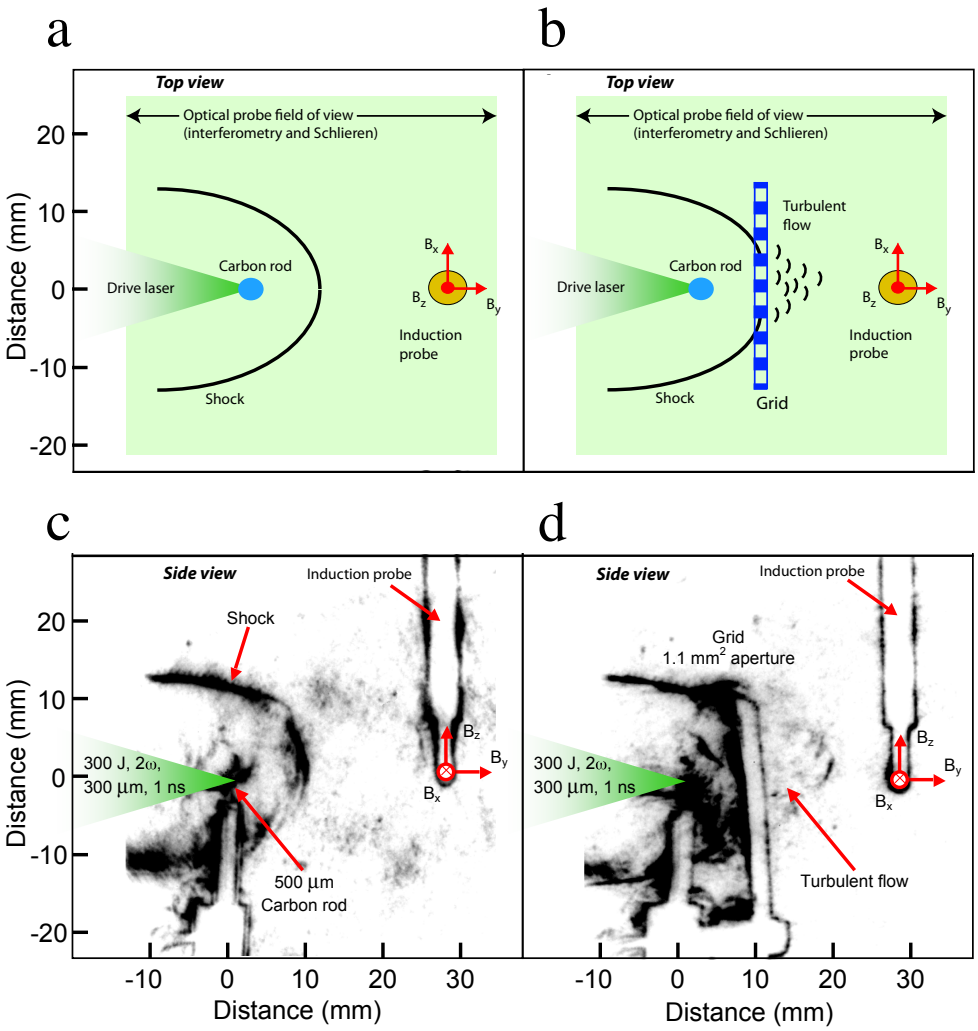

Figure 29: **Vulcan experimental setup to study magnetic field generation and amplification.** **a,** Drive beams focus onto a 500 μm carbon rod target in a 1 mbar argon gas-filled chamber. The plasma was characterised by optical diagnostics with a 8 cm diameter field of view. Bdot probes [86][63] were placed along the target horizon plane and could be adjusted to various distances along the plasma flow to characterise the magnetic fields. **b,** A 1.1 mm^2 aperture plastic non-conducting grid was placed 1 cm from the target to disturb the plasma flow and generate turbulence. **c,** Schlieren data of the resultant shock wave and **d,** turbulent flow indicates the location of density gradients.

The target chamber was filled with an ambient argon gas at $P = 1.0 \pm 0.2$ mbar. The carbon rod position was designated as target chamber centre and each graphite rod had a density of 2.267 g·cm^{-3}. The rods were minimally glued onto glass stalks which were mounted onto large plastic mounts. A 3×3 cm plastic mesh grid with $l = 1.1$ mm openings and 0.4 mm-thick wires was placed 1 cm from the target, allowing a fully-developed Sedov-Taylor shock wave to form before encountering the grid barrier.

To diagnose the plasma characteristics for an astrophysical scaling, we used optical diagnostics: (1) schlieren, (2) interferometry, and (3) spectroscopy. A tabletop YAG laser with a 532 nm wavelength and 5 ns gate width was used to probe the plasma. By expanding the beam diameter to 8 cm, a large field of view was attained of the experimental setup. The YAG beam spatial profile was not perfectly smooth, so an image of the background signal was taken before each shot. During the analysis procedure, this background signal was subtracted from the data. The probe beam was split to allow for schlieren and interferometry along the same path using large 10 inch optics. The schlieren diagnostic was used to measure density gradients and produced an image of the shock location. A 500 μm knife edge was used to block collimated rays, while refracted rays were collected with doublet optics and focused onto Princeton PI-MAX CCD cameras. A Mach-Zehnder interferometer was used to measure the density profile and used similar optical and camera equipment.

Spatially resolved spectroscopy was collected by a separate optical setup that was not exactly along the path of schlieren and interferometry. Though the collection optic for spectroscopy was at an angle $< 20°$ from normal and the field of view was 6 cm, the setup imaged a relatively similar plasma cross-section to make a comparison between data from all three diagnostics. A 1,200 grooves/mm grating was used with a dispersion of 0.0316 nm/pxl, centered at ~ 450 nm. A tungsten lamp, positioned at the target chamber centre, was used during the setup to measure the efficiency of the optical setup. Comparing the known white light response of the tungsten lamp to the measured response at the camera

(after passing through the entire optical setup), corrections could later be made to the data to improve the accuracy of spectral line ratios corresponding to electron temperature.

To diagnose the magnetic fields generated in the expanding plasma, a $\sim 1 \times 1$ mm^2 Bdot probe was placed along the path of the expanding plasma at various distances from the target. By positioning the tip $1-6$ cm from the target, a full magnetic field characterisation was performed for shock waves in argon gas at 1 mbar. Specifically we used probe #6 with cable #4.

4.4 Plasma Characterisation of Laser-produced Shock Waves

Without the presence of a non-conducting grid, the shock wave position (r_s) and properties have been monitored at various times using Schlieren, interferometry, and spectroscopy diagnostics. The shock closely follows a Sedov-Taylor solution [22] with $r_s \propto t^{2/5}$. Numerical simulations performed for 1D-spherical geometry with the collisional-radiative hydrodynamic code HELIOS, and for 2D-cylindrical geometry with the magnetohydrodynamic code FLASH reproduce the shock position, peak electron density and temperature values.

At the position of the grid ($r_{s0} = 1$ cm), the flow velocity of the shock is measured to be $v_0 \sim 2 \times 10^6$ cm·s^{-1} (Mach number ~ 9), although this increases on interaction with the grid. The Reynolds number corresponding to this shock radius is $\mathrm{Re} = v_0 r_{s0}/v \sim 5 \times 10^4$ ($\nu \approx 40$ cm^{2}s^{-1} is the plasma viscosity), and the magnetic Reynolds number is $\mathrm{Rm} = v_0 r_{s0}/\eta \sim 3 - 6$ with magnetic diffusivity $\eta \approx 4 \times 10^5$ cm^{2}s^{-1}. As shown in earlier hydrodynamic simulations [89] and in FLASH magnetohydrodynamic simulations of the experiment, for large Re, the grid acts as a channel, which accelerates the flow as it passes through the pores, after which the flow velocity decreases. This can be seen in Figure 29 where, with the grid, the turbulent flow appears to advance more rapidly towards the

position of the magnetic field diagnostics. From Schlieren imaging, for all experiments with the grid, the shock is observed to arrive at the position of the probe around $t \geq 1.5\mu$s. The error bars of each data point in Figure 30 were determined by shot-to-shot variations of identical experimental arrangements. All of the 2-5 repeats for each data point fall within the error bars shown.

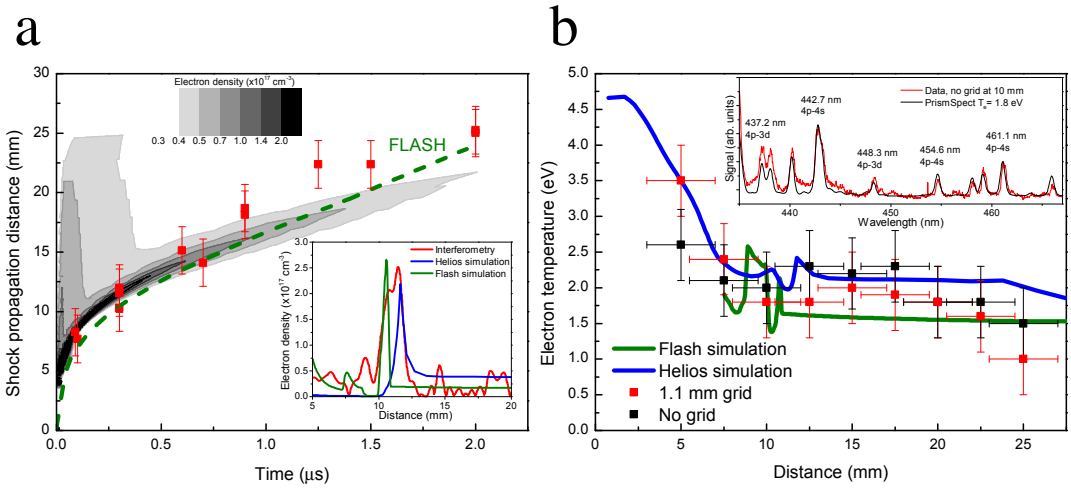

Figure 30: **Characterisation of the shocked plasma. a,** Measurement of the shock wave position versus time in the absence of a grid obtained from Schlieren data (red squares), 1D HELIOS simulations (contours) and 2D FLASH simulations (dashed green line). The inset shows the measured density profile obtained through interferometry at $t = 300$ ns compared with simulation predictions. The estimated maximum error of 2 mm in the experimental position is due to the uncertainty in the optical images to define the exact location of the shock front. **b,** The panel shows the measured electron temperature (T_e) profiles at $t = 300$ ns without (black symbols) and with (red symbols) a grid obstacle in the flow. The experimental temperature values are compared with HELIOS and FLASH simulations. The low value of T_e near the target in the FLASH simulation is an artefact due to expansion of the cold carbon material; we therefore omit this part of the T_e profile in the graph. The inset shows the measured spectral lines at 1 cm from the carbon rod position (averaged over 0.2 cm). The ratio of the emission lines has been fitted with the collisional-radiative code PrismSPECT. [90]

4.4.1 Description of Helios and FLASH Simulations

We have performed 2D-cylindrical MHD simulations using FLASH [91][92][93][94], a publicly available, modular, multi-physics, finite-volume, shock-capturing code. In order to model the full range of physical processes involved in the experiments, our simulations include the unsplit staggered mesh MHD solver [95], extended to three temperatures and cylindrical geometry [91][93], explicit Spitzer resistivity, implicit thermal conduction and heat exchange, as well as multigroup radiation diffusion with multi-material tabulated opacities and equations of state. The drive is accurately modelled using a laser ray-trace package, whereas the Biermann battery source is added to the MHD equations [96].

We initialise a circular target ($R = 250$ μm) of Carbon in the origin of a $[0, 2cm] \times [-1, 3cm]$ cylindrical $(r - z)$ computational domain, which is filled with argon gas at 1 mbar. The target is illuminated by a 300 J laser pulse for 1 ns, with a spot size of 300 μm. We have used the measured shock position at different times for a range of different laser energies to calibrate the fraction of the laser energy that is deposited in the target. We find that a fraction 37% is consistent with all of the measured shock positions within uncertainties, and we therefore use this fraction in our simulations.

We utilise 6 levels of refinement and blocks of 16×16 cells, obtaining an equivalent resolution of ~ 40 μm per cell. The reconstruction is carried out with a Piecewise Linear Method (PLM), employing a minmod limiter; the Godunov fluxes are recovered with an HLLC (Harten, Lax & van Leer-Contact) Riemann solver [97]. Free outflow boundary conditions are used except for the z-axis where axial symmetry is enforced. We performed two simulations of the described setup and followed their evolution for 3 μs. In one of the two runs, we introduced a grid at 1 cm from the target and perpendicular to the path of the flow, the aperture specifications of which conformed to the grid used in the experiment.

We have also performed 1D-spherical radiation-hydrodynamic simulations using the HELIOS code. HELIOS-CR is a user-oriented 1D radiation-magnetohydrodynamics code

to simulate the dynamic evolution of laser-produced plasmas. It includes an in-line collisional radiative (CR) model for computing non-LTE atomic level populations at each time step of the hydrodynamics simulation. We calibrated the HELIOS simulations using the position of the shock as a function of time measured in the experiment and predicted by the 2D-cylindrical FLASH simulations. This required taking the mass of ablated carbon to be ~ 40 ng, assuming a fraction 37% of the 300 J laser pulse is deposited in the carbon rod target.

4.5 Magnetic Field Characterisation of Shock-induced Turbulence

Wind tunnel experiments [98] with a steady flow have shown that homogeneous turbulence is already well developed at distances $d \sim 20l$, motivating us to take our field measurements predominantly at a distance of 2 cm downstream of the grid. Figure 31 shows that in the case of a grid, the perpendicular component ($B_\perp^2 = B_x^2 + B_z^2$) of the magnetic field is $2-3$ times larger than without it. Previous results [86] have indicated that perpendicular magnetic fields are produced at the shock front through the Biermann battery mechanism [99] owing to misaligned temperature and density gradients.

We find that for shocks passing through a grid, magnetic field amplification continues to occur long after the shock has passed, suggesting that an alternative mechanism is at play. This is attributed to the fact that the downstream flow is highly turbulent as a result of the shock-grid interaction. Figure 31 also shows that the measured signal starts earlier in the case with a grid than in the case without a grid for two reasons. First, the shock is accelerated as it passes through the grid, owing to the Bernoulli effect, whereas in the case without a grid, it is not. Second, the grid shadows the gas beyond it from the high-temperature radiation emitted at early times. Thus, in the case with a grid a significant

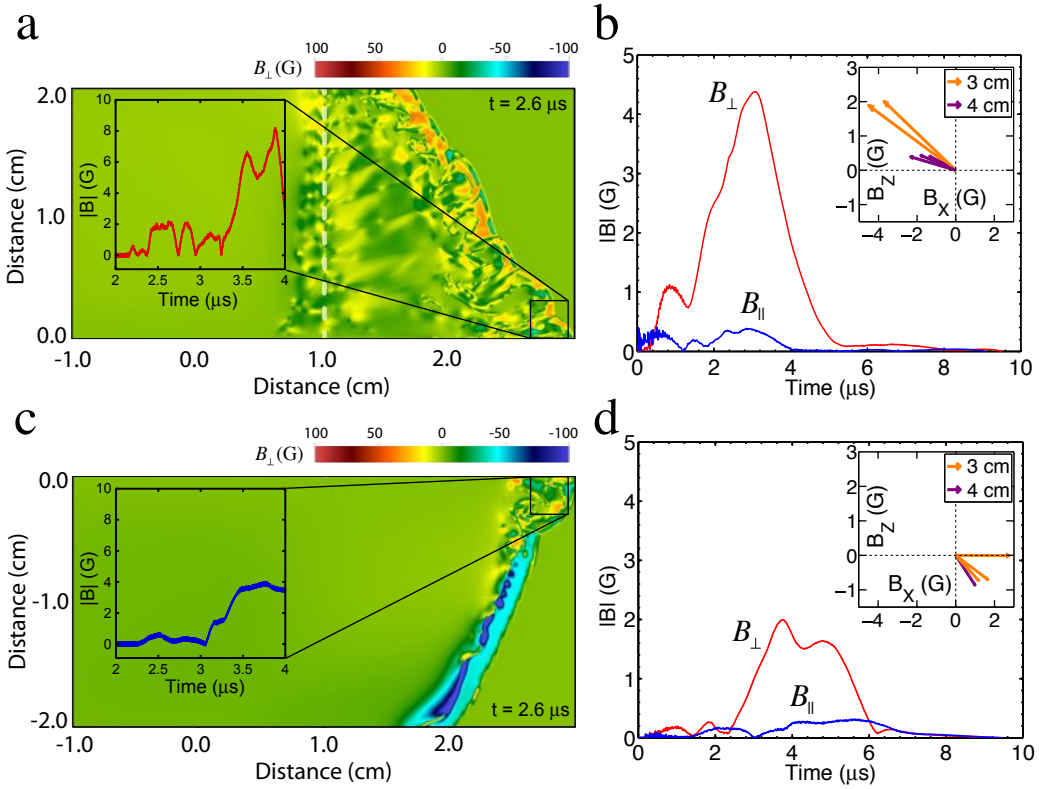

Figure 31: **Time evolution of the magnetic field. a,** FLASH simulation of the shock propagation through a grid at $t = 2.6$ μs. The inset shows the time variation of the magnetic field at 2.8 cm from the grid position along the symmetry axis (averaged over a 3 mm $\times$ 3 mm space). **b,** The same as in **a,** but with no grid. **c,** The magnetic field measured at 3 cm from the carbon rod with components along the axis. The time resolution is 10 ns. The magnetic field has been extracted from the coil voltage by using a fast Fourier transform technique [63]. We estimate error in the magnetic field traces to be $\pm$0.3 G based on shot-to-shot fluctuation as shown in the insets. Initial ($t < 100$ ns) high-frequency noise due to the laser-plasma interaction with the carbon rod has been filtered out in the extraction of the magnetic field. The inset shows the projection of the magnetic field onto the x-z plane at the time of its maximum intensity. Each vector corresponds to different shots. Data obtained at a distance of 4 cm from the carbon rod are also shown in the inset. In this case, the field magnitude is considerably reduced. **d,** The same as in **c** but without the grid, as illustrated in Figure 29.

fraction of the gas beyond the grid is not heated, and so has a higher diffusivity. This effect is visible in the measured temperature profiles of Figure 30.

Simulations suggest that the observed field amplification does not depend on the Biermann battery generation at the laser spot, we have run FLASH simulations with the latter process turned on only during the first 30 ns and switched off afterwards (Figure 32). This shows that the measured magnetic field is indeed enhanced as the shock passes through the grid owing, mainly, to the induced turbulence. Assuming a downstream flow velocity of the order $10^5 - 10^6$ cm·s^{-1}, the field is gradually amplified over a distance of ≤ 1 cm from the grid, before arriving at the probe, further supporting the mechanism of turbulent field amplification occurring by differential rotation induced by the mesh.

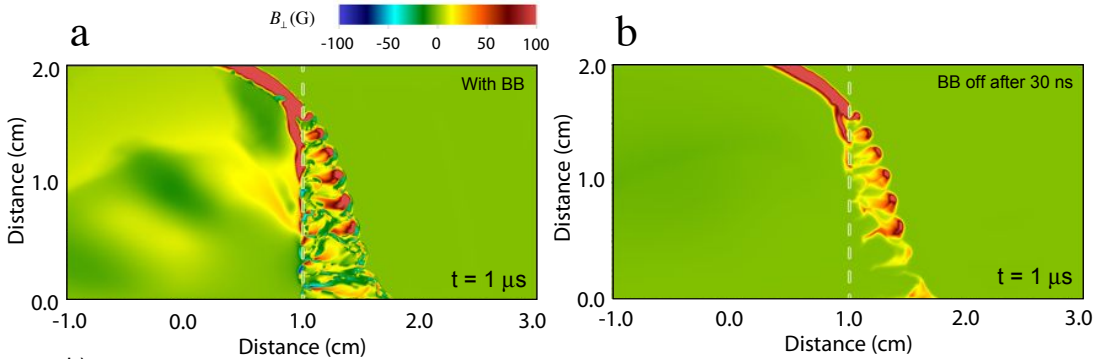

Figure 32: **Effect of the baroclinic source term. a,** FLASH simulations of the shock propagation through a grid at $t = 1$ μs with the Biermann battery (BB) term included. **b,** Same as **a** but with the Biermann battery term omitted except for the first 30 ns. The simulations show that magnetic fields of the order of a megagauss are produced in the plasma ablated from the target by the laser, and these magnetic fields are advected outward with the vaporised carbon rod material that drives the shock into the gas. However, the advected magnetic fields are diluted by expansion of the vaporised carbon target material and their strength is further reduced by the resistivity in the vapour, since Rm is small. The simulations also show the magnetic fields are much larger in the presence of the grid, and they develop over a large distance, supporting our conclusion that the grid plays a significant role in amplifying the magnetic fields.

4.5.1 Development of Kolmogorov Turbulence

The vorticity induced as the shock overtakes the grid acts as a seed for turbulent generation of magnetic field on a smaller scale. Beyond the grid, the vorticity is stretched in the direction of the flow, so that the spatial scale of the largest eddies is $L_e \sim 7$ by the time the shock reaches the induction probe (Figure 33). Since the magnetic Prandtl number, $\mathrm{Pm} = \mathrm{Rm}/\mathrm{Re} = v/\nu \approx 10^{-4}$, is substantially lower than in the SNR case, the resistive scale lies well above the viscous scale and in fact above the energy-containing scale at which the inertial range starts. Resistive diffusion of the magnetic field is increasingly important on smaller scales, although our measured increase in the magnetic field shows that it is not dominant at the scales of interest.

The measured k-spectrum of the magnetic field is consistent with the Golitsyn ($k^{-11/3}$) power-law dependence [11][49], characteristic of magnetic fluctuations at low Pm [11][100][101]. This suggests that turbulent motions are present and amplifying the field at subresistive scales. With a small magnetic Reynolds number, the amplification is due to the stochastic tangling of an imposed field, B_0, by turbulent motions, and the saturated level is set by balancing this effect with Ohmic diffusion [11][100][101]. In our experiment, B_0 is the Biermann-battery generated baroclinic magnetic field in the homogeneous flow. The amplified field scales as $|\delta B| \sim \mathrm{Rm}|B_0|$, and it remains dynamically unimportant because the Alfvén speed is smaller than the flow velocity ($v_A \sim 400 - 1400$ cm·s^{-1}). In Figure 31, we can see this moderate amplification of the small seed magnetic field as theoretically and physically discussed in Section 2.5.2.

FLASH simulations without a grid show that the shock becomes unstable when it is overtaken by the compositional discontinuity between the vaporised carbon target material and the gas, generating vorticity, and therefore magnetic fields, at spatial scales ≤ 3 mm. This is the origin of the k-spectrum of the magnetic field without a grid. Simulations with a grid present show that the size of the largest eddies is ~ 2 times larger, the flow velocity

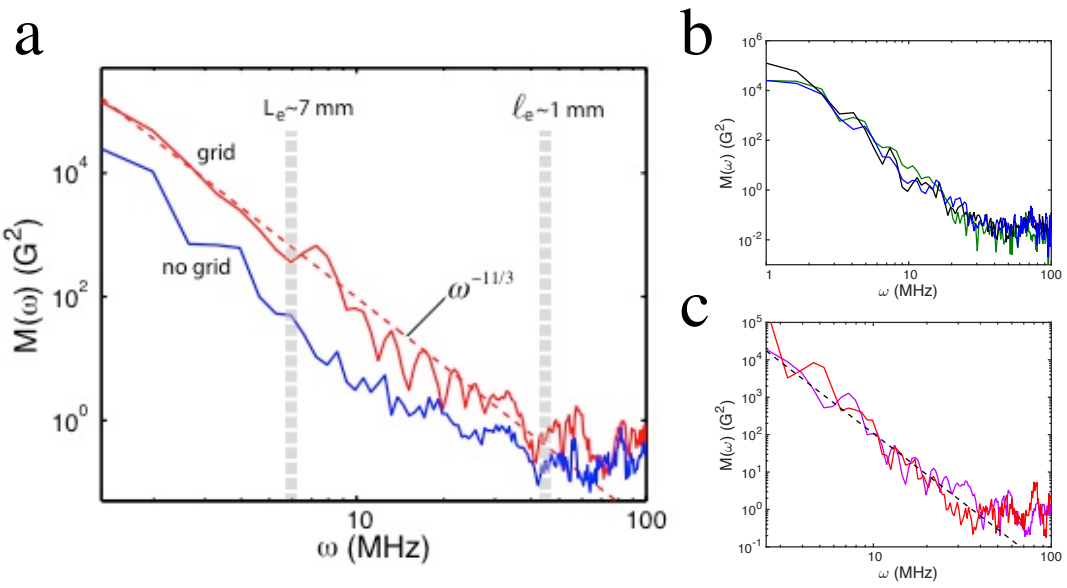

Figure 33: **Frequency spectrum of the magnetic field traces from Figure 31. a,** Plot of the measured magnetic energy spectrum $M(\omega) = |B(\omega)|^2$, where $B(\omega)$ is the fast Fourier transform of the total magnetic field for both the cases with (solid red line) and without (solid blue line) a grid. $M(\omega)$ is obtained by averaging all of the available laser shots with the induction coils placed at 3 cm from the carbon rod position. If we take the flow velocity as $v_0 \sim 7 \times 10^5$ cm·s^{-1} at the induction coil position, according to FLASH simulations with the presence of the grid, the corresponding spatial scales are indicated in the plot. L_e is the inferred energy-containing scale, that is, the scale of the largest eddies, and l_e is the induction coil size, which determines the resolution limit. The measured spectrum shows a power law $\omega^{-11/3}$ (dashed red line). As the mean flow velocity is larger than the (subsonic) velocity fluctuations excited by the grid, then, according to Taylor's hypothesis, we obtain $\omega \sim v_0 k$, where k is the wavenumber of the magnetic fluctuations. As a result of the proportionality relation between frequency and wavenumber, the magnetic energy spectrum thus exhibits the expected Golitsyn ($k^{-11/3}$) power-law dependence. **b,** Shot-to-shot comparison of the three identical shot configurations measuring the magnetic field from a shock wave at 3 cm from TCC with a probe. All three power spectrums are in good agreement and provide insight into the reproducibility of probe measurements. Figure 31 provides quantitative information regarding error analysis of B(t). **c** Same as **b** but for the laser-produced shock waves disturbed by a grid located at 1 cm from TCC. [11][100][101]

is $\sim$ 50% larger, and thus the magnetic Reynolds number is $\sim$ 3 times larger. This is consistent with the higher magnetic field seen in the experimental data.

4.5.2 Cross Correlation and Growth Rate

Figure 31 shows that amplification occurs over distances much larger than the aperture of the grid and further discussion of this amplification mechanism (both experimental and theoretical) can be found in Sections 4.5.1 and 2.5.2. The slope of the normalised twopoint cross-correlation function of the measured magnetic field at $d = 2$ cm and $d = 3$ cm from the grid position (Figure 34) shows an amplification rate $\gamma = 4 \times 10^5$ s^{-1}. This rate at the outer scale must be comparable to the Ohmic dissipation rate. Estimating this scale to be $\sim L_e = 7$ mm, we measure $\nu/L_e^2 \approx \gamma$. This timescale gives a good order-of-magnitude estimate of the effective stretching rate of the chaotic flow behind the grid and therefore of the typical minimal rate of magnetic field amplification one should expect in an astrophysical plasma, where resistivity is low and Rm is large.

To attain values of the magnetic field at different distances, a single Bdot probe was mounted onto a translation stage, as shown in Figure 29, and allowed for measurements of the magnetic field distances of 2 cm and 3 cm from TCC. The probe was placed at 2 cm for one shot and at 3 cm for the another identical shot. The assumption here is that the laser conditions, target alignment, and gas pressure were identical in both shots to produce the same plasma conditions and therefore a cross correlation. On the experimental side, the exact same procedures were executed to reproduce the same plasma conditions, but it is worth noting that the ideal situation would be to have measurements from the exact same shot at different positions. This was not possible because the data indicates that the Bdot probe disrupts the plasma flow. If we set up a probe at 2 cm and a probe at 3 cm, the plasma flow (and magnetic field signal) at the 3 cm probe location would be highly disturbed by the 2 cm probe. The best solution was to repeat the shot within the best of

our ability to recreate the same conditions and measure the field at different distances. In terms of quantitative error analysis, the resultant shock wave position varied on any given shot by ±4 mm and the peak of the magnetic field measurements varied by ±0.3 G (due to laser energy, pointing, gas pressure, etc.).

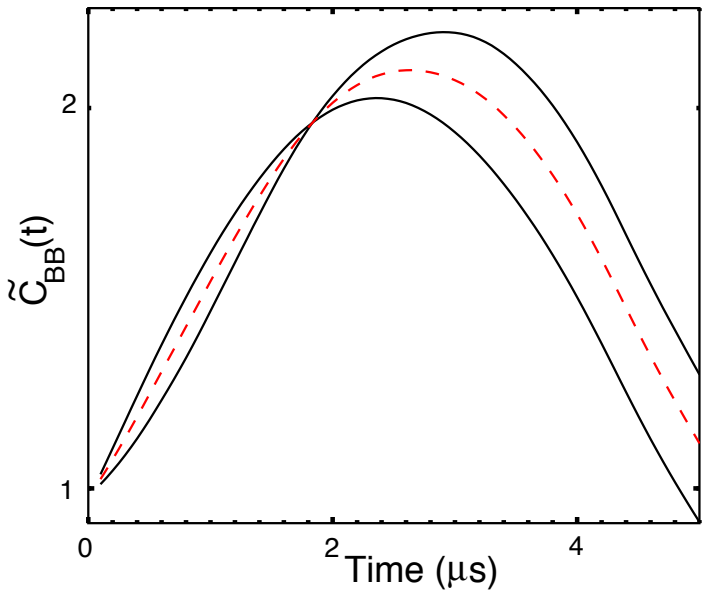

Figure 34: **Cross correlation analysis.** Plots of the normalised two-point cross correlation function, $\sim C_{BB}(\mathrm{t})$, of the measured magnetic field at d = 2 cm and d = 3 cm from the grid position. The solid black lines correspond to two different pairs of laser shots. The dashed red line is the average of $\sim C_{BB}(\mathrm{t})$ for the two pairs of shots. The slope of the two-point cross correlation function shows an amplification rate $\gamma = 4 \times 10^5$ s^{-1}.

The cross correlation and growth rate is calculated in the following way. Consider the magnetic field measured at two different points in space. Let $B_1(t) = (B_{x1}^2 + B_{y1}^2 + B_{z1}^2)^{1/2}$ be the field at 3 cm, and $B_2(t) = (B_{x2}^2 + B_{y2}^2 + B_{z2}^2)^{1/2}$ the field at 4 cm from the carbon rod position. We define the cross correlation function between these two points as:

$$C_{BB}(t) = \frac{1}{T_2 - T_1} \int_{T_1}^{T_2} B_1(u) B_2(t+u) du, \tag{99}$$

where T_1 and T_2 are the initial and final sampling times, respectively. In our case $T_1 = 2$ μs and $T_2 = 7$ μs. The evolution of the magnetic field, $B(t)$, can be formally described by [102]

$$\frac{d\mathbf{B}}{dt} = \frac{\partial \mathbf{B}}{\partial t} + \mathbf{v} \cdot \nabla \mathbf{B} = \mathbf{B} \cdot \nabla \mathbf{v} + \eta \nabla^{\mathbf{2}} \mathbf{B} \tag{100}$$

where we have assumed an incompressible fluid. The first term on the right side of the equation describes the growth of magnetic fields due to stretching and twisting of the field lines, and this operates, on a spatial scale l, with a characteristic rate v/l. The second term in this equation represents the resistive dissipation, with a characteristic decay rate given by η/l^2. Equation 100 can be rewritten in the scalar form as

$$\frac{dB}{dt} = \gamma B, \tag{101}$$

where γ is an effective growth (or decay) rate. We take γ to be independent of time, which essentially limits our analysis to times before saturation has been reached. We have $B_2(t+u) = B_2(u)exp(\gamma t)$, and

$$\overline{C}_{BB}(t) = \Big[\frac{C_{BB}(t)}{C_{BB}(0)}\Big] = exp(\gamma t) \tag{102}$$

The increase of the normalised correlation functions is then a measure of the effective growth rate.

4.6 Scaling of Laser-Produced Shock Waves to Cassiopeia A

Using hydrodynamic scaling relations [9][8], our experimental conditions at 0.3 μs after the laser illumination can be scaled to the supernova remnant Cassiopeia A with a probable age t_{SNR} of approximately 310 years, an expansion velocity v_{SNR} of about 4,700 km·s^{-1}

Table 1: Scaling between the laboratory and the SNR Cassiopeia A

Scaling parameters	**Definition**	**Laboratory**	**SNR Cas A**
Shock radius	L	1 cm	2.5 pc
Pressure	P	5×10^5 Pa	6.9×10^{-9} Pa
Particle density	n	10^{17} cm^{-3}	1 cm^{-3}
Electron temperature	T_e	2 eV	4.3 keV
Ion temperature	T_i	2 eV	43.3 keV
Time	t	0.3 μs	310 yrs
Velocity	v	2×10^6 cm/s	4,700 km/s
Deceleration parameter	vt/L	0.6	0.6
Peclet number	Pe	160	9.8×10^9
Reynolds number	Re	5.0×10^4	2.8×10^{24}
Radiation number	R_c	1,300	1.9×10^5
Magnetic field	B	5 G	100 μG
Plasma beta	β	5×10^6	170
Magnetic Reynolds number	Rm	5	3.6×10^{23}
Prandtl number	Pm = Rm/Re	1.0×10^{-4}	94

and a deceleration parameter $v_{SNR}t_{SNR}/R_{SNR}$ of about 0.6 [71], where R_{SNR} is the shock radius. The same scaling relations imply the wire thickness in the mesh corresponds to ~ 0.1 pc in the SNR. While Rm > 1 indicates magnetic field amplification can occur, Pm $\ll 1$ implies that frozen-in effects are not operative in this laboratory analogy. Furthermore, the discrepancy between Pm $\ll 1$ for the laboratory plasma and Pm $= 94$ for Cassiopeia A, indicates that this is not a perfect laboratory analogy. In fact there is strong diffusion in the laboratory analogy that can not be neglected. However, it is worth keeping in mind that the goal of the experiment is not to create an exact scaled model of Cassiopeia A. Instead we would like to study the phenomenon of magnetic field amplification as it (similarly) can occur in astrophysical objects such as Cassiopeia A. The scaling information in Table 1 indicates exactly how well the two plasmas compare.

From our scaling relations, the laboratory stretching rate calculated in Section 4.5 corresponds to a growth rate $\gamma_{SNR} \sim 0.4 \times 10^{-3}$ yr^{-1} on spatial scales ~ 1 pc in the SNR. At smaller scales in our experiment, where resistivity dominates, there are still sustained

magnetic fluctuations (Figure 33). The timescale for the resistive-chaotic-tangling balance to be established at those scales is η/l_e^2, where l_e is of order 1 mm (which is the induction coil size, and therefore the measurement resolution limit). The fact that the Golitsyn spectrum extends at least to these scales is an indirect confirmation that turbulence is established [11], with inertial-range motions tangling the magnetic field much faster than the motions at the energy-conserving scale (L_e). At scales of order l_e, the corresponding timescale is ≤ 50 ns in the laboratory, translating to ≤ 50 yr in the SNR over distances ~ 0.25 pc.

The observed variability of visible moving knots in the inner regions of the remnant is of the order of 10 yr [78]. The radio emission from Cassiopeia A can be characterised as a bright disordered ring of emission coincident with the cloud bank [78] surrounded by a polarised radio plateau of lower brightness with a predominantly radially stretched magnetic field extending to the outer shock seen in x-rays [76]. X-ray emission similarly consists of an inner ring of non-thermal emission broadly coincident with the cloud shell and an outer rim revealing the position of the outer shock [103]. The outer x-ray rim is thin because high-energy synchrotron-emitting electrons cool rapidly immediately downstream of the shock. The reverse shock, or shocks, may also accelerate the electrons needed for synchrotron emission at the inner ring.

Magnetic field amplification in Cassiopeia A can be thus understood as being partly due to amplification by cosmic rays at the shock and partly by the interaction, at a smaller radius, between ejecta and a clumpy medium. The latter process can be directly inferred from the experiment and its simulation. Our results are consistent with these observations, namely that a rotational flow, driven by a shock passing through a stationary density perturbation, is necessary to both amplify and sustain strong magnetic fields in an expanding magnetised plasma over distances corresponding to many times the scale of the initial density perturbation. Indeed, Figure 31 shows a disordered magnetic field, stretched from the grid position to the outer shock, matching the extent of the observed synchrotron emission.

On the other hand, as also indicated in Figure 31, in the absence of such perturbations (that is, without a grid), the magnetic field remains confined only to the outer rim. Our experimental work thus agrees with earlier numerical modelling of shock waves interacting with a clumpy medium [81][82][83], and it shows that magnetic fields can, on average, be amplified by the shock-induced rotational flow to values ~ 3 higher than expected from the jump conditions alone.

4.7 Reproducibility on Other Laser Facilities

Amplification of magnetic fields by turbulent processes was also measured using the Titan laser at the Lawrence Livermore National Laboratory. A 200 J green laser (527 nm) with a 5 ns pulse and 280 μm spot size, ablated a 500 μm diameter carbon rod (2.267 g·cm^{-3}) in an ambient 1.4 mbar Argon gas-filled chamber. To generate a turbulent flow, a plastic mesh grid with 1.1 mm holes and 400 μm wires was placed 1 cm from the target. To ensure the arrival of the shock at the grid was uniform across the shock front, the plastic mesh grid had a radius of curvature of 1 cm as seen in Figure 35. A 1 mm^3 Bdot probe located 4 cm from the target, characterised the shocked plasma.

Indeed magnetic field amplification was observed in the turbulent flow as seen in the Vulcan experiment. A moderate amplification of ~ 2 in the perpendicular components was observed for these similar conditions. This indicates that the mechanism of magnetic field amplification suggested by the Vulcan data is not an artefact of the experimental arrangements or facility. In fact, magnetic field amplification by turbulent motions is reproducible on other laser facilities. Further analysis of the magnetic field spectra and shot-to-shot variation analysis went beyond the time allocation of the author's graduate programme. She will continue this analysis in the coming year which requires a significant amount of additional work and error analysis.

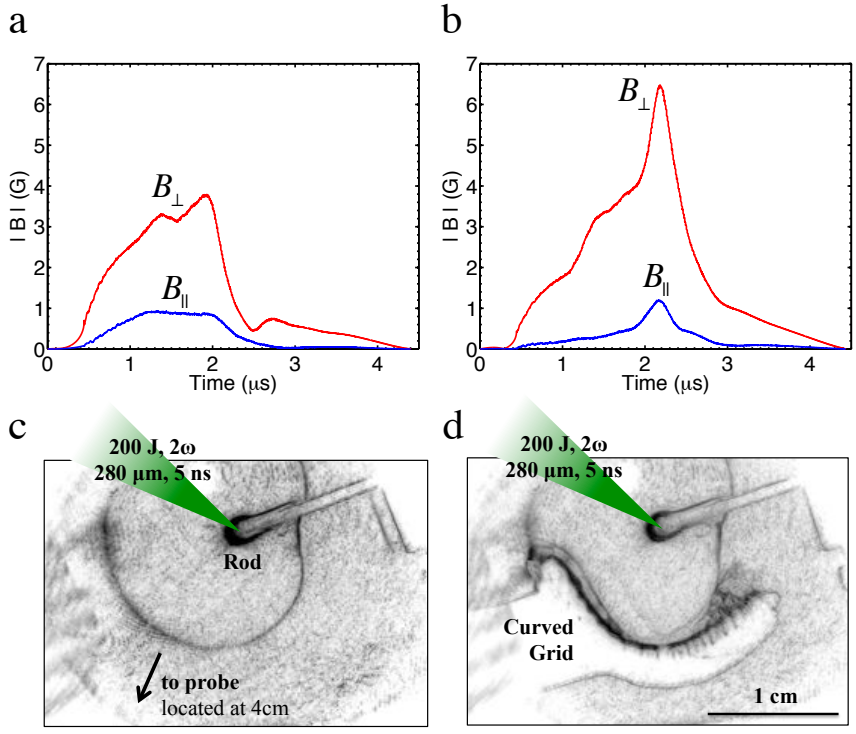

Figure 35: **Titan experimental setup to confirm magnetic field amplification results. a,** Bdot measurements of seed fields generated by the Biermann battery mechanism in a laser-produced shock wave. **b,** Magnetic field amplification of ~ 2 was observed in a turbulent flow generated by a non-conducting plastic grid. **c,** Schlieren images show a strong shock wave emanating from the carbon rod target in an ambient gas-filled chamber. **d,** A curved plastic grid induced a turbulent flow in the direction of the Bdot probes, located 4 cm from the target.

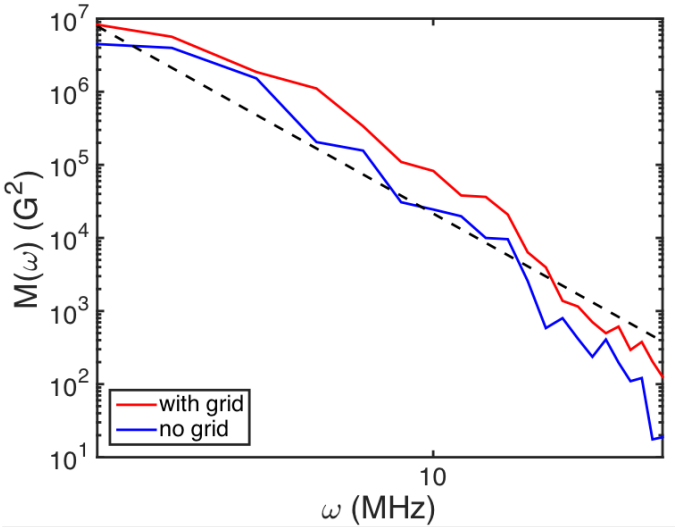

Figure 36: **Frequency spectrum of the magnetic field traces from Figure 35.** Plot of the measured magnetic energy spectrum $M(\omega) = |B(\omega)|^2$, where $B(\omega)$ is the fast Fourier transform of the total magnetic field for both the cases with (solid red line) and without a grid (solid blue line). The black dashed lines indicates the $\omega^{-11/3}$ Golitsyn spectrum. Due to limited shots on this experiment, shot-to-shot variation can not be reported.

Chapter 5

Nonlinear Amplification of Magnetic Fields in Laser-Produced Jets

The visible matter in the universe is turbulent and magnetised. Turbulence in galaxy clusters is produced by mergers and by jets of the central galaxies and believed responsible for the amplification of magnetic fields [104][15][105]. We report on experiments looking at the collision of two laser-produced plasma clouds, mimicking, in the laboratory, a cluster merger event. By measuring the spectrum of the density fluctuations, we infer developed, Kolmogorov-like turbulence [11]. From spectral line broadening, we estimate a level of turbulence consistent with turbulent heating balancing radiative cooling, as it likely does in galaxy clusters [106]. We show that the magnetic field is amplified by turbulent motions, reaching a nonlinear regime that is a precursor to turbulent dynamo [11]. Thus, our experiment provides a promising platform for understanding the structure of turbulence and the amplification of magnetic fields in the universe.

5.1 Astrophysical Motivation– Turbulence in Cluster Merger Events

The Coma Supercluster is comprised of over 1,000 identified galaxies that are gravitationally bound and emit strong x-rays due to temperatures of 10^7 K in the intracluster medium (ICM). The Coma cluster grew over time by accretion of matter and merger events. When clusters of similar mass collide, they produce turbulent motions which can contribute to

10% of the cluster's central energy density. The Coma Cluster has two central giant elliptical galaxies, NGC 4874 and NGC 4889, with a line-of-sight velocity difference of 700 km·s^{-1} [47]. X-ray observations indicate that a group of galaxies associated with NGC 4839 to the southwest is merging with the main cluster and resulting in the formation of high-surface-brightness 'arms' (labeled A1 thru A4) due to density fluctuations [47].

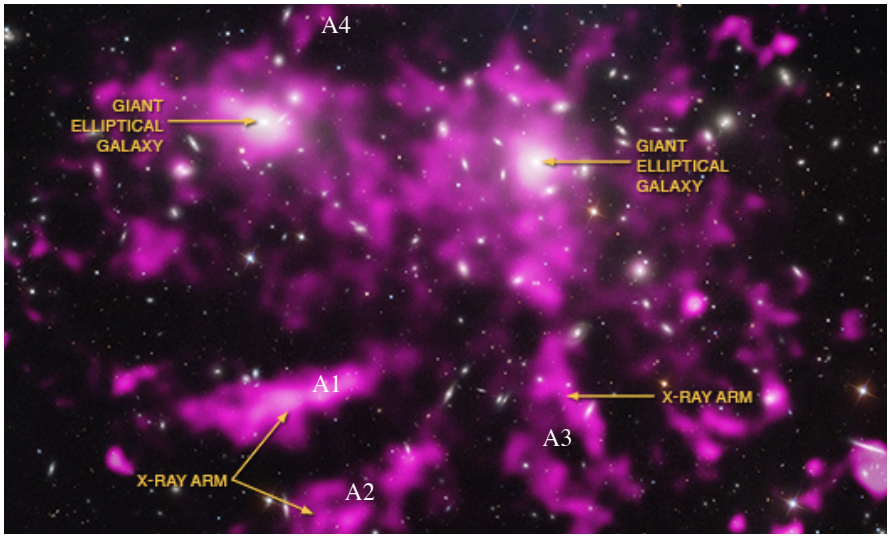

Figure 37: **Developed turbulence detected in the Coma cluster.** The optical data from the Sloan Digital Sky Survey, shows high-density arms (150 kPc) that resulted from a cluster merger event. X-ray observations from NASA's Chandra Observatory and ESA's XMM-Newton indicate that turbulent motions contribute to $\sim 10\%$ of the cluster's central energy density [47].

The arms in the core of the Coma cluster are likely the result of the gas stripped from subclusters merging within the cluster. This is supported by the fact that the entropy of the arms is lower than its surroundings which can give rise to density variations. In fact there is a tail of stripped material to the north of A1 behind GMP 2910. The stripping of gas is also seen in the Virgo Cluster, where subclusters of galaxies in M86 are merging with the main cluster. Using the Advanced Satellite for Cosmology and Astrophysics and the X-ray Multi-Mirror Mission (XMM-Newton), the arms are observed to be cooler than

their surroundings and the gaps between the arms [47]. Furthermore, they are in pressure equilibrium with their surroundings, and it has been estimated that A1, for instance, contains around 4×10^{10} solar masses of material. Assuming that A1 and A2 x-ray arms contain stripped material from a merger event involving the NGC 4911 subgroup, the material would remain coherent over several hundred kiloparsecs. Since the arms are massive and predicted to be 300 million years old, their motions do not instantaneously trace the ICM and do not indicate a laminar flow. Instead, turbulent flow is thought to operate in this region [47].

5.2 Experimental Arrangements

We have carried out experiments involving the collision of two plasma jets– reminiscent of cluster merger events– to produce a laboratory-scale replica of a turbulent intracluster plasma, although obviously our plasma is not confined in a dark matter potential well as it is in clusters. In the intracluster medium, large-scale turbulent motions are influenced by density stratification and gravity. However, at smaller spatial scales, the time periods for buoyancy-driven motions are much longer than those of the turbulent motions, so the fluctuations at these scales are universal, and thus similar to the turbulence we can create in our laboratory experiments. The scale invariance of hydrodynamic equations [14][9] implies that a distance of 1 cm in the laboratory corresponds to 100 kiloparsecs in the astrophysical case, 1 μs becomes 0.5 Gy, and a density of 4×10^{17} cm^{-3} is equivalent to 0.01 cm^{-3} in the galaxy cluster.

Our experiments were conducted using the Vulcan laser of the Central Laser Facility at the Rutherford Appleton Laboratory. We have focused multiple laser beams (with $\sim$ 240 J total energy and $\sim$ 1 ns pulse duration) onto a carbon foil to launch a plasma jet into an ambient, argon gas-filled chamber (at a pressure of 1 mbar). A full description of the experimental setup is given in Fig. 38. The laser configuration and details of the gas-

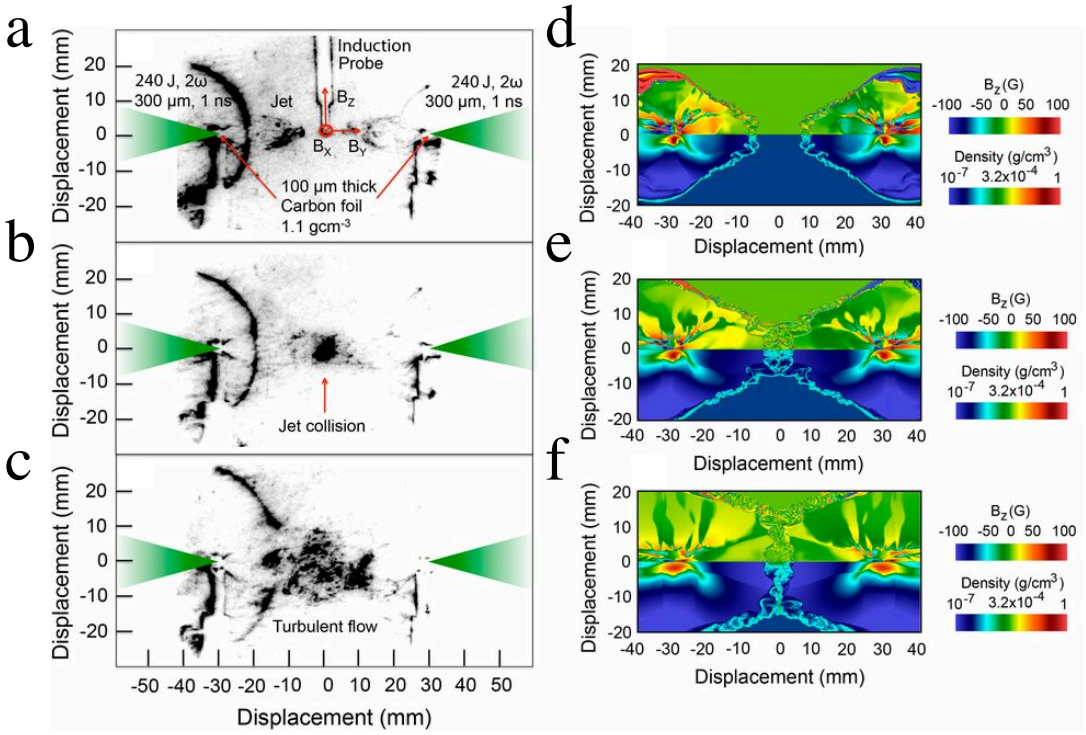

Figure 38: **Colliding jet configuration for the generation of turbulence.** Two carbon foils (100 μm thick, with density 1.13 g·cm^{-3}) are separated by 60 mm in a 1.0±0.2 mbar argon gas-filled chamber. Each target is ablated by three frequency-doubled (527 nm wavelength) laser beams with a laser spot diameter of 300 μm. The total laser illumination onto each foil is 240 ± 30 J in a 1 ns pulse length. An induction coil ($\geq$ 200 MHz bandwidth, with four twisted pair coils wound around the axis of a $\sim 1 \times 1$ mm^2 plastic core) is placed at equal distance between the foil targets. **a,** Schlieren image (using a 532 nm wavelength probe and 5 ns CCD gate width) of the jet formations at t = 500 ns after the laser shot. **b,** The jets collide at t = 800 ns, and **c,** turbulence develops by t = 1500 ns. **d,** Magnetic field (Top) and mass density (Bottom) from a FLASH simulation of the two jets at t = 500 ns. **e,** Same as **d** but at t = 800 ns. **f,** same as **d** but at t = 1500 ns.

filled chamber can be found in Section 4.3. Laser ablation of the carbon foil target drives a collimated jet from the back surface of the target (i.e., the side opposite to that illuminated by the laser). The target material ablated by the laser is slowed by the ambient medium, creating a wraparound shock, visible in Fig. 38. Optical and magnetic field diagnostics

(setup described in Section 4.3) were used to study the turbulent flows. Experiments were also performed using two sets of laser beams, each set illuminating a carbon foil, producing two jets that collide.

5.3 Plasma Characterisation of Laser-Produced Jets

Schileren measurements were taken to characterise the outflows at various times. The fastest moving material occurs on axis (see Figure 39) with $v_0 \approx 25$ km/s ($v_0/c_s \approx 4$, where c_s is the sound speed) at 3 cm from the target, while material on the edges of the jet moves more slowly as a result of Kelvin-Helmholtz shearing instabilities. In the case of interpenetrating jets, the collision drives strong turbulence in a region that grows from a size L $\sim$ 1 cm at $t = 0.8$ μs to $L \approx 2$ cm at $t > 1.5$ μs, at which time the turbulence reaches a more relaxed state. The error bars of each data point in Figure 39 were determined by shot-to-shot variations of identical experimental arrangements. All of the 2-5 repeats for each data point fall within the error bars shown.

5.3.1 Description and Implications of FLASH Simulations

We have performed 2D-cylindrical MHD simulations of the experiments using FLASH [91][92][93][94]. We initialise the simulations with two carbon foil targets having density 1.13 g/cm^3, radius 250 μm, and thickness 100 μm located at [0,0 cm] and [0,6 cm] (i.e., separated by 6 cm) in a [0, 2 cm] $\times$ [-1, 7 cm] cylindrical ($r - z$) computational domain, which is filled with argon gas at 1 mbar and at room temperature. Each target is illuminated by a laser whose energy is taken to be the measured value (i.e., 240 ± 30 J) for a duration of 1 ns, with a spot size of 300 μm. We used the measured shock position of the single jet at different times for a range of different laser energies to calibrate the fraction of the laser energy that is deposited in the target. We find that a fraction 57% is consistent with all of the measured shock positions within uncertainties, and we therefore use this fraction in

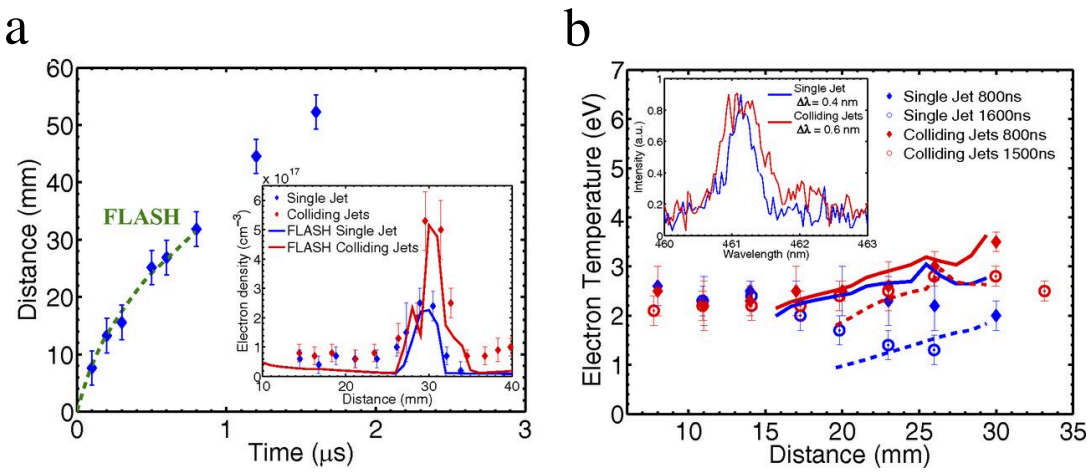

Figure 39: **Characterisation of jet propagation and collision. a,** Measurement of the jet leading edge vs. time from Schlieren data (blue symbols) and FLASH simulations (dashed green line). The FLASH simulation was calibrated to match the position of the leading edge of the jet at 800 ns for the measured value of the total laser energy for that data point. (Inset) The electron density profile obtained by interferometry at $t = 800$ ns compared with FLASH predictions. The density has been averaged over a volume of 5 mm radius from the axis connecting the two target foils. **b,** Spatially resolved electron temperature profile of a single jet (blue symbols) and colliding jets (red symbols) at $t = 800$ ns obtained from the measured argon spectral lines. Solid lines (blue, single jet; red, colliding jets) correspond to the predicted temperature values from FLASH simulations at $t = 800$ ns, averaged over the same volume as the electron density. Dashed lines are the results from the same FLASH simulations at $t = 1,500$ ns. (Inset) An example of the argon spectral line at $t = 800$ ns and 3 cm from the carbon foil target (averaged over 0.1 cm).

our simulations.

We use eight levels of refinement and blocks of 16×16 cells, obtaining an equivalent resolution of ~ 9.8 μm per cell (2048×8192 zones). The reconstruction is carried out with a piecewise linear method (PLM), using a minmod limiter; the Godunov fluxes are recovered with a Harten-Lax-van Leer Contact Riemann solver [97]. Outflow (zero gradient) boundary conditions are used except for the z-axis where axial symmetry is enforced. We

performed several simulations of the described setup for a single jet and for two colliding jets and followed their evolution for 2.5 μs. The FLASH MHD simulations and experimental results are consistent: The simulations quantitatively reproduce the flow characteristics, such as: the jet morphology, the position of the face of the jet with time, the electron number density and temperature in the interaction region, and the morphology and time behaviour of the magnetic field, including the time at which the field changes sign. The simulations underpredict the magnetic field strength since its turbulent amplification is not properly captured in a 2D geometry.

Two important characteristics of the experiments are the strength of the turbulent mixing produced by the collision of the jets and the persistence of the turbulent mixing. These characteristics are important for converting much of the kinetic energy of the jets into turbulence, which amplifies the seed magnetic fields. The FLASH simulations show that these characteristics result from the setup chosen for the experiment. Specifically, for the chosen setup, the carbon plasma produced by ablation of the target by the laser has just enough time to engulf the carbon foil target, wrap around it, and launch a shock in the argon gas before the jets are able to get ahead of it. As a result, the shock pinches the carbon jets. This pinching effect produces ripples in the faces of both jets that cause the fronts to become unstable (see Figure 40). It also causes the faces of both jets to have a shallow cup-like shape (so that, viewed in cross section, the faces of both jets have shallow, double-horned shapes).

When the two jets subsequently collide, the parts of the jet fronts that first do so are the rims of the shallow cup. (Viewed in cross section, it is the two shallow horns of each jet that meet first.) As a result, the argon gas between the faces of the two jets is trapped and mixes violently with the carbon in the jets (see Figure 41). As the two jets continue to collide, carbon in the rims of the jet faces flows outward, producing the expected disk-like flow, but at low velocity. The reason is that the remainder of the rims of the faces of both jets flows inward, further trapping the argon plasma. The resultant interaction region

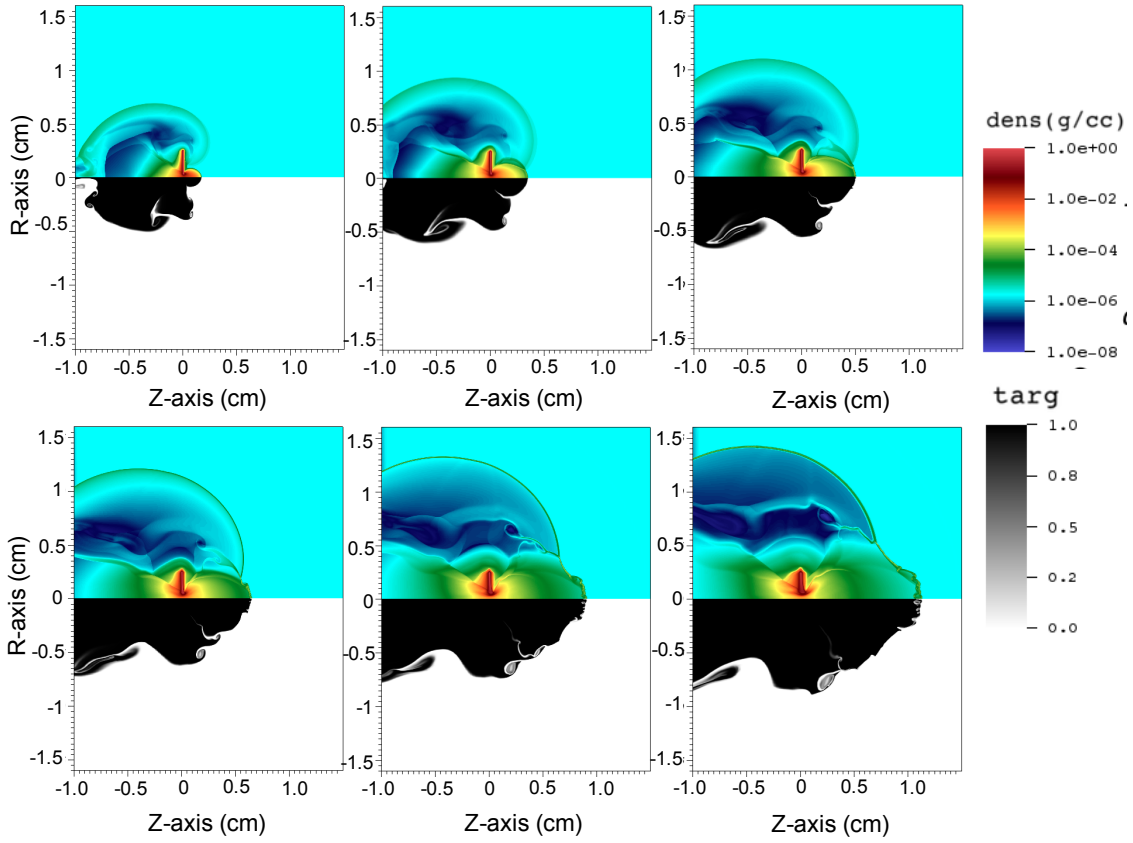

Figure 40: **Pinching of the jets by the wrap-around shock in the argon gas.** The six panels show close-up images of the shock produced by the carbon ablated by the laser, and the carbon jet at **(left to right, top to bottom)** 20 ns, 40 ns, 60 ns, 80 ns, 120 ns, and 160 ns showing the logarithm of the density (dens, top) and the target (targ) material fraction (bottom). The images show that the carbon plasma produced by laser ablation of the target has just enough time to engulf the carbon foil target, wrap around it, and launch a shock in the argon gas before the jets are able to get ahead of it. As a result, the shock pinches the carbon jets. This pinching effect produces ripples in the faces of both jets that cause the fronts to become unstable.

expands, to some extent, longitudinally (i.e., along the axes of the two jets) as the density of the plasma in the jets that arrives in the region decreases, but it cannot escape laterally (i.e., perpendicular to the axes of the two jets). The result is violent, turbulent mixing of

the argon gas and the carbon in the jets that persists for ~ 0.5 μs.

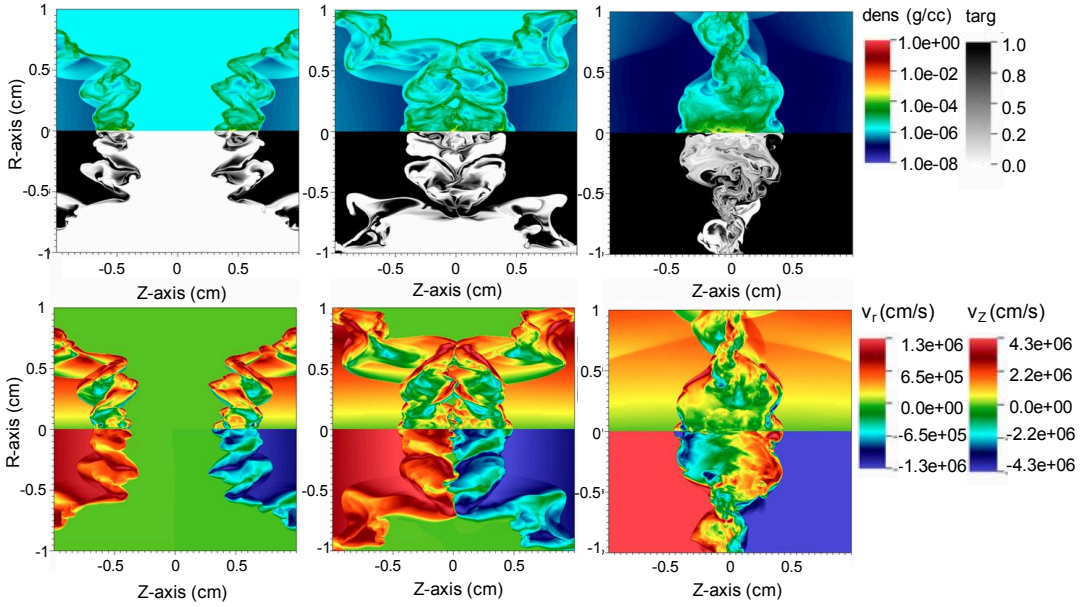

Figure 41: **Trapping and violent turbulent mixing of the argon gas and the carbon in the jets during collision. (Upper)** Close-up images of the interaction region at 600 ns, 800 ns, and 1,500 ns, showing the logarithm of the density (top) and the target material fraction (bottom). **(Lower)** Close-up images of the interaction region at the same three times, showing the radial velocity v_r perpendicular to the axes of the jets (top) and the velocity v_z parallel to the axes of the jets (bottom). The images show that the mixing between the argon gas and the jets is thorough and persists for ~ 0.5 μs

5.3.2 The MHD Approximation

By design, the plasma flows in the experiment are collisional, so that the interaction of the plasma jets produces strong turbulence. As we have shown, the ion-ion mean free path is $\lambda_{ii} \sim 0.005$ cm, which is much smaller than the characteristic size of the experiment. Such a small ion-ion mean free path ensures that kinetic processes are not important for the conditions of the experiment. Indeed, magnetic field generation by the Weibel instability is expected to become important when the ion skin depth is shorter than the mean free path.

The characteristic scale for the electromagnetic instability is [107][108] $l_{EM} \approx Kc/\omega_{pi}$, where ω_{pi} is the ion plasma frequency and $K \approx 100$ is a coefficient that indicates that the instability requires a certain number of ion skin depths to fully develop [109]. For our experimental conditions, we have $l_{EM} \approx 50$ cm, hence Weibel growth is strongly suppressed by collisions. The calculated Debye length is $\lambda_D \approx 2 \times 10^{-6}$ cm, and the inferred length scale for the development of electrostatic instabilities is $l_{ES} \approx 0.02$ cm, which is larger than the ion-ion mean free path, and thus electrostatic modes are suppressed by collisions.

The plasma coupling parameter is defined as [110]

$$\Gamma = \frac{Z^2 e^2}{4\pi\epsilon_0 a_i k_B T_i} \tag{103}$$

where Z is the ion charge, T_i is the ion temperature (assumed to be equal to the electron temperature), and $a_i = (3Z/4\pi n_e)^{1/3}$ is the mean ion separation. This represents the ratio of the average Coulomb energy per ion to the mean kinetic energy. Up to a numerical factor of the order of unity, $\Gamma \approx N_D^{-2/3}$, where N_D is the number of particles contained in the Debye sphere. An ideal (weakly coupled) plasma is a plasma for which Γ is small (or N_D is large). Since Γ acts as an expansion parameter in the thermodynamic equations, an ideal plasma exhibits statistical properties that are similar to those of an ideal gas [110].

With regards to the experiments and numerical simulations, the assumption of ideal plasma properties is implicitly adopted in the estimates of the dimensionless parameters (e.g., the Reynolds number) and collision frequencies, as well as thermal conductivities and opacities. It is thus important to verify such assumptions. Taking, at peak compression, $Z \approx 2.5$, $T_i \approx 3.5$ eV, and $n_e \approx 4 \times 10^{17}$ cm^{-3}, we get $\Gamma \approx 0.2$. For values $\Gamma \leq 1$, deviations from the ideal gas internal energy are of the order of $\sqrt{3}\Gamma^{3/2}/3 \approx 5\%$. Similar considerations hold for other thermodynamic and statistical properties [110]. These errors are smaller than those arising from measurement uncertainties and shot-to-shot variations. Moreover, in less dense plasma regions, we expect the coupling parameter to be even

smaller, and thus the ideal plasma approximation is well satisfied in our experiment.

5.4 Magnetic Field Characterisation of Jets

In our experiment, magnetic fields are generated, before the collision, via the Biermann battery mechanism, which is sustained by the shearing instability between the jet and the ambient medium. The Bdot probe was mounted onto a translation stage to allow for measurements along the forward path of the jet. By placing the probe tip at locations $2-6$ cm from the carbon foil target, the time history of the magnetic fields could be characterised as shown in Figure 42.

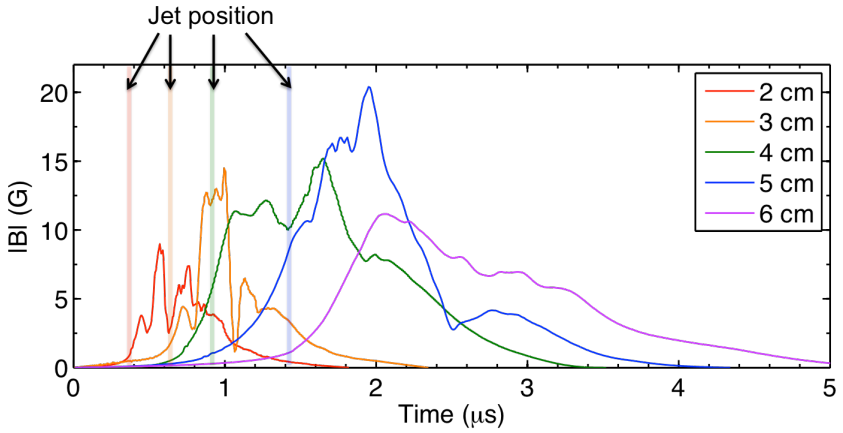

Figure 42: **Characterisation of magnetic fields from laser-produced jets.** The plots represent the total magnetic field detected by Bdot probes at locations $2-6$ cm from the target. Vertical lines indicate the arrival time of the jet front (from Schlieren measurements) at the Bdot probe locations. The peak magnetic field (~ 21 G) is detected 5 cm from TCC with a FWHM of ~ 1 μs. This plot also indicates the magnetic fields become longer-lived with distance and the peak magnetic field lags the plasma jet front.

The magnetic field produced by misaligned density and temperature gradients is not maximised close to the target, but instead, for this configuration, ~ 5 cm from the target. After 2 μs the Biermann battery fields have reached a maximum amplitude of 21 G with

a FWHM of ~ 1 μs. This plot indicates that the magnetic fields become longer-lived with a FWHM broadening from 0.6 μs to 1.6 μs over a distance of 4 cm. This implies that magnetic fields can become entangled in the turbulent flow caused by the pinching effect from the wrap-around shock. Magnetic diffusion prevents the fields from growing beyond 2 μs for this configuration. Furthermore, the peak of the magnetic field at each location ($2-6$ cm from the target) lags the jet front detected by Schlieren, indicating the fields are embedded in swept-up, turbulent material behind the jet tip. Due to time constraints on the laser facility, each shot in Figure 42 was taken 1-3 times to determine the shot-to-shot reproducibility and error bars. The peak magnetic field values were consistently within $\sim 10\%$ and demonstrated reproducible behaviour in terms of the FWHM which allows for trends in the magnetic field profiles to be inferred from Figure 42.

5.4.1 Effect of an Applied-Static Magnetic Field

Today's universe is ubiquitously magnetised. Therefore, it is of interest to study astrophysical objects in a pre-magnetised environment as they evolve in today's universe. Here we present observations of large-amplitude transient magnetic fields in a pre-magnetised ambient gas-filled chamber. Using the same setup as Section 5.2, a permanent magnet was placed 3 cm below the collision point of the jets to provide a vertical magnetic field along the z-axis as shown in Figure 43. The doughnut-shaped permanent magnet provided a 190 mT field at the collision point of the jets and 120 mT field 3 cm radially (in the $x-y$ plane of jet propagation) from the collision point (i.e., the location of the carbon foil targets). From Schlieren, we observe density gradients that indicate the jet flow is more confined in the presence of an applied magnetic field. The transient magnetic field of a single propagating jet at a location 3 cm from the carbon foil target has a total amplitude ~ 2 times larger than the field produced in a non-magnetised environment as shown in Figure 44. Static magnetic fields can become embedded in the turbulent flow of jet material, resulting in a larger observed field. Further analysis will be conducted into the nature of this

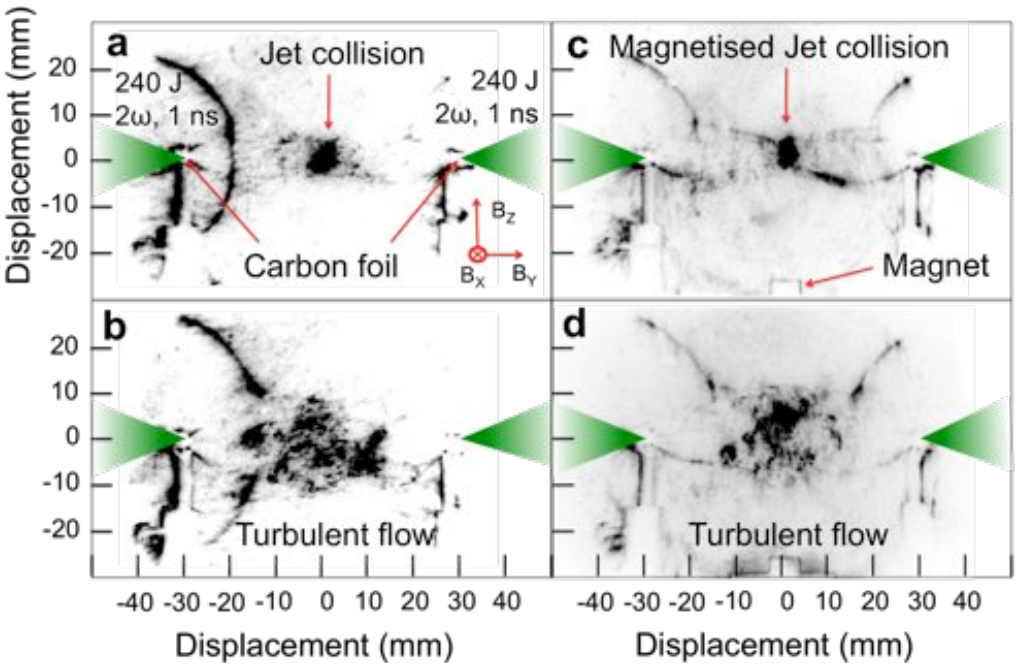

Figure 43: **Colliding jet configuration with an applied-static magnetic field.** The left images (**a** and **b**) show the configuration previously mentioned without an applied-static magnetic field at $t = 800$ ns and $t = 1,500$ ns respectively. The right images (**c** and **d**) are the same configuration with the additional permanent magnet placed 3 cm below the collision region. The static field is 0.19 T at the collision point and ~ 127 times stronger than the transient fields generated at that location without an applied field.

pre-magnetised plasma which went beyond the time-constraints of the author's graduate programme.

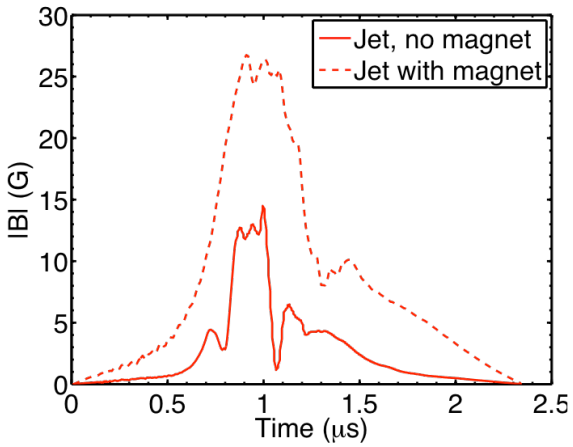

Figure 44: **Magnetic field generation and evolution in an applied-static magnetic field.** The solid red line shows the total magnetic field generated by the Biermann battery mechanism in the absence of an applied magnetic field. The dashed red line shows factor of ~ 2 enhancement of the generated magnetic field when traveling through a 0.3 T static field.

5.4.2 Magnetic Field Amplification in Colliding Jets

The Biermann battery fields generated by the laser-produced jets become tangled and amplified upon collision and development of turbulent motions. Figure 45 shows the magnetic field is larger by a factor of $\sim 2-3$ in the case of collision of the two jets compared with the unperturbed single jet. The FLASH simulation reproduces the morphology and time behaviour of the magnetic field, including the time at which the field changes sign. We expect the simulation to underpredict the peak magnetic field in the colliding jets case since turbulent amplification is not properly captured in 2D geometry.

Most importantly, the amplified magnetic field detected in the experiment is larger than the Biermann battery-produced field. This suggests that amplification has reached the nonlinear regime, with the amplified field roughly proportional to $\mathrm{Rm}^{1/2}$ [11]. In fact, after collision the Biermann battery mechanism has only a minor effect on the magnetic field in the interaction region of the colliding jets experiment. Figure 46 shows that by the

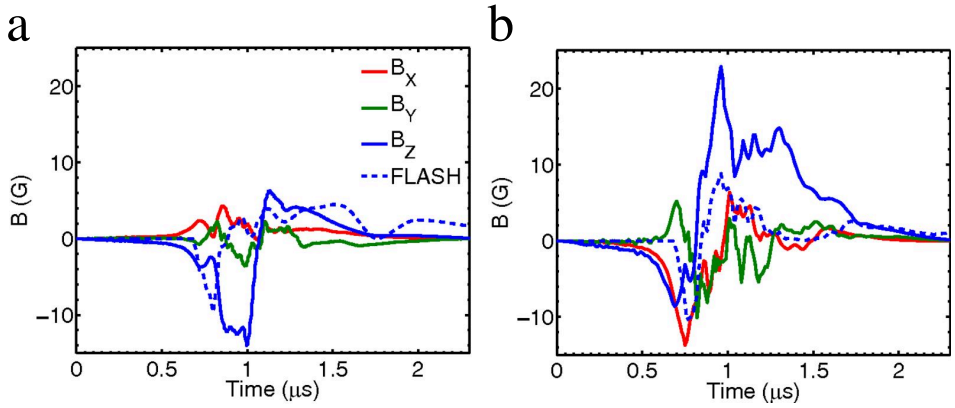

Figure 45: **Time evolution of the magnetic field. a,** The magnetic field components measured at 3 cm from the carbon foil in the case of a single jet. **b,** Magnetic field components measured in the case of jet collision. The time resolution of the magnetic field traces is 10 ns. These have been extracted from the recorded induction coil voltages. The dashed lines in both panels correspond to the average azimuthal magnetic field obtained from the FLASH simulations in a volume of radius 1 mm and length 3 mm centred at the midpoint between the two target foils. Due to cylindrical symmetry of the simulation domain, the measured component closest to the calculated one is B_z. We observe 2-4 times larger magnetic field contributions in the colliding jet configuration, implying magnetic field amplification due to turbulent motions. Furthermore, the x-axis and y-axis show amplifications up to 4 times larger in the colliding jet configuration which negates the explanation of a superposition of two magnetic fields– one from each jet– that could double the magnetic field at most.

time of collision, the magnetic fields are not dominated by the Biermann battery mechanism and are instead being stretched, twisted, and folded by the turbulent motions– a precursor to turbulent dynamo.

5.5 Development of Kolmogorov-like Turbulence

The turbulent velocity fluctuations on the system scale L can be estimated from Figure 39. At the collision point, the observed argon emission lines are broadened by ~ 0.2 nm.

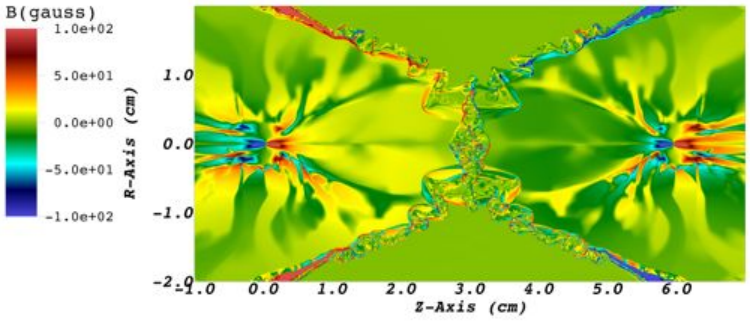

Figure 46: **Effect of the Biermann battery mechanism on the magnetic field in the interaction region of the colliding jets experiment.** The top half of the image shows the magnetic field strength at t = 1 μs in a FLASH simulation of the colliding jets experiment in which the Biermann effect was turned off at t = 716 ns (i.e., just before the two jets collide). The bottom half of the image shows the same, except the Biermann effect was on throughout the simulation. Comparison of the two images shows that the morphology and the overall value of the magnetic fields are similar in both cases, demonstrating that the Biermann battery mechanism has only a small effect on the magnetic field in the interaction region.

Half of this broadening is attributed to the increased density, and to a lesser extent to the higher temperatures (thermal broadening is small due to the large ion mass). The broadening due to turbulent motions is then $\sim$ 0.1 nm, corresponding to a turbulent velocity $v_{turb} \approx 27 \pm 5$ km/s. Thus, $V_{turb} \approx v_0$, suggesting that the collision effectively randomises the directed velocities of the two jets. Taking the measured values of jet velocity, density, and temperature in the collision region, and assuming an ionisation state $Z \approx 2.5$ for argon, we estimate the interjet electron-ion ($\lambda_{ei} \approx 0.04$ cm) and ion-ion ($\lambda_{ii} \approx 0.005$ cm) mean free paths to be significantly smaller than the size of the jets. This confirms that the two jets strongly interact via Coulomb collisions and the contact surface between the two jets becomes quickly unstable. The Reynolds number calculated with respect to the scale L is thus Re $= v_{turb}L/v \approx 1.0 \times 10^6$ ($v \approx 2.8$ cm^2/s is the kinematic viscosity of the plasma).

From the measurement of the magnetic energy spectrum $M(\omega)$, shown in Figure 47, it

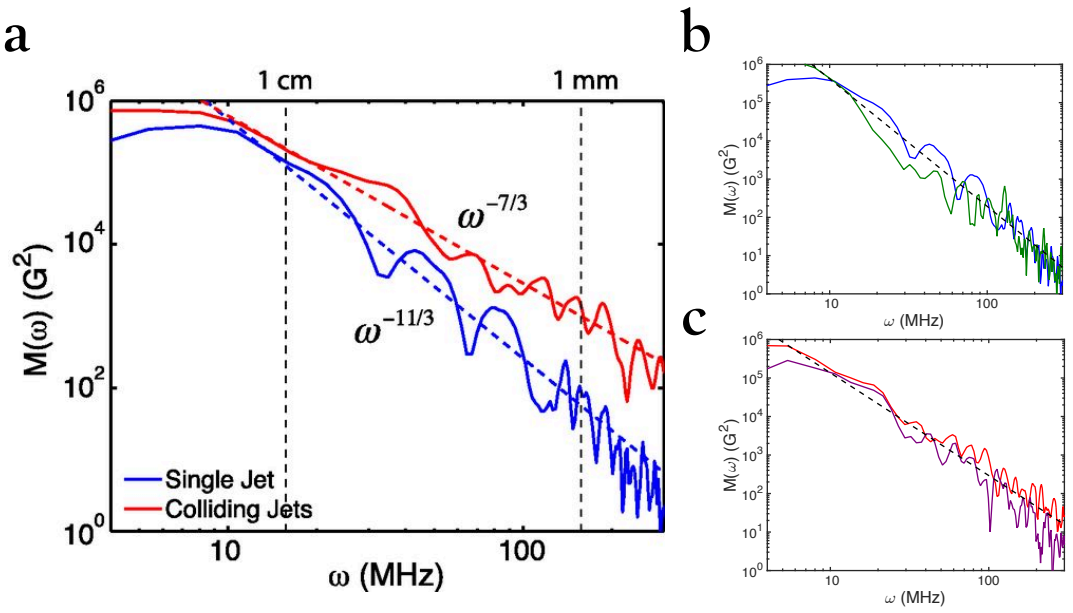

Figure 47: **Power spectra of the turbulence. a,** Plot of the magnetic energy spectrum $M(\omega) = |B(\omega)|^2$, where $B(\omega)$ is the discrete Fourier transform of the total magnetic field for the cases both with a single jet (blue solid line) and with colliding jets (red solid line) of the magnetic field traces in Figure 45. The slope of the spectrum in the case of colliding jets is shallower than in the case of a single jet (where it is consistent with the $k^{-11/3}$ Golitsyn spectrum, assuming conversion from frequencies to wavenumbers according to Taylor hypothesis, $\omega \approx v_0 k$). This gradual shallowing of the spectrum with increasing Rm is a signature of the dynamo precursor regime. The measured frequency spectrum, $\sim \omega^{-7/3}$, can be argued to correspond to wavenumber spectrum, $\sim k^{-1.9}$, in the case of colliding jets, where Taylor's hypothesis is inapplicable. **b,** Shot-to-shot comparison of two identical shots measuring the magnetic field from a single jet at 3 cm from TCC. Both power spectrums fit the $k^{-11/3}$ Golitsyn spectrum (dashed line) and provide insight into the error analysis and reproducibility of probe measurements. **c,** Same as **b** but for the colliding jet configuration. The dashed line corresponds to $\sim k^{-1.9}$.

appears the amplification has reached the nonlinear regime. Translated into wavenumber spectrum, this spectrum is $M(k) \approx k^{-17/9}$, substantially shallower than the low-Rm Golitsyn spectrum [49] $k^{-11/3}$, which we observe in the case of no jet collision. The emergence of progressively shallower magnetic spectra is a sign of nonlinear field amplification, which

is a precursor to turbulent dynamo [11].

If the turbulent velocity fluctuations are much smaller than the mean flow velocity, $v_{turb} \ll v_0$, then Taylor's hypothesis applies [111], and $\omega = v_0 k$. This relation, when applied to the single-jet experiment, where the flow moves at the speed of the jet, gives the $k^{-11/3}$ law for the magnetic field power spectrum. This hypothesis is clearly invalid for the case of the colliding jets. The induction probe sits at the collision centre where the mean flow is at rest, and turbulent velocity fluctuations are intense. Let's assume the magnetic field scales as $B_l \approx l^b$, where b is some real number. The magnetic field energy spectrum as a function of wavenumber is thus $M(k) \approx k^{-(2b+1)}$. Our experiment shows that in the colliding jets case, Kolmogorov-like turbulence is produced, as indicated later in Section 5.6. In Kolmogorov's theory of turbulence, the velocity at scale l is $v_l \approx l^{1/3}$, so $\omega \approx v_l/l \approx l^{-2/3}$. Now, suppose the magnetic field is passively advected by the flow (i.e., there is no back reaction of the field on the fluid). This is certainly the case in the experiment where the magnetic energy is a small fraction of the inferred kinetic energy density of the turbulent motions. This then implies that $l \approx \omega^{-3/2}$ and $M(\omega) \approx \omega^{-(3b+1)}$. We are measuring $M(\omega) \approx \omega^{-7/3}$; hence $b = 4/9$ and the power spectrum of the magnetic field is $k^{-17/9} \approx k^{-1.9}$, measurably shallower than the Golitsyn's $k^{-11/3}$, as expected in the dynamo precursor regime [11].

5.5.1 Thermal Broadening due to Turbulent Motions

The plasma temperature is inferred from the measurements of argon spectral lines. The spectroscopy diagnostic images a field of view that spans the horizontal midplane from the carbon foil position to the induction coil tip onto a 50 μm slit. The spectrometer is coupled to a CCD camera with 20 ns gate width. The ratio of different emission lines has been fitted using the collisional-radiative code PrismSPECT with nonlocal thermodynamic equilibrium transition rates. Line ratio of emission spectra is independent of the electron density

for optically thin plasmas when collisional deexcitation of atomic level dominates over spontaneous radiative decay. This occurs when the electron density $n_e \gg 1.7 \times 10^{14} T_e^{1/2} (\Delta E)^3$ cm^{-3}, where T_e is the electron temperature (in electron volts) and ΔE is the transition energy (in electron volts). For our plasma and optical transitions in argon, we get the condition $n_e \geq 9 \times 10^{15}$ cm^{-3}, which is well satisfied in the regime of the experiment.

A detail of the argon line at 461 nm at 3 cm from the target is shown in Figure 48. In the colliding jet case, the line is broadened by ~ 0.2 nm compared with the single-jet propagation. A fraction of the line broadening can be attributed to the increase in density and, to a minor extent, to the higher temperature. To assess this contribution, we calculated the expected line profile using PrismSPECT for a plasma with ion density of 1.6×10^{17} cm^{-3} (corresponding to the peak electron density for $Z = 2.5$) and an electron temperature of 3.5 eV. The result of this calculation is reported in Figure 48, and the predicted width of the argon line is ~ 0.5 nm. The further increase in line broadening observed in Figure 48 for the colliding jet case is thus ~ 0.1 nm, which must be attributed to turbulent motions in the collection volume. While the Mach number of the turbulence is large (~ 4) and the turbulence is damped, the creation of turbulence in the experiment is not impulsive, but is driven as the two plasma clouds (which are ~ 0.5 cm in extent) interact. This interaction of the two plasma clouds continuously drives the turbulence over a time period $t > 0.4$ μs, indicated by the fact that the Ar spectral line widths remain broad during this time period (Figure 49).

5.5.2 Balancing Turbulent Heating with Radiative Cooling

For our plasma conditions, the radiative cooling rate per ion is $Q_{cool} \approx m_{ion} \kappa_P \sigma_{SB} T^4 \approx 0.5$ eV/ns, where m_{ion} is the argon mass, $\kappa_P \sim 8 \times 10^4$ cm^2/g is the Planck opacity, and σ_{SB} is the Stefan-Boltzmann constant. This implies that during one jet crossing time, $\sim L/v_0 \approx 400$ ns, the plasma should have cooled to near 1 eV, as in the case of a single-jet

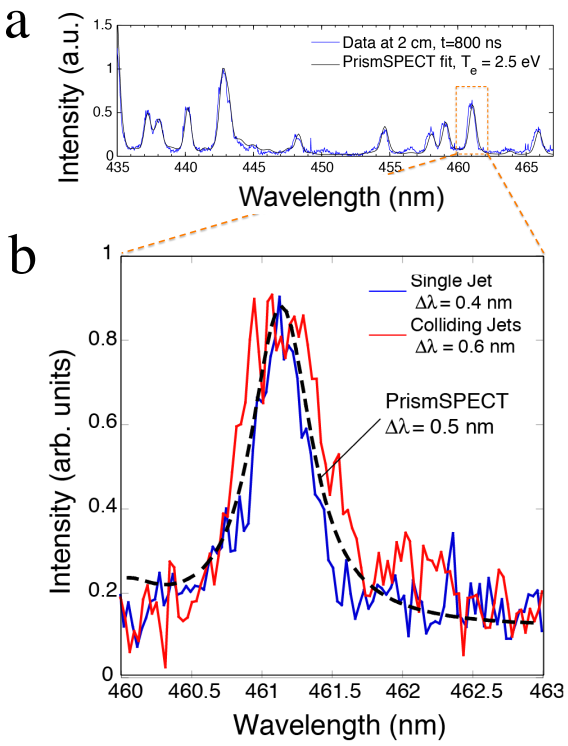

Figure 48: **Turbulent line broadening. a,** Measurement of spectral lines. Argon spectral lines at t = 800 ns for a single-jet experiment. Spectral fit performed with the code PrismSPECT is also shown. **b,** The measured argon spectral line at 461 nm at 3 cm from the carbon foil target for colliding jets (solid red line) and a single jet (solid blue line). A PrismSPECT calculation for an ion density of 1.6×10^{17} cm^{-3} and an electron temperature of 3.5 eV is also shown (dashed black line).

expansion. Figure 39 instead shows that in the collision region the temperature remains ≥ 2 eV over a few L/v_0, suggesting that much of the cooling must be offset by heating. Turbulent motions are eventually dissipated into heat. This heating rate per ion can be approximated as $Q_{turb} \approx m_{ion} v_{turb}^3 / L \approx 0.6$ eV/ns. Thus, $Q_{turb} \approx Q_{cool}$, consistent with turbulence playing an important role in achieving a stable temperature profile, with near balance between turbulent heating and radiative cooling.

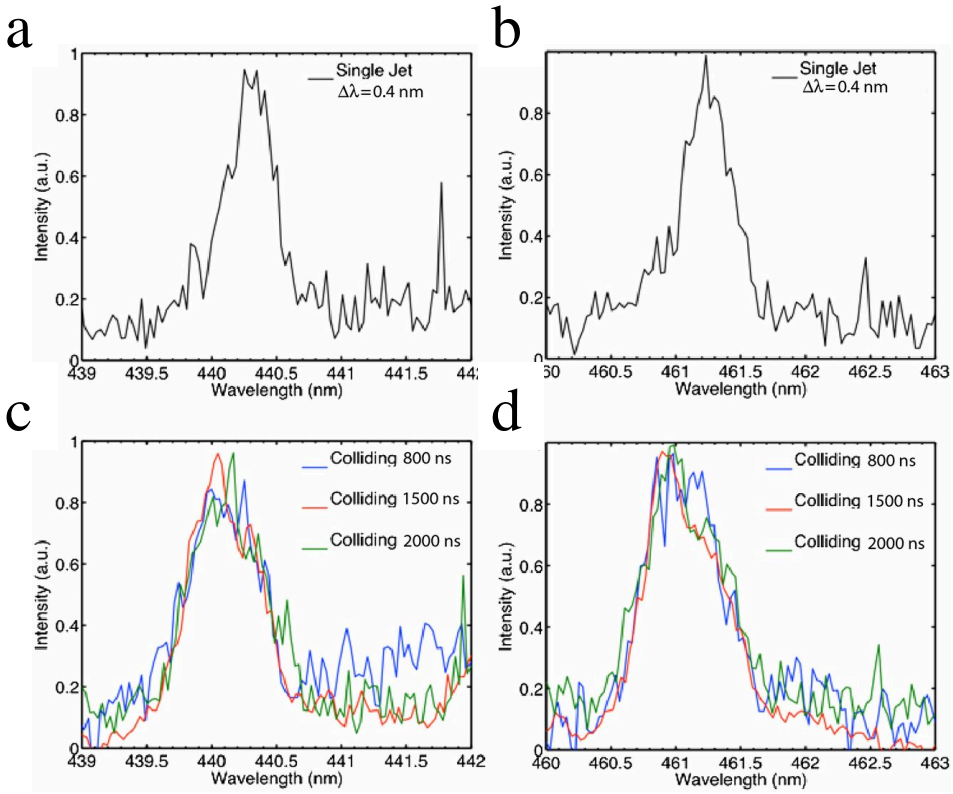

Figure 49: **Time evolution of spectral line widths. a,** The measured argon spectral line at 440 nm **b,** and 461 nm at 3 cm from the carbon foil target for a single jet (**a and b) and colliding jets at various times after the interaction (c and d).**

The calculation of the Planck mean opacity (κ_P) for argon was performed with the PROPACEOS (PRism OPACity and Equation Of State) code (www.prism-cs.com) [112]. This includes extensive collisional-radiative free-free, free-bound, and bound-bound transitions. PROPACEOS provides results that are very similar to the SESAME equation of state tables, and both models are based on the same theoretical assumptions. Typical values for κ_P are given in Figure 50. Since the cooling function depends nontrivially on both density and temperature [113], we have run a model calculation with the 1D radiation hydrodynamic code HELIOS [90] in radial geometry. The simulation was initialised with

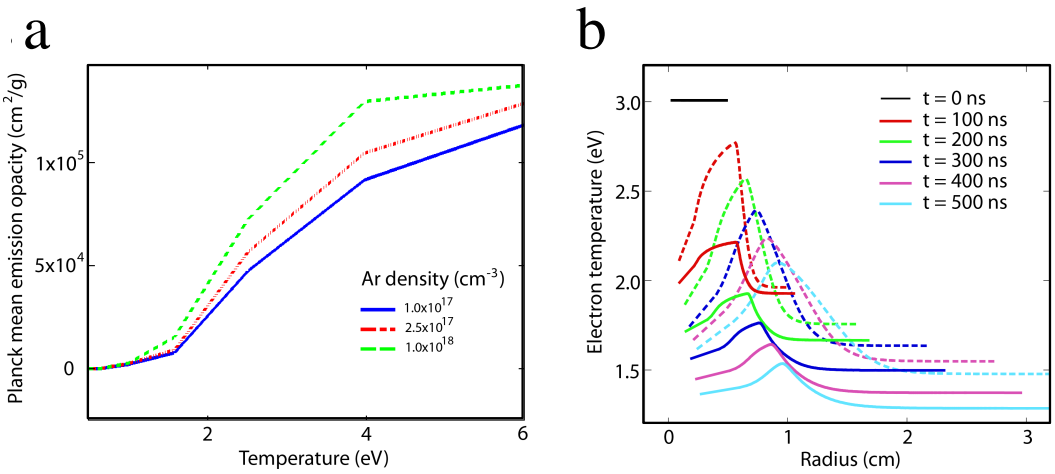

Figure 50: **Radiative cooling of the plasma.** **a,** Calculation of the Planck mean emission opacity (κ_P) for argon as a function of typical values of density and temperature expected in the experiment. **b,** 1D radiation hydrodynamic simulation with the code HELIOS showing the rapid cooling of an argon plasma sphere initialised with radius of 0.5 cm, $T_e = 3$ eV, mass density of 9×10^{-6} gcm^{-3}, and outward radial velocity of 14 km/s. Results from a calculation performed with multi-group radiation diffusion turned on are shown with solid lines. Results from a similar calculation but without radiation diffusion are shown with dashed lines.

argon contained in a sphere of 0.5 cm radius and 3 eV temperature and at a density of 9×10^{-6} g/cm^3. The plasma is assumed to expand outward with a radial velocity of 14 km/s. The results of the simulation, using the PROPACEOS equation of state table, are shown in Figure 50.

We see that the temperature quickly drops to below 1.5 eV, and, after a jet crossing time ($\sim$ 400 ns), it reaches values that are close to 1.2 eV. Figure 50 shows the same calculation but with the radiation package in HELIOS turned off, resulting in much higher temperature profiles. It is thus clear that radiation is a major contributor to the energy loss in this plasma. The same conclusion can also be drawn from a FLASH simulation of the colliding jets experiment in which multigroup radiation diffusion (and therefore radiative

cooling) was turned off at $t = 716$ ns (i.e., just before the two jets collide) and a simulation in which it was on throughout (Figure 51).

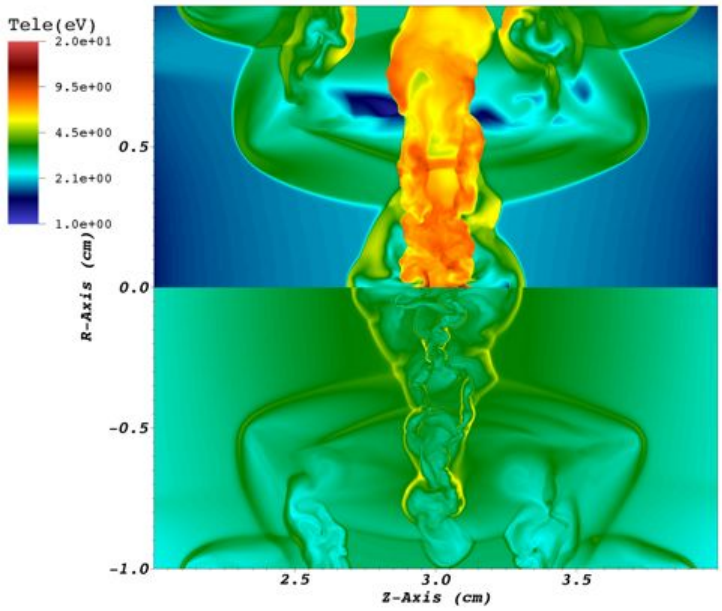

Figure 51: **Effect of radiative cooling in the interaction region of the colliding jets experiment.** The top half of the image shows T_e in the interaction region at $t = 1$ μs in a FLASH simulation of the colliding jets experiment in which multi-group radiation diffusion (and therefore radiative cooling) was turned off at t = 716 ns (i.e., just before the two jets collide). The bottom half of the image shows the same, except multi-group radiation diffusion was on throughout. Comparison of the two images shows T_e is a factor of ~ 3 larger in the first case, demonstrating that radiative cooling is very important in the interaction region.

5.6 Astrophysical Relevance to the Coma Cluster

In some respects, our experimental conditions are qualitatively similar to those found in galaxy clusters, where heating driven by turbulent motions in the intracluster plasma reduces radiative losses and decreases the net cooling rate [114]. On the other hand, while,

in the inertial range, energy is transferred from one scale to another at a rate given by Q_{turb}, which has the same form in both clusters and laboratory experiments, the actual mechanism for energy dissipation into heat can be different. This is dominated by collisional, isotropic viscosity in the laboratory, whereas in clusters, at a minimum, one must take into account that viscosity is anisotropic due to magnetic fields, and, furthermore, kinetic processes may play an important role [5]. Thus, the similarity between the laboratory 'replica' and the astrophysical reality can only hold at scales larger than the viscous one.

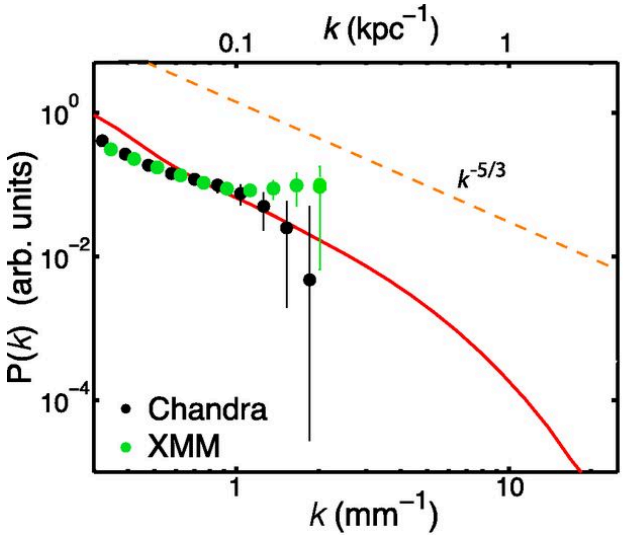

Figure 52: **Power spectra of turbulence. a,** Plot of the density fluctuation power spectrum $P(k) = |n_k/n_0|^2$, where N_k is the discrete Fourier transform of the space-dependent electron density and n_0 is its average value. In Schlieren imaging, the measured signal intensity is proportional to $\int(\partial n/\partial y + \partial n/\partial z)dx$, where n is the electron density, x, y are the image plane spatial coordinates, and z is the depth. Therefore, under the assumption that turbulence is statistically homogeneous across the jet interaction region, the discrete Fourier transform of the central region of the jet collision directly gives n_k. The power spectrum is arbitrarily normalised so that $P(k) \approx 1$ at the largest scale. The solid red curve corresponds to the experimental data, while the black and green symbols correspond to the inferred density spectrum in the Coma cluster obtained from CHANDRA and XMM satellite observations, respectively. Using a 500 μm Schlieren stop with a 7° collection angle over a distance of 1 m, results in the k-spectrum bounds of $0.06 < k < 12$ mm^{-1}. This follows from the discussion of Schlieren stop choices in Section 3.2.1.

During hierarchical structure formation, clusters form from accretion of filaments, galaxies, galaxy groups, and cluster mergers. In clusters of galaxies, turbulent velocities can be inferred from the density perturbations, which, in turn, are obtained using the measured x-ray radiation intensities [114][47][115]. The turbulence in clusters is mainly subsonic at small scales (and near sonic at large scales), so density fluctuations (injected at large scales) behave like a passive scalar. Therefore, the density and velocity spectra are expected to be the same [116]. The fact that turbulence is moderately supersonic in our experiment, while subsonic in clusters, is likely to lead to only a modest change in the power spectra (and at small enough scales, motions will, in any event, become subsonic). Indeed, spectroscopic observations of supersonic motions in molecular clouds [117] suggest a velocity power spectrum close to the classical Kolmogorov $k^{-5/3}$ law (where k is the wavenumber) that holds for incompressible fluids. Numerical simulations of supersonic turbulence show a spectrum somewhat steeper than Kolmogorov's, $k^{-1.9}$ to k^{-2}, depending on the details of the driving mechanism [118]. These differences are smaller than the uncertainties in our power spectrum measurements.

We have extracted the power spectrum of the electron density fluctuations from our data. The result is shown in Figure 52, using the wavelet method that was used for the analysis of x-ray maps of the Coma cluster [115]. The spectrum is consistent with a Kolmogorov-like power law, as expected from the theoretical work discussed in Section 2.5, suggesting that we do indeed see fully developed turbulence. A similar spectrum was obtained in galaxy clusters [115][47]. Despite important differences, the laboratory simulation of an intracluster plasma that we have created offers an important tool for modelling the amplification of magnetic fields by turbulent astrophysical plasmas.

5.7 Comparison with Laser-Produced Jets from Aluminium Foil Targets

Using the same setup described in Section 5.2, laser-produced jets were also formed from aluminium foil targets as shown in Figure 53. Flat foils (5×5 mm square), 10 μm thick of 2.7 g·cm^{-3} were ablated at the centre with a laser spot size of 300 μm of 240 J of green (527 nm) light in ~ 1 ns. The propagation of a single aluminium jet was characterised over several shots with optical diagnostics as seen in Figure 54. The fastest moving material along the axis of the jet was $v_0 \approx 50$ km/s ($v_0/c_s \approx 8$, where c_s is the sound speed) at 3 cm from the target. Interferometry indicates densities of 2.4×10^{17} cm^{-3} at 3 cm from the target for a single jet and $\sim 4.2 \times 10^{17}$ cm^{-3} in colliding jets. Though not plotted here, on some shots, it was observed that a larger square foil (i.e., 25×25 mm) was able to block the wrap-around shock and produce more collimated jets. In the case of interpenetrating jets, the collision drove strong turbulence in a region that grew from a size $L \sim 1$ cm at $t = 0.7$ μs to $L \sim 2cm$ at $t > 1$ μs when the turbulence reaches a more relaxed state.

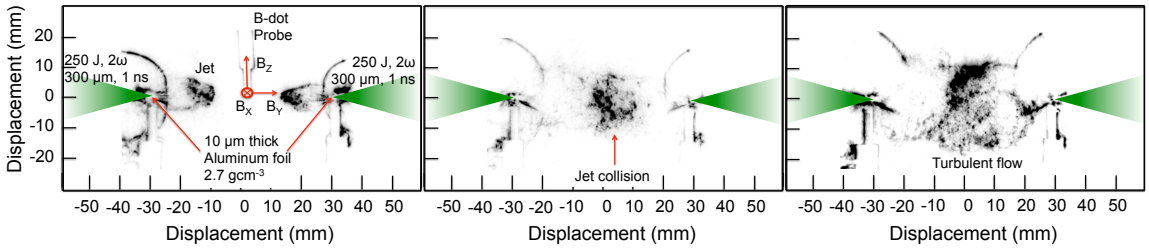

Figure 53: **Colliding jet configuration for aluminium foil targets.** As in the previous setup, two foil targets were separated by 60 mm in a 1.0±0.2 mbar argon gas-filled chamber. Each target was ablated by three frequency doubled (527 nm wavelength) laser beams with a laser spot diameter of 300 μm of 240 ± 30 J in a 1 ns pulse. However, this setup used 10 μm thick aluminium foil targets (2.7 g·cm^{-3}). **a,** Schlieren image of the jet formations at 200 ns after the laser shot. **b,** The jets collide at $t = 600$ ns, and **c,** turbulence develops by $t = 1,000$ ns.

5.7.1 Magnetic Field Characterisation and Development of Turbulence

As in the case of the carbon foils, the jets produced from the aluminium targets carry Biermann battery fields that become tangled and amplified by turbulent motions. Figure 55 shows that the magnetic field is larger by a factor of $\sim 2-7$ in the case of collision of the two jets compared with the unperturbed single jet. In particular, the B_z component was amplified by a factor of ~ 7 compared to the carbon jets which amplified fields by a factor of 3 (maximum). From the magnetic energy spectrum $M(\omega)$, shown in Figure 56, it appears the amplification for this target material has also reached the nonlinear regime where the stretching, twisting, and folding of magnetic fields due to turbulent motions is in operation. Further analysis and simulations are needed to complete this set of data that went beyond the time constraints of the author's graduate programme.

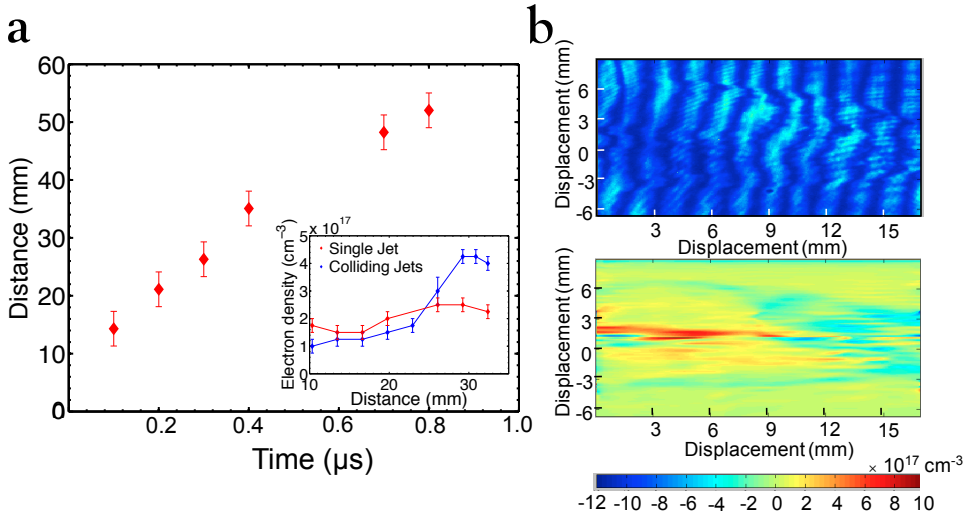

Figure 54: **Characterisation of aluminium jet propagation and collision. a,** Measurement of the jet leading edge versus time from Schlieren data (red symbols). (Inset) The electron density profile obtained by interferometry at $t = 600$ ns for a single jet (red symbols) and colliding jets (blue symbols). **b,** Interferogram (top) of a single laser-produced jet at 300 ns shows fringe shifts around the outer edges of the formation. Using the PAT software described in Section 3.2.2, a map of the density profile (bottom) can be constructed.

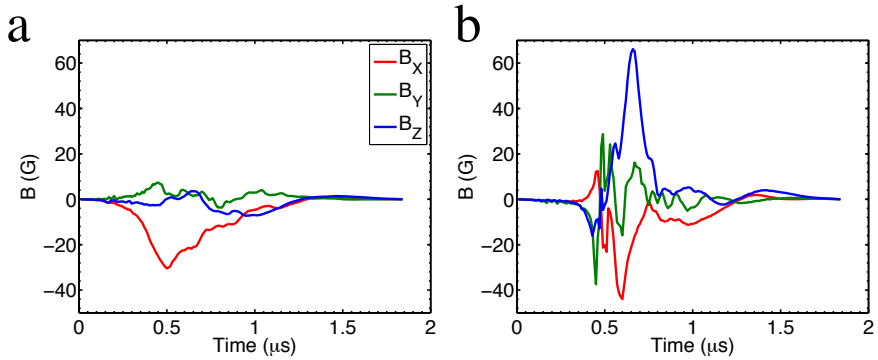

Figure 55: **Time evolution of the magnetic field using aluminium targets. a,** The magnetic field components measured at 3 cm from the aluminium foil surface in the case of a single jet. **b,** Magnetic field components measure in the case of jet collision show amplification of $\sim 2 - 7$.

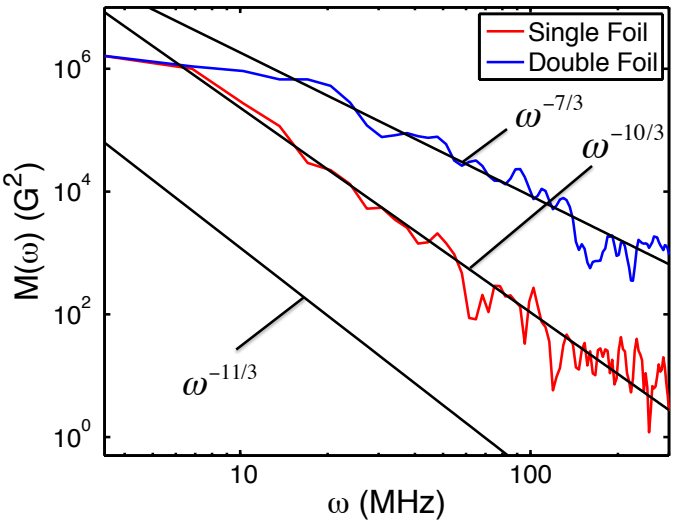

Figure 56: **Power spectra of the turbulence.** Plot of the magnetic energy spectrum $M(\omega) = |B(\omega)|^2$, where $B(\omega)$ is the discrete Fourier transform of the total magnetic field for the cases of both a single jet (blue solid line) and with colliding jets (red solid line). The slope of the spectrum in the case of the colliding jets is shallower than the $k^{-11/3}$ Golitsyn spectrum, demonstrating a nonlinear regime of developed turbulence.

Chapter 6

Future Work: Measurements of Turbulent Dynamo using the NIF

Experimental preparations are currently underway at the National Ignition Facility (NIF) to evince amplification of magnetic fields by the turbulent dynamo mechanism (for Pm = Rm/Re > 1)– the 'holy grail' of astrophysical plasma physics. As discussed, the standard model for the origin of galactic and intergalactic magnetic fields involves the amplification of seed fields by the turbulent dynamo process to a level consistent with current observations [4][5][6]. The results presented in Chapters 4 and 5 demonstrate that moderate amplification of magnetic fields can occur at low Pm due to the stochastic tangling of seed fields by turbulent motions, and the saturated level is set by balancing this process with Ohmic diffusion [11]. However, the NIF laser can provide ideal conditions to reach Rm > Re in laser-produced plasmas. It is the only facility in the world that is able to access the regime of high-temperature plasmas where resistivity can be neglected at all scales including the viscous dissipation scale. Such an experiment would establish, for the first time, the soundness of the theoretical expectation that tiny seed fields produced in the formation of protogalactic structures can be amplified to observed, dynamically significant values within cosmologically short times.

6.1 Experimental Arrangements

The simplest way to raise Rm in a laser-produced plasma experiment is to increase the laser-energy deposition to produce higher-velocity and higher-temperature plasmas. The highest

Table 2: **Summary of NIF Shot Day 1 scheduled February 18, 2016**

Day #1	**Configuration**	**Primary Diagnostics**	**Goal**
Shot 1	Double CH foils + Grid + D^3He capsule 133 kJ/ foil = 266 kJ total drive	GXD x-ray imaging, FABS polarimetry, PRAD proton radiography	Look for magnetic field amplification using PRAD and self-emission x-ray modulation
Shot 2	Double CD foils + Grid 133 kJ/ foil = 266 kJ total drive	GXD x-ray imaging, FABS polarimetry, Proton self-emission using SSII (4× magnification) and CR39	Look for magnetic field amplification using PRAD and self-emission x-ray modulation
Shot 3	Double CD foils + Grid 200 kJ/ foil = 400 kJ total drive	GXD x-ray imaging, FABS polarimetry, Proton self-emission using SSII (4× magnification) and CR39	Increase velocity of plasma to drive stronger turbulence

energy laser in the world resides in Livermore, California, and we have been allocated three shots day on the NIF– the first of which will be February 18, 2016 and we expect three shots.

To generate high-velocity, collisional flows, 96 beams of frequency-tripled (350 nm) light in a 15 ns square pulse and 1.6 mm focal spot, will be used to ablate the surface of two CH foils as shown in Figure (57). We expect 2.77 kJ per beam for a total of 133 kJ (8.85 TW) onto each opposing foil surface. The lasers ablate the disk surface, launching a shock through the washer, which develops over 2 mm until passing through a non-conducting grid, generating turbulence, and then finally undergoes a head-on collision with the identical, opposing turbulent flow. Turbulent dynamo is generated at the point of collision, 4 mm from each opposing target surface, and is analysed by a number of diagnostics.

The target components, manufactured by General Atomics (GA) and built by LLNL, are a stacked assembly including (in order starting from the ablation surface): a doped CH/CD disk, CH washer, plastic cylindrical shield, and curved plastic grid mesh. The doped CH or CD foil is planar with an outer diameter of 4 mm and 100 μm thickness. A

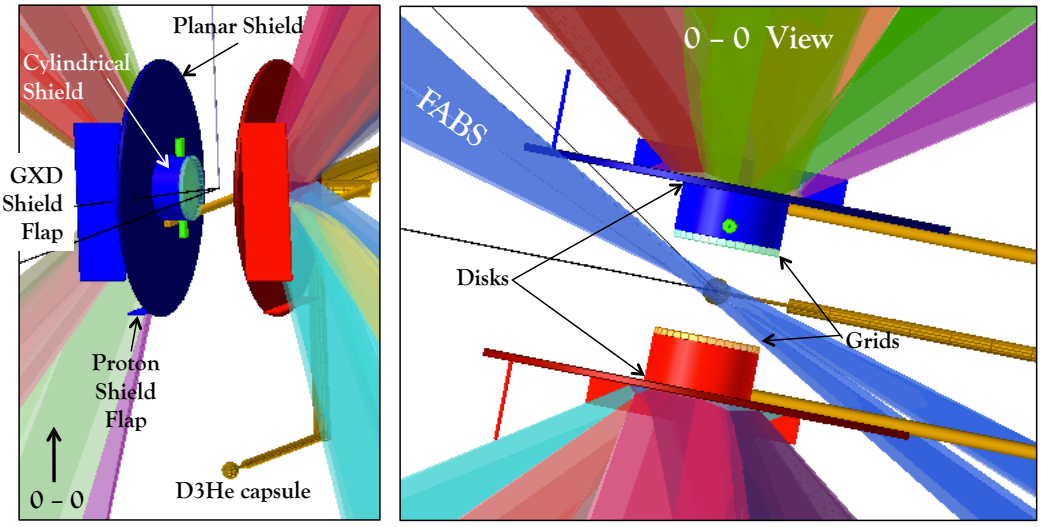

Figure 57: **Experimental arrangements of the NIF experiment to measure turbulent dynamo.** Two different views of the setup show 96 drive beams (133 kJ per target) onto 4 mm diameter doped CH/CD foils protected by $\sim$ 2 mm long cylindrical shields. Plastic non-conducting grids located 2 mm from each foil are used to generate a turbulent flow. The two flows collide at 4 mm from each target, developing turbulent dynamo for $\mathrm{Rm} > \mathrm{Re} \gg 1 \rightarrow \mathrm{Pm} > 1$.

dopant of 0.1% Mn and 0.1% Co is included to measure temperature with spectroscopy. For some shots, a CD foil is preferable to measure proton self-emission at the interaction region. A CH washer is placed on top of the disk to provide direction to the flow with a 1.2 mm inner diameter, 4 mm outer diameter, and 250 μm thickness. To avoid unconverted 1ω light from bouncing off the flat surface of the target and back into a beam port (potentially ruining the main amplifiers), the facility requires us to have cylindrical shields around the disk/grid assembly. The plastic cylindrical shields were 3-D printed by GA with 4 mm outer diameter, 3.8 mm inner diameter, and 1.475 mm height. The 4 mm diameter plastic grid was placed on top of the cylindrical shield with 300 μm apertures, 300 μm curved wires, and 270 μm thickness. On Shot 1, a D^3He capsule placed 18 mm from TCC (defined by the interaction region 4 mm from each target) was used to generate protons that can be detected on the $0-0$ DIM for proton radiography.

This is the main target assembly– however, additional components were added based on diagnostic and facility requirements. A large dimpled Al shield with CH coating was placed around the disk with 16.2 mm outer diameter and 4.1 mm inner diameter to protect the target from the drive laser light and unconverted 1ω. Shield flaps were placed on the outer edges of the large dimpled shield to protect the diagnostic cameras. A Cu shield with CH coating, 3 mm by 10 mm and $\sim$ 100 μm thick, was used to protect the $90-78$ DIM GXD camera from saturation of light from the laser spot interaction. A Cu shield with CH coating, 1 mm by 10 mm and $\sim$ 100 μm thick, was used to protect the D^3He capsule used on Shot 1 for proton radiography. Alignment fibres 1.25 mm long and 1 mm thick were placed on the cylindrical shields. The entire target assembly will be oriented along the equatorial plane (a plane that intersects the middle of both disk surfaces) in the chamber as shown in Figure (57).

To assess the magnetic fields present in our experiment, we employ proton radiography for Shot 1, proton self-emission from CD disk targets on Shots 2 and 3, time-resolved polarimetry on all shots using the FABS beams, nTOF to measure neutron yield, and pTOF or magpTOF to measure proton yield or proton energy distribution. For proton radiography (PRAD), a D^3He capsule with < 4 μm thick SiO_2 and 860 μm diameter is placed 18 mm from TCC (away from the polar $0-0$ DIM) and ablated by 15 quads (60 laser beams) of 350 nm light in a 900 ps pulse. Protons generated from the capsule explosion will stream through the interaction region, feel a deflection in the presence of magnetic fields, and be imaged onto 1.5 mm of CR39 with a 7 mm^2 field of view, 25 ns after the drive beams. Similar to results attained on the Omega laser in Rochester, New York, we hope to see caustics as a result of large magnetic fields generated by turbulent dynamo.

Since PRAD has not been proven successful on NIF experiments yet, Shot 2 and 3 will employ proton self-emission to assess the magnetic fields. Using a pinhole array with 1 mm, 2 mm, 3 mm, and 3.5 mm holes, a time-integrated signal will be detected on a image plate as shown in Figure (58). This will indicate the proton yield with 1-3.5 mm

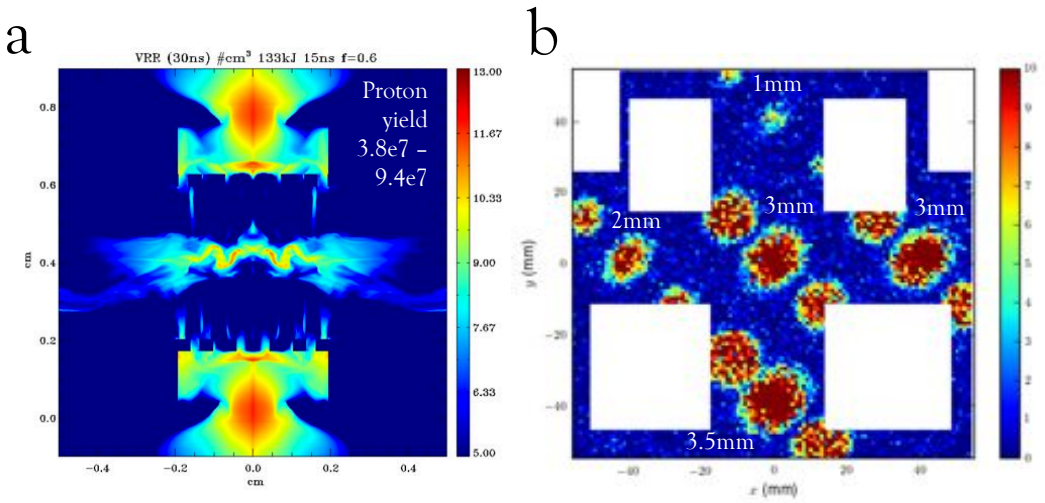

Figure 58: **Predicted proton self-emission measurements. a,** FLASH simulations indicate a proton yield of $3.8 \times 10^7 - 9.4 \times 10^7$ for a 133 kJ drive to each target. **b,** Predicted proton self-emission images onto the polar DIM image plate, courtesy of Alex Zylstra (LANL). Even for 3.5 mm pinholes, there is a distinction between protons emitted from the interaction region and ablated target surface. By measuring the proton yield, a lower bound on the ion temperature, and therefore Rm, can be determined.

spacial resolution, which can indicate a lower bound on the ion temperature. Assuming a turbulent driving scale of 300 μm, a lower bound on the Rm can be determined. On every shot, the four FABS beams will be used to measure polarimetry. Beam 316 is time-resolved and pointed at TCC, while the other three beams are time-integrated and pointed 500 μm off TCC with a 15 ns delay from the drive beams, 12.6 ns pulse, and best focus. For our conditions, we predict a polarisation rotation of $\sim$ 20 degrees/MG and $\sim$ 8 MG fields at TCC.

The gated x-ray camera (GXD) located at the $90 - 78$ DIM will be used to image the density turbulence as shown in Figure (59). The power spectrum of the turbulent motions can be inferred from density perturbations derived from x-ray maps. Shield flaps will protect the camera from saturation of the laser-target interaction region. The camera

features four strips that can be timed independently– we have chosen 15 ns, 23 ns, 27 ns, and 35 ns. A pinhole array located 267 mm from TCC and 633 mm from the detector will be used to image the region with a 2.4 magnification. In addition, two time-integrated cameras (SXI) will be located at $18 - 124$ and $161 - 326$.

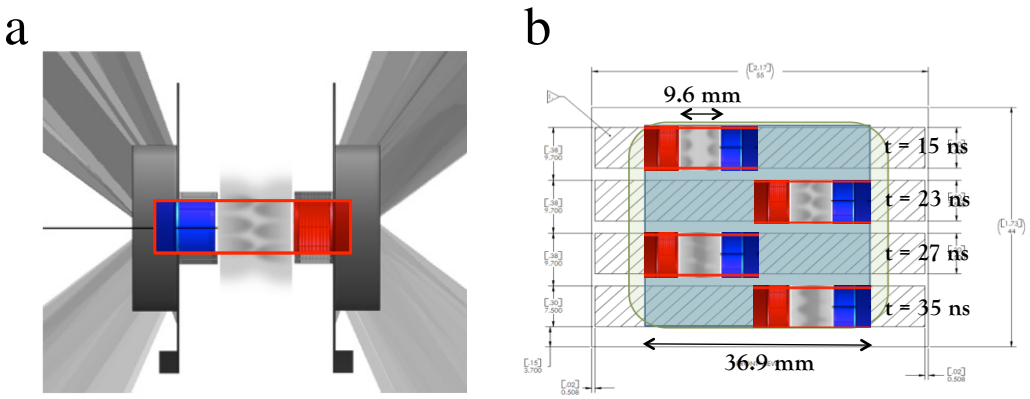

Figure 59: **Gated x-ray camera diagnostic to measure developed turbulence. a,** Graphic shows the coloured region that we are interested in imaging on the camera. A pinhole array with 25 μm diameter holes and 2.4× magnification are located between the interaction region and the $90 - 78$ DIM detector. **b,** Each of the four strips on the camera can be timed independently– we have chosen 15 ns, 23 ns, 27 ns, and 35 ns. Note the pinhole array has staggered holes, resulting in staggered images to avoid unwanted overlap between each image.

6.2 Predicted Results and Simulations

For the plasma flow to couple with the grid such that vorticity is injected at large scales, we need to ensure that the grid aperture remains much larger than the mean free path, $\lambda_{ii} \sim 4\times 10^{-4}$ cm. Therefore we employ a 300 μm aperture non-conducting grid located 2 mm away from the disk surface to allow formation of the laser-produced jet before interaction with the obstacle. To sustain turbulence and achieve a large Rm, we have employed tactics from both Chapters 4 and 5: a non-conducting grid obstacle and a colliding-flow arrangement to

develop turbulence. FLASH simulations indicate $v \sim 5\times10^7$ cm/s, $n_e \sim 2\times10^{20}$ cm^{-3}, and $T_e \sim 700$ eV. With a $l = 300$ μm spatial scale, Re $\sim 3,100$ and Rm $\sim 9,200$ which means the experiment should reach Pm $= 3$. Assuming turbulent dynamo is active, the magnetic fields will grow exponentially from the value of the initial seed field to equipartition, with a viscous-scale motion turnover rate of $v\mathrm{Re}^{1/2}/l \sim 90\mathrm{ns}^{-1}$. The will be a large number of eddy-turnovers while turbulence persists in the collision region, allowing for turbulent dynamo to fully develop.

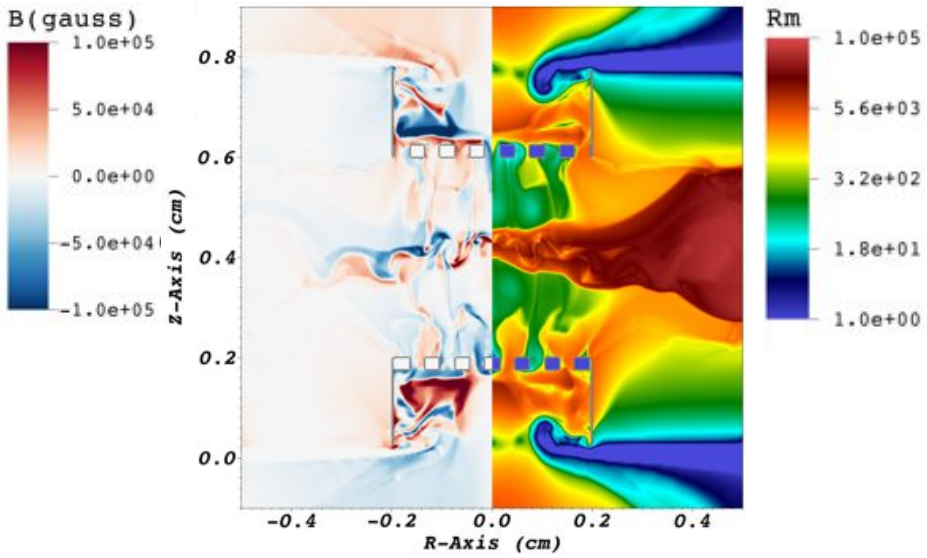

Figure 60: **FLASH simulations of the magnetic field and Rm**. Courtesy of Petros Tzeferacos, large fields ~ 8 MG and Rm $\gg 1$ can be achieved on the NIF. This is a 2-D simulation at 18 ns and 3-D simulations are currently underway.

Conclusions

Cosmic observations indicate the universe is ubiquitously magnetised [6]. Faraday rotation and Radio-Synchrotron emission measurements have revealed that clusters, filaments, and voids are magnetised from a few nG to tens of μG [2][3]. The origin and distribution of magnetic fields is unknown. The standard model for the origin of galactic and intergalactic magnetic fields involves three steps: First, generate small seed fields by some mechanism (e.g. Biermann battery) [4][5][6]. Second, amplify 'frozen-in' seed fields via stochastic tangling in a turbulent flow. Third, saturate the magnetic field amplification by the turbulent dynamo process, which occurs when the magnetic field strength reaches equipartition with the turbulent energy [11]. In 2012, G. Gregori measured the generation of seed fields (Step 1) in laser-produced shock waves scaled to the intergalactic medium [86].

In the fulfilment of a DPhil, the author presents the first measurements of magnetic field amplification and developed Kolmorgorov-like turbulence (Step 2) in laser-produced plasmas relevant to astrophysical events. Using the Vulcan laser, a non-conducting grid barrier was placed along the flow of a shock wave to generate vorticity. Within the turbulent features, a magnetic field amplification of $2-3$ was measured along with a $k^{-11/3}$ power spectrum characteristic of Kolmogorov turbulence. These results were scaled to the supernova remnant Cassiopeia A to explain the large magnetic fields observed in the turbulent interior of the remnant [7]. Using a similar setup, interpenetrating jets were generated in the laboratory to better understand merger events in the Coma cluster. Nonlinear magnetic field amplification of $2-3$ and a $k^{-7/3}$ power spectrum were observed, indicating the phenomena is a precursor to turbulent dynamo [10]. Combining the two results, the author is currently leading experimental efforts at the NIF, generating interpenetrating, laser-produced jets, perturbed by a non-conducting grid barrier to measure the coveted turbulent dynamo effect (Step 3). This work done by the author in fulfilment of a DPhil has helped explain the magnetisation of luminous matter in the universe.

References

[1] F. Miniati, D. Ryu, H. Kang, T. Jones, R. Cen, and J. P. Ostriker, "Properties of cosmic shock waves in large-scale structure formation," *The Astrophysical Journal*, vol. 542, no. 2, p. 608, 2000.

[2] F. Govoni and L. Feretti, "Magnetic fields in clusters of galaxies," *International Journal of Modern Physics D*, vol. 13, no. 08, pp. 1549–1594, 2004.

[3] M. L. Bernet, F. Miniati, S. J. Lilly, P. P. Kronberg, and M. Dessauges-Zavadsky, "Strong magnetic fields in normal galaxies at high redshift," *Nature*, vol. 454, no. 7202, pp. 302–304, 2008.

[4] E. G. Zweibel and C. Heiles, "Magnetic fields in galaxies and beyond," *Nature*, vol. 385, no. 6612, pp. 131–136, 1997.

[5] A. Schekochihin and S. Cowley, "Turbulence, magnetic fields, and plasma physics in clusters of galaxiesa)," *Physics of Plasmas (1994-present)*, vol. 13, no. 5, p. 056501, 2006.

[6] D. Ryu, H. Kang, J. Cho, and S. Das, "Turbulence and magnetic fields in the large-scale structure of the universe," *Science*, vol. 320, no. 5878, pp. 909–912, 2008.

[7] J. Meinecke, H. Doyle, F. Miniati, A. Bell, R. Bingham, R. Crowston, R. Drake, M. Fatenejad, M. Koenig, Y. Kuramitsu, *et al.*, "Turbulent amplification of magnetic fields in laboratory laser-produced shock waves," *Nature Physics*, vol. 10, no. 7, pp. 520–524, 2014.

[8] B. A. Remington, D. Arnett, R. Paul, H. Takabe, *et al.*, "Modeling astrophysical phenomena in the laboratory with intense lasers," *Science*, vol. 284, no. 5419, pp. 1488–1493, 1999.

[9] D. Ryutov, R. Drake, J. Kane, E. Liang, B. Remington, and W. Wood-Vasey, "Similarity criteria for the laboratory simulation of supernova hydrodynamics," *The Astrophysical Journal*, vol. 518, no. 2, p. 821, 1999.

[10] J. Meinecke, P. Tzeferacos, A. Bell, R. Bingham, R. Clarke, E. Churazov, R. Crowston, H. Doyle, R. P. Drake, R. Heathcote, *et al.*, "Developed turbulence and nonlinear amplification of magnetic fields in laboratory and astrophysical plasmas," *Proceedings of the National Academy of Sciences*, vol. 112, no. 27, pp. 8211–8215, 2015.

[11] A. Schekochihin, A. Iskakov, S. Cowley, J. McWilliams, M. Proctor, and T. Yousef, "Fluctuation dynamo and turbulent induction at low magnetic prandtl numbers," *New Journal of Physics*, vol. 9, no. 8, p. 300, 2007.

[12] R. P. Drake, "High-energy-density physics," *Phys. Today*, vol. 63, pp. 28–33, 2010.

[13] P. S. Committee *et al.*, *Frontiers in High Energy Density Physics:: The X-Games of Contemporary Science*. National Academies Press, 2003.

[14] J. E. Cross, B. Reville, and G. Gregori, "Scaling of magneto-quantum-radiative hydrodynamic equations: From laser-produced plasmas to astrophysics," *The Astrophysical Journal*, vol. 795, no. 1, p. 59, 2014.

[15] G. Giovannini, A. Bonafede, L. Feretti, F. Govoni, M. Murgia, F. Ferrari, and G. Monti, "Radio halos in nearby (z <0.4) clusters of galaxies," *Astronomy & Astrophysics*, vol. 507, no. 3, pp. 1257–1270, 2009.

[16] A. Neronov and I. Vovk, "Evidence for strong extragalactic magnetic fields from fermi observations of tev blazars," *Science*, vol. 328, no. 5974, pp. 73–75, 2010.

[17] E. Orrú, M. Murgia, L. Feretti, F. Govoni, G. Brunetti, G. Giovannini, M. Girardi, and G. Setti, "Low-frequency study of two clusters of galaxies: A2744 and a2219," *Astronomy & Astrophysics*, vol. 467, no. 3, pp. 943–954, 2007.

[18] F. Govoni, M. Murgia, L. Feretti, G. Giovannini, K. Dolag, and G. Taylor, "The intracluster magnetic field power spectrum in abell 2255," *Astronomy & Astrophysics*, vol. 460, no. 2, pp. 425–438, 2006.

[19] S. Mancuso and S. R. Spangler, "Faraday rotation and models for the plasma structure of the solar corona," *The Astrophysical Journal*, vol. 539, no. 1, p. 480, 2000.

[20] F. F. Chen and A. Trivelpiece, "Introduction to plasma physics," *Physics Today*, vol. 29, p. 54, 1976.

[21] R. O. Dendy, *Plasma physics: an introductory course*. Cambridge University Press, 1995.

[22] J. P. Ostriker and C. F. McKee, "Astrophysical blastwaves," *Reviews of Modern Physics*, vol. 60, no. 1, p. 1, 1988.

[23] P. Hartigan, J. Raymond, and J. Meaburn, "Observations and shock models of the jet and herbig-haro objects hh 46/47," *The Astrophysical Journal*, vol. 362, pp. 624–633, 1990.

[24] R. Narayan and E. Quataert, "Black hole accretion," *Science*, vol. 307, no. 5706, pp. 77–80, 2005.

[25] R. Schlickeiser and P. K. Shukla, "Cosmological magnetic field generation by the weibel instability," *The Astrophysical Journal Letters*, vol. 599, no. 2, p. L57, 2003.

[26] C. Huntington, F. Fiuza, J. Ross, A. Zylstra, R. Drake, D. Froula, G. Gregori, N. Kugland, C. Kuranz, M. Levy, *et al.*, "Observation of magnetic field generation via the weibel instability in interpenetrating plasma flows," *Nature Physics*, 2015.

[27] M. V. Medvedev, "Weibel turbulence in laboratory experiments and grb/sn shocks," *Astrophysics and Space Science*, vol. 307, no. 1-3, pp. 245–250, 2007.

[28] A. Bell and R. Kingham, "Resistive collimation of electron beams in laser-produced plasmas," *Physical review letters*, vol. 91, no. 3, p. 035003, 2003.

[29] F. Miniati and A. Bell, "Resistive magnetic field generation at cosmic dawn," *The Astrophysical Journal*, vol. 729, no. 1, p. 73, 2011.

[30] L. Pitaevskii and E. Lifshitz, *Physical kinetics*, vol. 10. Butterworth-Heinemann, 2012.

[31] H. Xu, B. W. Ohea, D. C. Collins, M. L. Norman, H. Li, and S. Li, "The biermann battery in cosmological mhd simulations of population iii star formation," *The Astrophysical Journal Letters*, vol. 688, no. 2, p. L57, 2008.

[32] E. Harrison, "Generation of magnetic fields in the radiation era," *Monthly Notices of the Royal Astronomical Society*, vol. 147, no. 3, pp. 279–286, 1970.

[33] K. Subramanian, D. Narasimha, and S. Chitre, "Thermal generation of cosmological seed magnetic fields in ionization fronts," *Monthly Notices of the Royal Astronomical Society*, vol. 271, no. 1, pp. L15–L18, 1994.

[34] N. Y. Gnedin, A. Ferrara, and E. G. Zweibel, "Generation of the primordial magnetic fields during cosmological reionization," *The Astrophysical Journal*, vol. 539, no. 2, p. 505, 2000.

[35] V. Korobkin and R. Serov, "Investigation of the magnetic field of a spark produced by focusing laser radiation," *ZhETF Pisma Redaktsiiu*, vol. 4, p. 103, 1966.

[36] G. Askar'yan, M. Rabinovich, A. Smirnova, and V. Studenov, "Currents produced by light pressure when a laser beam acts on matter," *Soviet Journal of Experimental and Theoretical Physics Letters*, vol. 5, p. 93, 1967.

[37] J. Stamper, K. Papadopoulos, R. Sudan, S. Dean, E. McLean, and J. Dawson, "Spontaneous magnetic fields in laser-produced plasmas," *Physical Review Letters*, vol. 26, no. 17, p. 1012, 1971.

[38] J. Chase, J. LeBlanc, and J. Wilson, "Role of spontaneous magnetic fields in a laser-created deuterium plasma," *Physics of Fluids (1958-1988)*, vol. 16, no. 7, pp. 1142–1148, 1973.

[39] N. Winsor and D. Tidman, "Laser target model," *Physical Review Letters*, vol. 31, no. 17, p. 1044, 1973.

[40] J. A. Stamper and B. H. Ripin, "Faraday-rotation measurements of megagauss magnetic fields in laser-produced plasmas," *Phys. Rev. Lett.*, vol. 34, pp. 138–141, Jan 1975.

[41] M. Drouet and R. Bolton, "Distribution of self-generated current in laser-produced plasmas," *Physical Review Letters*, vol. 36, no. 11, p. 591, 1976.

[42] A. Raven, O. Willi, and P. T. Rumsby, "Megagauss magnetic field profiles in laser-produced plasmas," *Phys. Rev. Lett.*, vol. 41, pp. 554–557, Aug 1978.

[43] J. Stamper, "Review on spontaneous magnetic fields in laser-produced plasmas: Phenomena and measurements," *Laser and Particle Beams*, vol. 9, no. 04, pp. 841–862, 1991.

[44] F. Pegoraro, S. Bulanov, F. Califano, and M. Lontano, "Nonlinear development of the weibel instability and magnetic field generation in collisionless plasmas," *Physica Scripta*, vol. 1996, no. T63, p. 262, 1996.

[45] W. D. Hayes, "The vorticity jump across a gasdynamic discontinuity," *Journal of Fluid Mechanics*, vol. 2, no. 06, pp. 595–600, 1957.

[46] A. N. Kolmogorov, "The local structure of turbulence in incompressible viscous fluid for very large reynolds numbers," in *Dokl. Akad. Nauk SSSR*, vol. 30, pp. 299–303, 1941.

[47] P. Schuecker, A. Finoguenov, F. Miniati, H. Böhringer, and U. Briel, "Probing turbulence in the coma galaxy cluster," *Astronomy & Astrophysics*, vol. 426, no. 2, pp. 387–397, 2004.

[48] M. T. Landahl and E. Mollo-Christensen, *Turbulence and random processes in fluid mechanics*. Cambridge University Press, 1992.

[49] G. Golitsyn, "Fluctuations of the magnetic field and current density in a turbulent flow of a weakly conducting fluid," in *Soviet Physics Doklady*, vol. 5, p. 536, 1960.

[50] J. Huba and N. P. Formulary, "Beam physics branch," *Plasma Physics Devision, Naval Research Laboratory, Washington, DC*, vol. 20375, 2007.

[51] W. L. Kruer, "The physics of laser plasma interactions," 1988.

[52] P. Gibbon and E. Förster, "Short-pulse laser-plasma interactions," *Plasma physics and controlled fusion*, vol. 38, no. 6, p. 769, 1996.

[53] V. Ginzburg, "The propagation of electromagnetic waves in plasmas,"

[54] T. H. Maiman, "Stimulated optical radiation in ruby," 1960.

[55] W. Koechner and M. Bass, *Solid-State Lasers: A Graduate Text*. Springer Science & Business Media, 2003.

[56] F. McClung and R. Hellwarth, "Giant optical pulsations from ruby," *Journal of Applied Physics*, vol. 33, no. 3, pp. 828–829, 1962.

[57] A. Yariv, "Quantum electronics, 3rd," *Edn.(John WieLy & Sons, New York, 1988) p*, vol. 389, 1989.

[58] E. Hecht, "Optics, 4th," *International edition, Addison-Wesley, San Francisco*, pp. 467–473, 2002.

[59] G. S. Settles, *Schlieren and shadowgraph techniques: visualizing phenomena in transparent media*. Springer Science & Business Media, 2012.

[60] I. H. Hutchinson, *Principles of plasma diagnostics*. Cambridge university press, 2005.

[61] M. Takeda, H. Ina, and S. Kobayashi, "Fourier-transform method of fringe-pattern analysis for computer-based topography and interferometry," *JosA*, vol. 72, no. 1, pp. 156–160, 1982.

[62] C. A. Palmer, E. G. Loewen, and R. Thermo, *Diffraction grating handbook*. Newport Corporation Springfield, Ohio, USA, 2005.

[63] E. Everson, P. Pribyl, C. Constantin, A. Zylstra, D. Schaeffer, N. Kugland, and C. Niemann, "Design, construction, and calibration of a three-axis, high-frequency magnetic probe (b-dot probe) as a diagnostic for exploding plasmas," *Review of Scientific Instruments*, vol. 80, no. 11, p. 113505, 2009.

[64] R. Shaw, J. Booske, and M. McCarrick, "Broadband calibration for magnetic probes for use in the maryland spheromak," *Review of scientific instruments*, vol. 58, no. 7, pp. 1204–1210, 1987.

[65] A. Nawaz, M. Lau, G. Herdrich, and M. Auweter-Kurtz, "Investigation of the magnetic field in a pulsed plasma thruster," *AIAA journal*, vol. 46, no. 11, pp. 2881–2889, 2008.

[66] J. Spaleta, L. Zakharov, R. Kaita, R. Majeski, and T. Gray, "Magnetic probe response function calibrations for plasma equilibrium reconstructions of cdx-u," *Review of scientific instruments*, vol. 77, no. 10, p. 10E305, 2006.

[67] J. Yang, J. Choi, B. Kim, N. Yoon, and S. Hwang, "A calibration method of a radio frequency magnetic probe," *Review of scientific instruments*, vol. 70, no. 9, pp. 3774–3775, 1999.

[68] M. Frigo and S. G. Johnson, "Fftw: An adaptive software architecture for the fft," in *Acoustics, Speech and Signal Processing, 1998. Proceedings of the 1998 IEEE International Conference on*, vol. 3, pp. 1381–1384, IEEE, 1998.

[69] U. Hwang, S. S. Holt, and R. Petre, "Mapping the x-ray-emitting ejecta in cassiopeia a with chandra," *The Astrophysical Journal Letters*, vol. 537, no. 2, p. L119, 2000.

[70] M. D. Stage, G. E. Allen, J. C. Houck, and J. E. Davis, "Cosmic-ray diffusion near the bohm limit in the cassiopeia a supernova remnant," *Nature Physics*, vol. 2, no. 9, pp. 614–619, 2006.

[71] D. J. Patnaude and R. A. Fesen, "Proper motions and brightness variations of non-thermal x-ray filaments in the cassiopeia a supernova remnant," *The Astrophysical Journal*, vol. 697, no. 1, p. 535, 2009.

[72] M. Anderson, J. Keohane, and L. Rudnick, "The polarization and depolarization of radio emission from supernova remnant cassiopeia a," *The Astrophysical Journal*, vol. 441, pp. 300–306, 1995.

[73] M. Anderson and L. Rudnick, "The deceleration powering of synchrotron emission from ejecta components in supernova remnant cassiopeia a," *The Astrophysical Journal*, vol. 441, pp. 307–333, 1995.

[74] A. Bell, "Proper motions and temporal flux changes of compact features in cassiopeia a at 5 ghz.," *Monthly Notices of the Royal Astronomical Society*, vol. 179, p. 573, 1977.

[75] A. Bell, "Turbulent amplification of magnetic field and diffusive shock acceleration of cosmic rays," *Monthly Notices of the Royal Astronomical Society*, vol. 353, no. 2, pp. 550–558, 2004.

[76] J. Vink and J. M. Laming, "On the magnetic fields and particle acceleration in cassiopeia a," *The Astrophysical Journal*, vol. 584, no. 2, p. 758, 2003.

[77] S. Gull, "The x-ray, optical and radio properties of young supernova remnants," *Monthly Notices of the Royal Astronomical Society*, vol. 171, no. 2, pp. 263–278, 1975.

[78] S. van den Bergh and W. Dodd, "Optical studies of cassiopeia a. i. proper motions in the optical remnant," *The Astrophysical Journal*, vol. 162, p. 485, 1970.

[79] R. A. Chevalier and J. Oishi, "Cassiopeia a and its clumpy presupernova wind," *The Astrophysical Journal Letters*, vol. 593, no. 1, p. L23, 2003.

[80] K. Borkowski, A. E. Szymkowiak, J. M. Blondin, and C. L. Sarazin, "A circumstellar shell model for the cassiopeia a supernova remnant," *The Astrophysical Journal*, vol. 466, p. 866, 1996.

[81] G. Gregori, F. Miniati, D. Ryu, and T. Jones, "Enhanced cloud disruption by magnetic field interaction," *The Astrophysical Journal Letters*, vol. 527, no. 2, p. L113, 1999.

[82] J. Giacalone and J. Jokipii, "Magnetic field amplification by shocks in turbulent fluids," *The Astrophysical Journal Letters*, vol. 663, no. 1, p. L41, 2007.

[83] F. Guo, S. Li, H. Li, J. Giacalone, J. Jokipii, and D. Li, "On the amplification of magnetic field by a supernova blast shock wave in a turbulent medium," *The Astrophysical Journal*, vol. 747, no. 2, p. 98, 2012.

[84] D. Milisavljevic and R. A. Fesen, "A detailed kinematic map of cassiopeia a's optical main shell and outer high-velocity ejecta," *The Astrophysical Journal*, vol. 772, no. 2, p. 134, 2013.

[85] R. M. Kulsrud, R. Cen, J. P. Ostriker, and D. Ryu, "The protogalactic origin for cosmic magnetic fields," *The Astrophysical Journal*, vol. 480, no. 2, p. 481, 1997.

[86] G. Gregori, A. Ravasio, C. Murphy, K. Schaar, A. Baird, A. Bell, A. Benuzzi-Mounaix, R. Bingham, C. Constantin, R. Drake, *et al.*, "Generation of scaled protogalactic seed magnetic fields in laser-produced shock waves," *Nature*, vol. 481, no. 7382, pp. 480–483, 2012.

[87] J. Hansen, M. Edwards, D. Froula, G. Gregori, A. Edens, and T. Ditmire, "Laboratory observation of secondary shock formation ahead of a strongly radiative blast wave," *Physics of Plasmas (1994-present)*, vol. 13, no. 2, p. 022105, 2006.

[88] J. F. Hansen, M. J. Edwards, D. Froula, G. Gregori, A. Edens, and T. Ditmire, "Laboratory simulations of supernova shockwave propagation," in *High Energy Density Laboratory Astrophysics*, pp. 61–67, Springer, 2005.

[89] H. Naiman and D. D. Knight, "The effect of porosity on shock interaction with a rigid, porous barrier," *Shock Waves*, vol. 16, no. 4-5, pp. 321–337, 2007.

[90] J. MacFarlane, I. Golovkin, P. Wang, P. Woodruff, and N. Pereyra, "Spect3d–a multi-dimensional collisional-radiative code for generating diagnostic signatures based on hydrodynamics and pic simulation output," *High energy density physics*, vol. 3, no. 1, pp. 181–190, 2007.

[91] A. Dubey, K. Antypas, M. K. Ganapathy, L. B. Reid, K. Riley, D. Sheeler, A. Siegel, and K. Weide, "Extensible component-based architecture for flash, a massively parallel, multiphysics simulation code," *Parallel Computing*, vol. 35, no. 10, pp. 512–522, 2009.

[92] B. Fryxell, K. Olson, P. Ricker, F. Timmes, M. Zingale, D. Lamb, P. MacNeice, R. Rosner, J. Truran, and H. Tufo, "Flash: An adaptive mesh hydrodynamics code for modeling astrophysical thermonuclear flashes," *The Astrophysical Journal Supplement Series*, vol. 131, no. 1, p. 273, 2000.

[93] P. Tzeferacos, M. Fatenejad, N. Flocke, C. Graziani, G. Gregori, D. Lamb, D. Lee, J. Meinecke, A. Scopatz, and K. Weide, "Flash mhd simulations of experiments that study shock-generated magnetic fields," *High Energy Density Physics*, 2014.

[94] P. Tzeferacos, M. Fatenejad, N. Flocke, G. Gregori, D. Lamb, D. Lee, J. Meinecke, A. Scopatz, and K. Weide, "Flash magnetohydrodynamic simulations of shock-generated magnetic field experiments," *High Energy Density Physics*, vol. 8, no. 4, pp. 322–328, 2012.

[95] D. Lee, "A solution accurate, efficient and stable unsplit staggered mesh scheme for three dimensional magnetohydrodynamics," *Journal of Computational Physics*, vol. 243, pp. 269–292, 2013.

[96] M. Fatenejad, A. Bell, A. Benuzzi-Mounaix, R. Crowston, R. Drake, N. Flocke, G. Gregori, M. Koenig, C. Krauland, D. Lamb, *et al.*, "Modeling hedla magnetic field generation experiments on laser facilities," *High Energy Density Physics*, vol. 9, no. 1, pp. 172–177, 2013.

[97] S. Li, "An hllc riemann solver for magneto-hydrodynamics," *Journal of computational physics*, vol. 203, no. 1, pp. 344–357, 2005.

[98] G. Comte-Bellot and S. Corrsin, "The use of a contraction to improve the isotropy of grid-generated turbulence," *Journal of Fluid Mechanics*, vol. 25, no. 04, pp. 657–682, 1966.

[99] A. Schlüter, "Über den ursprung der magnetfelder auf sternen und im interstellaren raum," *Zeitschrift für Naturforschung A*, vol. 5, no. 2, pp. 65–71, 1950.

[100] K. Moffatt, "The amplification of a weak applied magnetic field by turbulence in fluids of moderate conductivity," *Journal of Fluid Mechanics*, vol. 11, no. 04, pp. 625–635, 1961.

[101] P. Odier, J.-F. Pinton, and S. Fauve, "Advection of a magnetic field by a turbulent swirling flow," *Physical review E*, vol. 58, no. 6, p. 7397, 1998.

[102] R. M. Kulsrud, *Plasma physics for astrophysics*, vol. 77. Princeton University Press Princeton, 2005.

[103] E. Helder and J. Vink, "Characterizing the nonthermal emission of cassiopeia a," *The Astrophysical Journal*, vol. 686, no. 2, p. 1094, 2008.

[104] C. Ferrari, F. Govoni, S. Schindler, A. Bykov, and Y. Rephaeli, "Observations of extended radio emission in clusters," in *Clusters of Galaxies*, pp. 93–118, Springer, 2008.

[105] G. Taylor, A. Fabian, and S. Allen, "Magnetic fields in the centaurus cluster," *Monthly Notices of the Royal Astronomical Society*, vol. 334, no. 4, pp. 769–776, 2002.

[106] A. Malagoli, R. Rosner, and G. Bodo, "On the thermal instability of galactic and cluster halos," *The Astrophysical Journal*, vol. 319, pp. 632–636, 1987.

[107] H.-S. Park, D. Ryutov, J. Ross, N. Kugland, S. Glenzer, C. Plechaty, S. Pollaine, B. Remington, A. Spitkovsky, L. Gargate, *et al.*, "Studying astrophysical collisionless shocks with counterstreaming plasmas from high power lasers," *High Energy Density Physics*, vol. 8, no. 1, pp. 38–45, 2012.

[108] R. Drake and G. Gregori, "Design considerations for unmagnetized collisionless-shock measurements in homologous flows," *The Astrophysical Journal*, vol. 749, no. 2, p. 171, 2012.

[109] T. N. Kato and H. Takabe, "Nonrelativistic collisionless shocks in unmagnetized electron-ion plasmas," *The Astrophysical Journal Letters*, vol. 681, no. 2, p. L93, 2008.

[110] S. Ichimaru, *Statistical plasma physics*. Westview, 2004.

[111] G. I. Taylor, "The spectrum of turbulence," in *Proceedings of the Royal Society of London A: Mathematical, Physical and Engineering Sciences*, vol. 164, pp. 476–490, The Royal Society, 1938.

[112] G. I. Kerley, "Equation of state and phase diagram of dense hydrogen," *Physics of the Earth and Planetary Interiors*, vol. 6, no. 1, pp. 78–82, 1972.

[113] Y. B. Zel'dovich, Y. P. Raizer, W. D. Hayes, R. F. Probstein, and R. Landshoff, "Physics of shock waves and high-temperature hydrodynamic phenomena, vol. 2," *Physics Today*, vol. 23, no. 2, pp. 74–74, 2008.

[114] I. Zhuravleva, E. Churazov, A. Schekochihin, S. Allen, P. Arévalo, A. Fabian, W. Forman, J. Sanders, A. Simionescu, R. Sunyaev, *et al.*, "Turbulent heating in galaxy clusters brightest in x-rays," *Nature*, 2014.

[115] E. Churazov, A. Vikhlinin, I. Zhuravleva, A. Schekochihin, I. Parrish, R. Sunyaev, W. Forman, H. Böhringer, and S. Randall, "X-ray surface brightness and gas density fluctuations in the coma cluster," *Monthly Notices of the Royal Astronomical Society*, vol. 421, no. 2, pp. 1123–1135, 2012.

[116] I. Zhuravleva, E. Churazov, A. Schekochihin, E. Lau, D. Nagai, M. Gaspari, S. Allen, K. Nelson, and I. Parrish, "The relation between gas density and velocity power spectra in galaxy clusters: qualitative treatment and cosmological simulations," *The Astrophysical Journal Letters*, vol. 788, no. 1, p. L13, 2014.

[117] R. B. Larson, "Turbulence and star formation in molecular clouds," *Monthly Notices of the Royal Astronomical Society*, vol. 194, no. 4, pp. 809–826, 1981.

[118] C. Federrath, "On the universality of supersonic turbulence," *Monthly Notices of the Royal Astronomical Society*, p. stt1644, 2013.